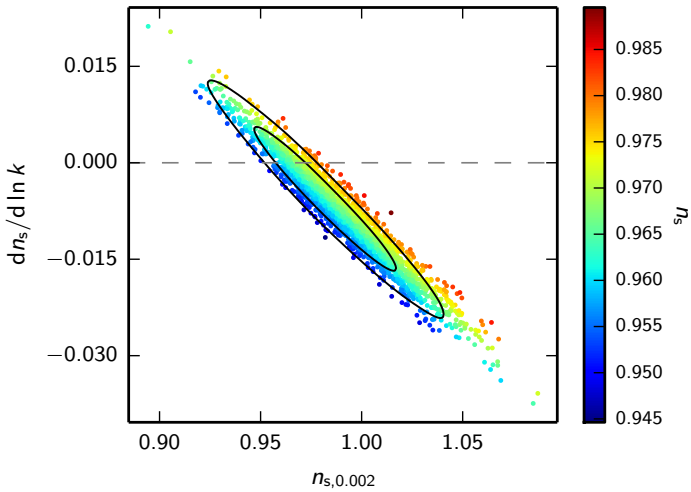

Fig. 23. Constraints on the running of the scalar spectral index in the ΛCDM model, using *Planck* TT+lowP (samples, coloured by the spectral index at $k = 0.05\,\mathrm{Mpc}^{-1}$), and *Planck* TT,TE,EE+lowP (black contours). The *Planck* data are consistent with zero running, but also allow for significant negative running, which gives a positive tilt on large scales and hence less power on large scales.

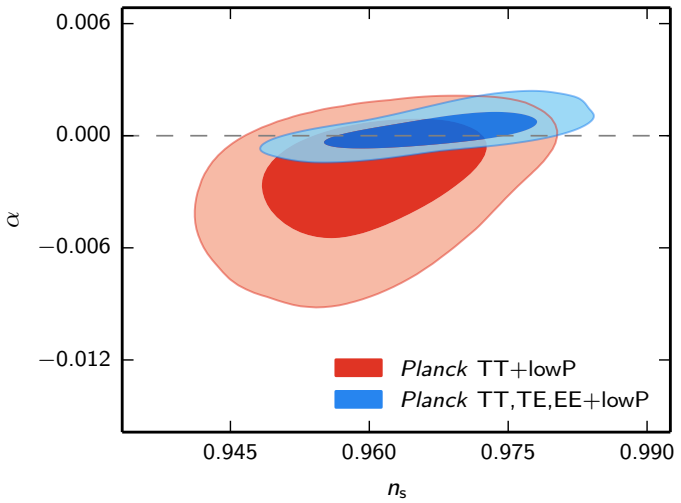

Fig. 24. Constraints on the correlated matter isocurvature mode amplitude parameter α, where $\alpha = 0$ corresponds to purely adiabatic perturbations. The *Planck* temperature data slightly favour negative values, since this lowers the large-scale anisotropies; however, the polarization signal from an isocurvature mode is distinctive and the *Planck* polarization data significantly shrink the allowed region around the value $\alpha = 0$ corresponding to adiabatic perturbations.

include tensor fluctuations in addition to running:

$$\frac{dn_s}{d\ln k} = -0.0126^{+0.0098}_{-0.0087}, \quad \textit{Planck}\ \text{TT+lowP}, \tag{42a}$$

$$\frac{dn_s}{d\ln k} = -0.0085 \pm 0.0076, \quad \textit{Planck}\ \text{TT, TE, EE+lowP}, \tag{42b}$$

$$\frac{dn_s}{d\ln k} = -0.0065 \pm 0.0076, \quad \textit{Planck}\ \text{TT+lowP+lensing +ext+BKP}. \tag{42c}$$

PCP13 found an approximately 2σ pull towards negative running for these models. This tension is reduced to about 1σ with the 2015 *Planck* data, and to lower values when we include the BKP likelihood, which reduces the range of allowed tensor amplitudes.

In summary, the *Planck* data are consistent with zero running of the scalar spectral index. However, as illustrated in Fig. 23, the *Planck* data still allow running at roughly the 10^{-2} level, i.e., an order of magnitude higher than expected in simple inflationary models. One way of potentially improving these constraints is to extend the wavenumber range from CMB scales to smaller scales using additional astrophysical data, for example by using measurements of the Lyα flux power spectrum of high-redshift quasars (as in the first year WMAP analysis, Spergel et al. 2003). Palanque-Delabrouille et al. (2015) have recently reported an analysis of a large sample of quasar spectra from the SDSSIII/BOSS survey. These authors find a low value of the scalar spectral index $n_s = 0.928 \pm 0.012$ (stat.) $\pm$ (0.02) (syst.) on scales of $k \approx 1\,\mathrm{Mpc}^{-1}$. To extract physical parameters, the Lyα power spectra need to be calibrated against numerical hydrodynamical simulations. The large systematic error in this spectral index determination is dominated by the fidelity of the hydrodynamic simulations and by the splicing used to achieve high resolution over large scales. These uncertainties need to be reduced before addressing the consistency of Lyα results with CMB measurements of the running of the spectral index.

6.2.3. Isocurvature perturbations

A key prediction of single-field inflation is that the primordial perturbations are adiabatic. More generally, the observed fluctuations will be adiabatic in any model in which the curvature perturbations were the only super-horizon perturbations left by the time that dark matter (and other matter) first decoupled, or was produced by decay. The different matter components then all have perturbations proportional to the curvature perturbation, so there are no isocurvature perturbations. However, it is possible to produce an observable amount of isocurvature modes by having additional degrees of freedom present during inflation and through reheating. For example, the curvaton model can generate correlated adiabatic and isocurvature modes from a second field (Mollerach 1990; Lyth & Wands 2002).

Isocurvature modes describe relative perturbations between the different species (Bucher et al. 2001b), with perhaps the simplest being a perturbation in the baryonic or dark matter sector (relative to the radiation). However, only one total matter isocurvature mode is observable in the linear CMB (in the accurate approximation in which the baryons are pressureless); a compensated mode (between the baryons and the cold dark matter) with $\delta\rho_b = -\delta\rho_c$ has no net density perturbation, and produces no CMB anisotropies (Gordon & Lewis 2003; Grin et al. 2011; Grin et al. 2014). It is possible to generate isocurvature modes in the neutrino sector; however, this requires interaction of an additional perturbed super-horizon field with neutrinos after they have decoupled, and hence is harder to achieve. Finally, neutrino velocity potential and vorticity modes are other possible consistent perturbations to the photon-neutrino fluid after neutrino decoupling. However, they are essentially impossible to excite, since they consist of photon and neutrino fluids coherently moving in opposite directions on super-horizon scales (although the relative velocity would have been zero before neutrino decoupling).

Planck Collaboration XXII (2014) presented constraints on a variety of general isocurvature models using the *Planck* temperature data, finding consistency with adiabaticity, though with

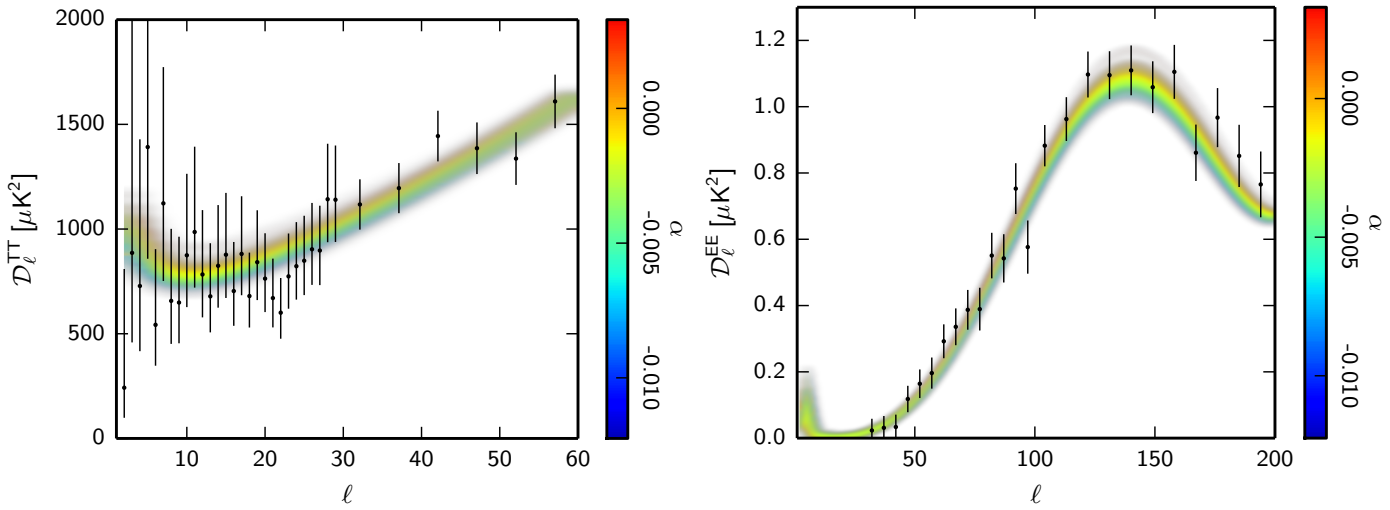

Fig. 25. Power spectra drawn from the *Planck* TT+lowP posterior for the correlated matter isocurvature model, colour-coded by the value of the isocurvature amplitude parameter α, compared to the *Planck* data points. The *left-hand figure* shows how the negatively-correlated modes lower the large-scale temperature spectrum, slightly improving the fit at low multipoles. Including polarization, the negatively-correlated modes are disfavoured, as illustrated at the first acoustic peak in EE on the right-hand plot. Data points at $\ell < 30$ are not shown for polarization, as they are included with both the default temperature (i.e., TT+lowP) and polarization (i.e., TT,TE,EE+lowP) likelihood combinations.

some mild preference for isocurvature models that reduce the power at low multipoles to provide a better match to the *Planck* temperature spectrum at $\ell \lesssim 50$. For matter isocurvature perturbations, the photons are initially unperturbed but perturbations develop as the Universe becomes more matter dominated. As a result, the phase of the acoustic oscillations differs from adiabatic modes; this is most clearly distinctive with the addition of polarization data (Bucher et al. 2001a).

An extended analysis of isocurvature models is given in Planck Collaboration XX (2016). Here we focus on a simple illustrative case of a totally-correlated matter isocurvature mode. We define an isocurvature amplitude parameter α, such that[27]

$$S_{\rm m} = {\rm sgn}(\alpha)\sqrt{\frac{|\alpha|}{1-|\alpha|}}\zeta, \tag{43}$$

where ζ is the primordial curvature perturbation. Here $S_{\rm m}$ is the total matter isocurvature mode, defined as the observable sum of the baryon and CDM isocurvature modes, i.e., $S_{\rm m} = S_{\rm c} + S_{\rm b}(\rho_{\rm b}/\rho_{\rm c})$, where

$$S_i \equiv \frac{\delta\rho_i}{\rho_i} - \frac{3\delta\rho_\gamma}{4\rho_\gamma}. \tag{44}$$

All modes are assumed to have a power spectrum with the same spectral index $n_{\rm s}$, so that α is independent of scale. For positive α this agrees with the definitions in Bean et al. (2006) and Larson et al. (2011) for α_{-1}, but also allows for the correlation to have the opposite sign. Approximately, ${\rm sgn}(\alpha)\,\alpha^2 \approx B_{\rm c}$, where $B_{\rm c}$ is the CDM version of the amplitude defined as in Amendola et al. (2002). Note that in our conventions, negative values of α *lower* the Sachs-Wolfe contribution to the large-scale TT power spectrum. We caution the reader that this convention differs from some others, e.g., Larson et al. (2011).

Planck constraints on the correlated isocurvature amplitude are shown in Fig. 24, with and without high-multipole polarization. The corresponding marginalized limit from the temperature data is

$$\alpha = -0.0025^{+0.0035}_{-0.0047} \quad (95\%, \textit{Planck}\ \text{TT+lowP}), \tag{45}$$

which is significantly tightened around zero when *Planck* polarization information is included at high multipoles:

$$\alpha = 0.0003^{+0.0016}_{-0.0012} \quad (95\%, \textit{Planck}\ \text{TT,TE,EE+lowP}). \tag{46}$$

This strongly limits the isocurvature contribution to be less than about 3% of the adiabatic modes. Figure 25 shows how models with negative correlation parameter, α, fit the temperature data at low multipoles slightly better than models with $\alpha = 0$; however, these models are disfavoured from the corresponding change in the polarization acoustic peaks.

In this model most of the gain in sensitivity comes from relatively large scales, $\ell \lesssim 300$, where the correlated isocurvature modes with delayed phase change the first polarization acoustic peak ($\ell \approx 140$) significantly more than in temperature (Bucher et al. 2001a). The polarization data are not entirely robust to systematics on these scales, but in this case the result appears to be quite stable between the different likelihood codes. However, it should be noted that a particularly low point in the TE spectrum at $\ell \approx 160$ (see Fig. 3) pulls in the direction of positive α, and could be giving an artificially strong constraint if this were caused by an unidentified systematic.

6.2.4. Curvature

The simplifying assumptions of large-scale homogeneity and isotropy lead to the familiar Friedman-Lemaître-Robertson-Walker (FLRW) metric that appears to be an accurate description of our Universe. The base ΛCDM cosmology assumes an FLRW metric with a flat 3-space. This is a very restrictive assumption that needs to be tested empirically. In this subsection, we investigate constraints on the parameter Ω_K, where for ΛCDM models $\Omega_K \equiv 1 - \Omega_{\rm m} - \Omega_\Lambda$. For FLRW models $\Omega_K > 0$ corresponds to negatively-curved 3-geometries while $\Omega_K < 0$ corresponds to positively-curved 3-geometries. Even with perfect data within our past lightcone, our inference of the curvature

[27] Planck Collaboration XX (2016) gives equivalent one-tailed constraints on $\beta_{\rm iso} = |\alpha|$, where the correlated and anti-correlated cases are considered separately.

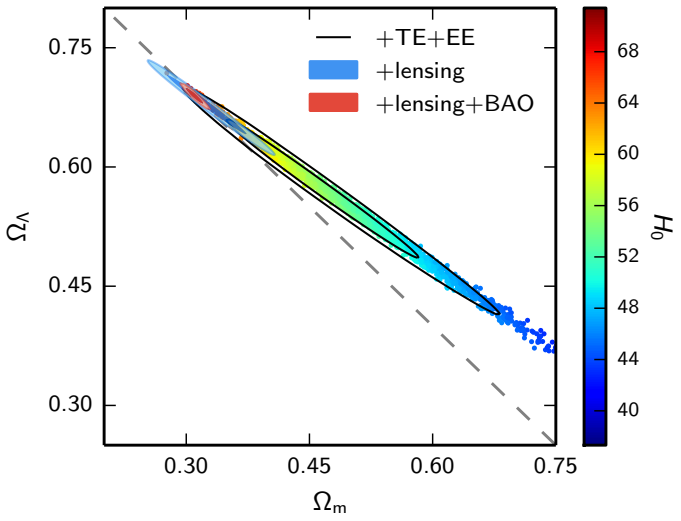

Fig. 26. Constraints in the Ω_m–Ω_Λ plane from the *Planck* TT+lowP data (samples; colour-coded by the value of H_0) and *Planck* TT,TE,EE+lowP (solid contours). The geometric degeneracy between Ω_m and Ω_Λ is partially broken because of the effect of lensing on the temperature and polarization power spectra. These limits are improved significantly by the inclusion of the *Planck* lensing reconstruction (blue contours) and BAO (solid red contours). The red contours tightly constrain the geometry of our Universe to be nearly flat.

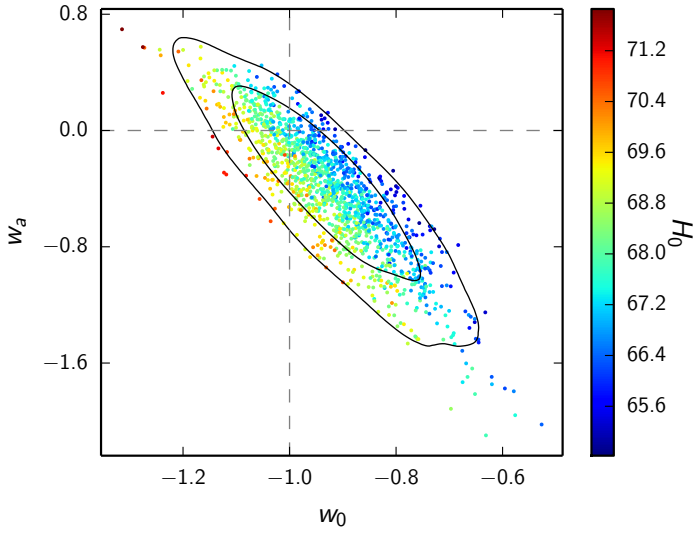

Fig. 27. Samples from the distribution of the dark energy parameters w_0 and w_a using *Planck* TT+lowP+BAO+JLA data, colour-coded by the value of the Hubble parameter H_0. Contours show the corresponding 68% and 95% limits. Dashed grey lines intersect at the point in parameter space corresponding to a cosmological constant.

Ω_K is limited by the cosmic variance of curvature perturbations that are still super-horizon at the present, since these cannot be distinguished from background curvature within our observable volume.

The parameter Ω_K decreases exponentially with time during inflation, but grows only as a power law during the radiation and matter-dominated phases, so the standard inflationary prediction has been that curvature should be unobservably small today. Nevertheless, by fine-tuning parameters it is possible to devise inflationary models that generate open (e.g., Bucher et al. 1995; Linde 1999) or closed universes (e.g., Linde 2003). Even more speculatively, there has been interest recently in multiverse models, in which topologically-open "pocket universes" form by bubble nucleation (e.g., Coleman & De Luccia 1980; Gott 1982) between different vacua of a "string landscape" (e.g., Freivogel et al. 2006; Bousso et al. 2015). Clearly, the detection of a significant deviation from $\Omega_K = 0$ would have profound consequences for inflation theory and fundamental physics.

The *Planck* power spectra give the constraint

$$\Omega_K = -0.052^{+0.049}_{-0.055} \quad (95\%, \textit{Planck}\ \mathrm{TT{+}lowP}). \tag{47}$$

The well-known geometric degeneracy (Bond et al. 1997; Zaldarriaga et al. 1997) allows for the small-scale linear CMB spectrum to remain almost unchanged if changes in Ω_K are compensated by changes in H_0 to obtain the same angular diameter distance to last scattering. The *Planck* constraint is therefore mainly determined by the (wide) priors on H_0, and the effect of lensing smoothing on the power spectra. As discussed in Sect. 5.1, the *Planck* temperature power spectra show a slight preference for more lensing than expected in the base ΛCDM cosmology, and since positive curvature increases the amplitude of the lensing signal, this preference also drives Ω_K towards negative values.

Taken at face value, Eq. (47) represents a detection of positive curvature at just over 2σ, largely via the impact of lensing on the power spectra. One might wonder whether this is mainly a parameter volume effect, but that is not the case, since the best fit closed model has $\Delta\chi^2 \approx 6$ relative to base ΛCDM, and the fit is improved over almost all the posterior volume, with the mean improvement being $\langle\Delta\chi^2\rangle \approx 5$ (very similar to the phenomenological case of ΛCDM+A_L). Addition of the *Planck* polarization spectra shifts Ω_K towards zero by $\Delta\Omega_K \approx 0.015$:

$$\Omega_K = -0.040^{+0.038}_{-0.041} \quad (95\%, \textit{Planck}\ \mathrm{TT,TE,EE{+}lowP}), \tag{48}$$

but Ω_K remains negative at just over 2σ.

What's more, the lensing reconstruction from *Planck* measures the lensing amplitude directly and, as discussed in Sect. 5.1, this does *not* prefer more lensing than base ΛCDM. The combined constraint shows impressive consistency with a flat universe:

$$\Omega_K = -0.005^{+0.016}_{-0.017} \quad (95\%, \textit{Planck}\ \mathrm{TT{+}lowP{+}lensing}). \tag{49}$$

The dramatic improvement in the error bar is another illustration of the power of the lensing reconstruction from *Planck*.

The constraint can be sharpened further by adding external data that break the main geometric degeneracy. Combining the *Planck* data with BAO, we find

$$\Omega_K = 0.000 \pm 0.005 \quad (95\%,\ \textit{Planck}\ \mathrm{TT{+}lowP{+}lensing{+}BAO}). \tag{50}$$

This constraint is unchanged at the quoted precision if we add the JLA supernovae data and the H_0 prior of Eq. (30).

Figure 26 illustrates these results in the Ω_m–Ω_Λ plane. We adopt Eq. (50) as our most reliable constraint on spatial curvature. Our Universe appears to be spatially flat to a 1σ accuracy of 0.25%.

6.3. Dark energy

The physical explanation for the observed accelerated expansion of the Universe is currently not known. In standard ΛCDM the acceleration is provided by a cosmological constant, i.e., an additional fluid satisfying an equation of state $w \equiv p_{DE}/\rho_{DE} = -1$.

However, there are many possible alternatives, typically described either in terms of extra degrees of freedom associated with scalar fields or modifications of general relativity on cosmological scales (for reviews see, e.g., Copeland et al. 2006; Tsujikawa 2010). A detailed study of these models and the constraints imposed by *Planck* and other data are presented in a separate paper, Planck Collaboration XIV (2016).

Here we will limit ourselves to the most basic extensions of ΛCDM, which can be phenomenologically described in terms of the equation of state parameter w alone. Specifically we will use the `camb` implementation of the "parameterized post-Friedmann" (PPF) framework of Hu & Sawicki (2007) and Fang et al. (2008) to test whether there is any evidence that w varies with time. This framework aims to recover the behaviour of canonical (i.e., those with a standard kinetic term) scalar field cosmologies minimally coupled to gravity when $w \geq -1$, and accurately approximates them for values $w \approx -1$. In these models the speed of sound is equal to the speed of light, so that the clustering of the dark energy inside the horizon is strongly suppressed. The advantage of using the PPF formalism is that it is possible to study the phantom domain, $w < -1$, including transitions across the "phantom barrier", $w = -1$, which is not possible for canonical scalar fields.

The CMB temperature data alone do not tightly constrain w, because of a strong geometrical degeneracy, even for spatially-flat models. From *Planck* we find

$$w = -1.54^{+0.62}_{-0.50} \quad (95\%, \textit{Planck}\ \mathrm{TT{+}lowP}), \tag{51}$$

i.e., almost a 2σ shift into the phantom domain. This is partly, but not entirely, a parameter volume effect, with the average effective χ^2 improving by $\langle \Delta\chi^2 \rangle \approx 2$ compared to base ΛCDM. This is consistent with the preference for a higher lensing amplitude discussed in Sect. 5.1.2, improving the fit in the $w < -1$ region, where the lensing smoothing amplitude becomes slightly larger. However, the lower limit in Eq. (51) is largely determined by the (arbitrary) prior $H_0 < 100$ km s^{-1}Mpc^{-1}, chosen for the Hubble parameter. Much of the posterior volume in the phantom region is associated with extreme values for cosmological parameters, which are excluded by other astrophysical data. The mild tension with base ΛCDM disappears as we add more data that break the geometrical degeneracy. Adding *Planck* lensing and BAO, JLA and H_0 ("ext") gives the 95% constraints

$$w = -1.023^{+0.091}_{-0.096} \quad \textit{Planck}\ \mathrm{TT{+}lowP{+}ext}, \tag{52a}$$

$$w = -1.006^{+0.085}_{-0.091} \quad \textit{Planck}\ \mathrm{TT{+}lowP{+}lensing{+}ext}, \tag{52b}$$

$$w = -1.019^{+0.075}_{-0.080} \quad \textit{Planck}\ \mathrm{TT, TE, EE{+}lowP{+}lensing{+}ext}. \tag{52c}$$

The addition of *Planck* lensing, or using the full *Planck* temperature+polarization likelihood together with the BAO, JLA, and H_0 data does not substantially improve the constraint of Eq. (52a). All of these data set combinations are compatible with the base ΛCDM value of $w = -1$. In PCP13, we conservatively quoted $w = -1.13^{+0.24}_{-0.25}$, based on combining *Planck* with BAO, as our most reliable limit on w. The errors in Eqs. (52a)–(52c) are substantially smaller, mainly because of the addition of the JLA SNe data, which offer a sensitive probe of the dark energy equation of state at $z \lesssim 1$. In PCP13, the addition of the SNLS SNe data pulled w into the phantom domain at the 2σ level, reflecting the tension between the SNLS sample and the *Planck* 2013 base ΛCDM parameters. As noted in Sect. 5.3, this discrepancy is no longer present, following improved photometric calibrations of the SNe data in the JLA sample. One consequence of this is the tightening of the errors in Eqs. (52a)–(52c) around the ΛCDM value $w = -1$ when we combine the JLA sample with *Planck*.

If w differs from -1, it is likely to change with time. We consider here the case of a Taylor expansion of w at first order in the scale factor, parameterized by

$$w = w_0 + (1 - a)w_a. \tag{53}$$

More complex models of dynamical dark energy are discussed in Planck Collaboration XIV (2016). Figure 27 shows the 2D marginalized posterior distribution for w_0 and w_a for the combination *Planck*+BAO+JLA. The JLA SNe data are again crucial in breaking the geometrical degeneracy at low redshift and with these data we find no evidence for a departure from the base ΛCDM cosmology. The points in Fig. 27 show samples from these chains colour-coded by the value of H_0. From these MCMC chains, we find $H_0 = (68.2 \pm 1.1)$ km s^{-1}Mpc^{-1}. Much higher values of H_0 would favour the phantom regime, $w < -1$.

As pointed out in Sects. 5.5.2 and 5.6 the CFHTLenS weak lensing data are in tension with the *Planck* base ΛCDM parameters. Examples of this tension can be seen in investigations of dark energy and modified gravity, since some of these models can modify the growth rate of fluctuations from the base ΛCDM predictions. This tension can be seen even in the simple model of Eq. (53). The green regions in Fig. 28 show 68% and 95% contours in the w_0–w_a plane for *Planck* TT+lowP combined with the CFHTLenS H13 data. In this example, we have applied ultra-conservative cuts, excluding ξ_- entirely and excluding measurements with $\theta < 17'$ in ξ_+ for all tomographic redshift bins. As discussed in Planck Collaboration XIV (2016), with these cuts the CFHTLenS data are insensitive to modelling the nonlinear evolution of the power spectrum, but this reduction in sensitivity comes at the expense of reducing the statistical power of the weak lensing data. Nevertheless, Fig. 28 shows that the combination of *Planck*+CFHTLenS pulls the contours into the phantom domain and is discrepant with base ΛCDM at about the 2σ level. The *Planck*+CFHTLenS data also favour a high value of H_0. If we add the (relatively weak) H_0 prior of Eq. (30), the contours (shown in cyan) in Fig. 28 shift towards $w = -1$. It therefore seems unlikely that the tension between *Planck* and CFHTLenS can be resolved by allowing a time-variable equation of state for dark energy.

A much more extensive investigation of models of dark energy and also models of modified gravity can be found in Planck Collaboration XIV (2016). The main conclusions of that analysis are:

- an investigation of more general time-variations of the equation of state shows a high degree of consistency with $w = -1$;
- a study of several dark energy and modified gravity models either finds compatibility with base ΛCDM, or mild tensions, which are driven mainly by external data sets.

6.4. Neutrino physics and constraints on relativistic components

In the following subsections, we update *Planck* constraints on the mass of standard (active) neutrinos, additional relativistic degrees of freedom, models with a combination of the two, and models with massive sterile neutrinos. In each subsection we emphasize the *Planck*-only constraint, and the implications of the *Planck* result for late-time cosmological parameters measured from other observations. We then give a brief discussion of tensions between *Planck* and some discordant external data, and

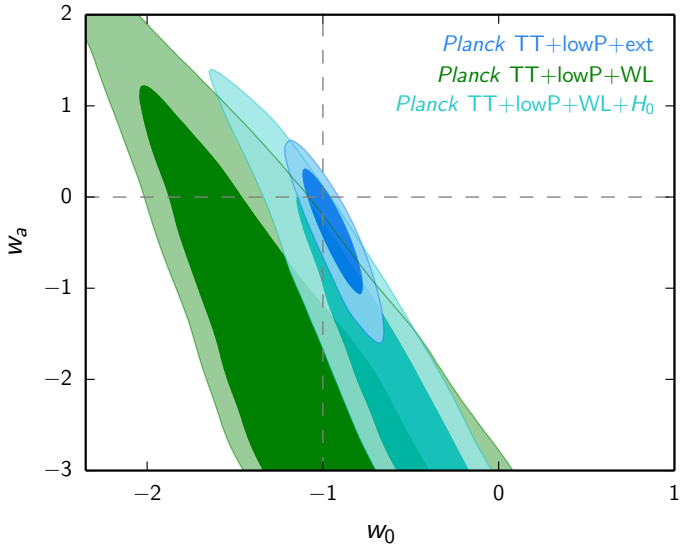

Fig. 28. Marginalized posterior distributions for (w_0, w_a) for various data combinations. We show *Planck* TT+lowP in combination with BAO, JLA, H_0 ("ext"), and two data combinations that add the CFHTLenS data with ultra-conservative cuts as described in the text (denoted "WL"). Dashed grey lines show the parameter values corresponding to a cosmological constant.

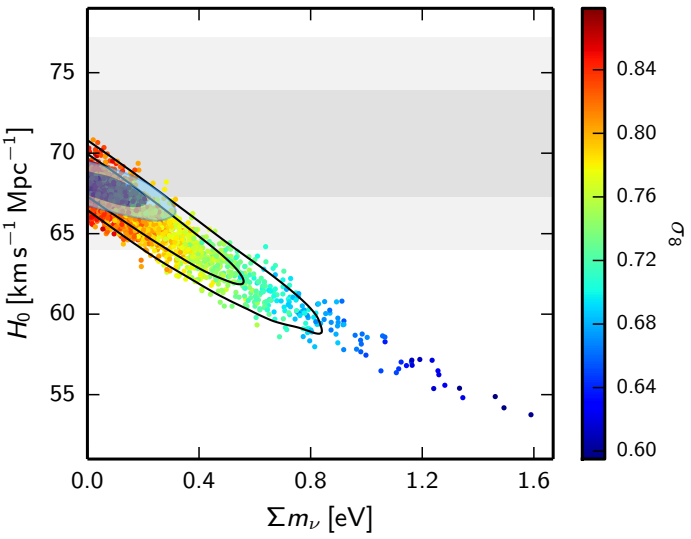

Fig. 29. Samples from the *Planck* TT+lowP posterior in the $\sum m_\nu$–H_0 plane, colour-coded by σ_8. Higher $\sum m_\nu$ damps the matter fluctuation amplitude σ_8, but also decreases H_0. The grey bands show the direct measurement, $H_0 = (70.6 \pm 3.3)$ km s^{-1}Mpc^{-1}, Eq. (30). Solid black contours show the constraint from *Planck* TT+lowP+lensing (which mildly prefers larger masses), and filled contours show the constraints from *Planck* TT+lowP+lensing+BAO.

assess whether any of these model extensions can help to resolve them. Finally we provide constraints on neutrino interactions.

6.4.1. Constraints on the total mass of active neutrinos

Detection of neutrino oscillations has proved that neutrinos have mass (see, e.g., Lesgourgues & Pastor 2006 and Nakamura & Petcov 2014 for reviews). The *Planck* base ΛCDM model assumes a normal mass hierarchy with $\sum m_\nu \approx 0.06$ eV (dominated by the heaviest neutrino mass eigenstate) but there are other possibilities, including a degenerate hierarchy with $\sum m_\nu \gtrsim 0.1$ eV. At this time there are no compelling theoretical reasons to strongly prefer any of these possibilities, so allowing for larger neutrino masses is perhaps one of the most well-motivated extensions to base ΛCDM considered in this paper. There has also been significant interest recently in larger neutrino masses as a possible way to lower σ_8 (the late-time fluctuation amplitude), and thereby reconcile *Planck* with weak lensing measurements and the abundance of rich clusters (see Sects. 5.5 and 5.6). Though model dependent, neutrino mass constraints from cosmology are already significantly stronger than those from tritium β-decay experiments (see, e.g., Drexlin et al. 2013).

Here we give constraints assuming three species of degenerate massive neutrinos, neglecting the small differences in mass expected from the observed mass splittings. At the level of sensitivity of *Planck* this is an accurate approximation, but note that it does not quite match continuously on to the base ΛCDM model (which assumes two massless and one massive neutrino with $\sum m_\nu = 0.06$ eV). We assume that the neutrino mass is constant, and that the distribution function is Fermi-Dirac with zero chemical potential.

Masses well below 1 eV have only a mild effect on the shape of the CMB power spectra, since they became non-relativistic after recombination. The effect on the background cosmology can be compensated by changes in H_0, to ensure the same observed acoustic peak scale θ_*. There is, however, some sensitivity of the CMB anisotropies to neutrino masses as the neutrinos start to become less relativistic at recombination (modifying the early ISW effect), and from the late-time effect of lensing on the power spectrum. The *Planck* power spectrum (95%) constraints are

$$\sum m_\nu < 0.72 \text{ eV} \quad \textit{Planck} \text{ TT+lowP}, \tag{54a}$$

$$\sum m_\nu < 0.21 \text{ eV} \quad \textit{Planck} \text{ TT+lowP+BAO}, \tag{54b}$$

$$\sum m_\nu < 0.49 \text{ eV} \quad \textit{Planck} \text{ TT, TE, EE+lowP}, \tag{54c}$$

$$\sum m_\nu < 0.17 \text{ eV} \quad \textit{Planck} \text{ TT, TE, EE+lowP+BAO}. \tag{54d}$$

The *Planck* TT+lowP constraint has a broad tail to high masses, as shown in Fig. 29, which also illustrates the acoustic scale degeneracy with H_0. Larger masses imply a lower σ_8 through the effects of neutrino free-streaming on structure formation, but the larger masses also require a lower Hubble constant, leading to possible tensions with direct measurements of H_0. Masses below about 0.4 eV can provide an acceptable fit to the direct H_0 measurements, and adding the BAO data helps to break the acoustic scale degeneracy and tightens the constraint on $\sum m_\nu$ substantially. Adding *Planck* polarization data at high multipoles produces a relatively small improvement to the *Planck* TT+lowP+BAO constraint (and the improvement is even smaller with the alternative `CamSpec` likelihood), so we consider the *TT* results to be our most reliable constraints.

The constraint of Eq. (54b) is consistent with the 95% limit of $\sum m_\nu < 0.23$ eV reported in PCP13 for *Planck*+BAO. The limits are similar because the linear CMB is insensitive to the mass of neutrinos that are relativistic at recombination. There is little to be gained from improved measurement of the CMB temperature power spectra, though improved external data can help to break the geometric degeneracy to higher precision. CMB lensing can also provide additional information at lower redshifts, and future high-resolution CMB polarization measurements that accurately reconstruct the lensing potential can probe much smaller masses (see, e.g. Abazajian et al. 2015b).

As discussed in detail in PCP13 and Sect. 5.1, the *Planck* CMB power spectra prefer somewhat more lensing smoothing than predicted in ΛCDM (allowing the lensing amplitude to vary gives $A_{\rm L} > 1$ at just over 2σ). The neutrino mass constraint from the power spectra is therefore quite tight, since increasing the neutrino mass lowers the predicted smoothing even further compared to base ΛCDM. On the other hand the lensing reconstruction data, which directly probes the lensing power, prefers lensing amplitudes slightly below (but consistent with) the base ΛCDM prediction (Eq. (18)). The *Planck*+lensing constraint therefore pulls the constraints slightly away from zero towards higher neutrino masses, as shown in Fig. 30. Although the posterior has less weight at zero, the lensing data are incompatible with very large neutrino masses so the *Planck*+lensing 95% limit is actually tighter than the *Planck* TT+lowP result:

$$\sum m_\nu < 0.68 \text{ eV} \quad (95\%, \textit{Planck}\ \text{TT+lowP+lensing}). \tag{55}$$

Adding the polarization spectra improves this constraint slightly to

$$\sum m_\nu < 0.59 \text{ eV} \quad (95\%, \textit{Planck}\ \text{TT,TE,EE+lowP+lensing}). \tag{56}$$

We take the combined constraint that further includes BAO, JLA, and H_0 ("ext") as our best limit:

$$\left.\begin{array}{l} \sum m_\nu < 0.23 \text{ eV} \\ \Omega_\nu h^2 < 0.0025 \end{array}\right\} 95\%, \textit{Planck}\ \text{TT+lowP+lensing+ext}. \tag{57}$$

This is slightly weaker than the constraint from *Planck* TT,TE,EE+lowP+lensing+BAO (which is tighter in both the `CamSpec` and `Plik` likelihoods), but is immune to low level systematics that might affect the constraints from the *Planck* polarization spectra. Equation (57) is therefore a conservative limit. Marginalizing over the range of neutrino masses, the *Planck* constraints on the late-time parameters are[28]

$$\left.\begin{array}{l} H_0 = 67.7 \pm 0.6 \\ \sigma_8 = 0.810^{+0.015}_{-0.012} \end{array}\right\} \textit{Planck}\ \text{TT+lowP+lensing+ext}. \tag{58}$$

For this restricted range of neutrino masses, the impact on the other cosmological parameters is small and, in particular, low values of σ_8 will remain in tension with the parameter space preferred by *Planck*.

The constraint of Eq. (57) is weaker than the constraint of Eq. (54b) excluding lensing, but there is no good reason to disregard the *Planck* lensing information while retaining other astrophysical data. The CMB lensing signal probes very-nearly linear scales and passes many consistency checks over the multipole range used in the *Planck* lensing likelihood (see Sect. 5.1 and Planck Collaboration XV 2016). The situation with galaxy weak lensing is rather different, as discussed in Sect. 5.5.2. In addition to possible observational systematics, the weak lensing data probe lower redshifts than CMB lensing, and smaller spatial scales, where uncertainties in modelling nonlinearities in the matter power spectrum and baryonic feedback become important (Harnois-Déraps et al. 2015).

[28] To simplify the displayed equations, H_0 is given in units of km s^{-1}Mpc^{-1} in this section.

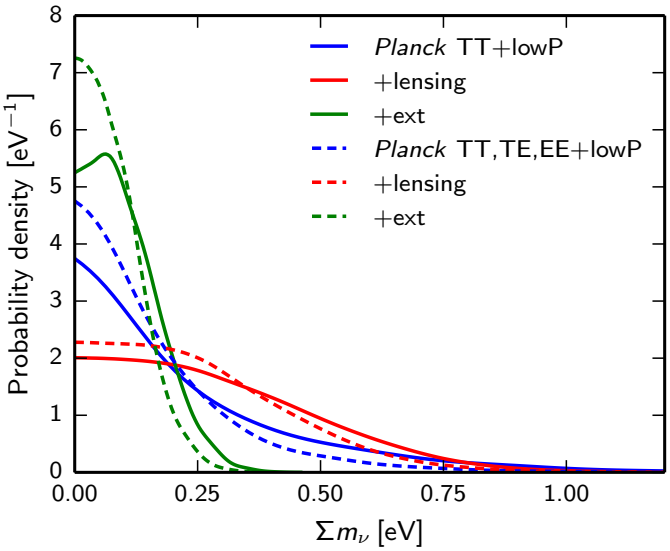

Fig. 30. Constraints on the sum of the neutrino masses for various data combinations.

A larger range of neutrino masses was found by Beutler et al. (2014b) using a combination of RSD, BAO, and weak lensing information. The tension between the RSD results and base ΛCDM was subsequently reduced following the analysis of Samushia et al. (2014), as shown in Fig. 17. Galaxy weak lensing and some cluster constraints remain in tension with base ΛCDM, and we discuss possible neutrino resolutions of these problems in Sect. 6.4.4.

Another way of potentially improving neutrino mass constraints is to use measurements of the Lyα flux power spectrum of high-redshift quasars. Palanque-Delabrouille et al. (2015) have recently reported an analysis of a large sample of quasar spectra from the SDSSIII/BOSS survey. When combining their results with 2013 Planck data, these authors find a bound $\sum m_\nu < 0.15$ eV (95% CL), compatible with the results presented in this section.

An exciting future prospect is the possible direct detection of non-relativistic cosmic neutrinos by capture on tritium, for example with the PTOLEMY experiment (Cocco et al. 2007; Betts et al. 2013; Long et al. 2014). Unfortunately, for the mass range $\sum m_\nu < 0.23$ eV preferred by *Planck*, detection with the first generation experiment will be extremely difficult.

6.4.2. Constraints on $N_{\rm eff}$

Dark radiation density in the early Universe is usually parameterized by $N_{\rm eff}$, defined so that the total relativistic energy density in neutrinos and any other dark radiation is given in terms of the photon density ρ_γ at $T \ll 1$ MeV by

$$\rho = N_{\rm eff} \frac{7}{8} \left(\frac{4}{11}\right)^{4/3} \rho_\gamma. \tag{59}$$

The numerical factors in this equation are included so that $N_{\rm eff} = 3$ for three standard model neutrinos that were thermalized in the early Universe and decoupled well before electron-positron annihilation. The standard cosmological prediction is actually $N_{\rm eff} = 3.046$, since neutrinos are not completely decoupled at electron-positron annihilation and are subsequently slightly heated (Mangano et al. 2002).

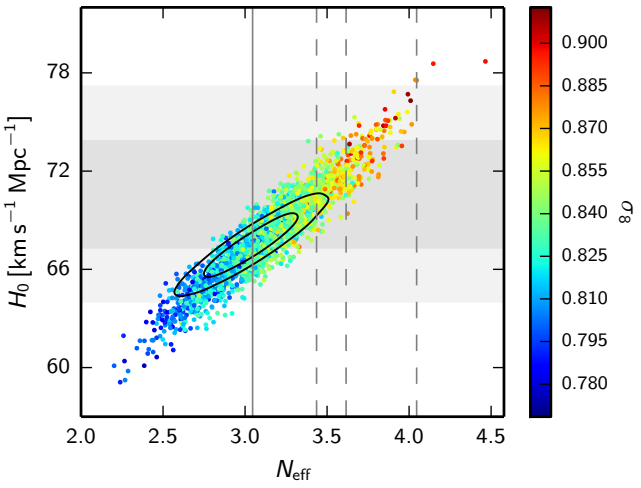

Fig. 31. Samples from *Planck* TT+lowP chains in the $N_{\rm eff}$–H_0 plane, colour-coded by σ_8. The grey bands show the constraint $H_0 = (70.6 \pm 3.3)$ km s^{-1}Mpc^{-1} of Eq. (30). Notice that higher $N_{\rm eff}$ brings H_0 into better consistency with direct measurements, but increases σ_8. Solid black contours show the constraints from *Planck* TT,TE,EE+lowP+BAO. Models with $N_{\rm eff} < 3.046$ (left of the solid vertical line) require photon heating after neutrino decoupling or incomplete thermalization. Dashed vertical lines correspond to specific fully-thermalized particle models, for example one additional massless boson that decoupled around the same time as the neutrinos ($\Delta N_{\rm eff} \approx 0.57$), or before muon annihilation ($\Delta N_{\rm eff} \approx 0.39$), or an additional sterile neutrino that decoupled around the same time as the active neutrinos ($\Delta N_{\rm eff} \approx 1$).

In this section we focus on additional energy density from massless particles. In addition to massless sterile neutrinos, a variety of other particles could contribute to $N_{\rm eff}$. We assume that the additional massless particles are produced well before recombination, and neither interact nor decay, so that their energy density scales with the expansion exactly like massless neutrinos. An additional $\Delta N_{\rm eff} = 1$ could correspond to a fully thermalized sterile neutrino that decoupled at $T \lesssim 100$ MeV; for example, any sterile neutrino with mixing angles large enough to provide a potential resolution to short-baseline reactor neutrino oscillation anomalies would most likely thermalize rapidly in the early Universe. However, this solution to the neutrino oscillation anomalies requires approximately 1-eV sterile neutrinos, rather than the massless case considered in this section; exploration of the two parameters $N_{\rm eff}$ and $\sum m_\nu$ is reported in Sect. 6.4.3. For a review of sterile neutrinos see Abazajian et al. (2012).

More generally the additional radiation does not need to be fully thermalized, for example there are many possible models of non-thermal radiation production via particle decays (see, e.g., Hasenkamp & Kersten 2013; Conlon & Marsh 2013). The radiation could also be produced at temperatures $T > 100$ MeV, in which case typically $\Delta N_{\rm eff} < 1$ for each additional species, since heating by photon production at muon annihilation (corresponding to $T \approx 100$ MeV) decreases the fractional importance of the additional component at the later times relevant for the CMB. For particles produced at $T \gg 100$ MeV the density would be diluted even more by numerous phase transitions and particle annihilations, and give $\Delta N_{\rm eff} \ll 1$. Furthermore, if the particle is not fermionic, the factors entering the entropy conservation equation are different, and even thermalized particles could give specific fractional values of $\Delta N_{\rm eff}$. For example Weinberg (2013) considers the case of a thermalized massless boson, which contributes $\Delta N_{\rm eff} = 4/7 \approx 0.57$ if it decouples in the range 0.5 MeV $< T <$ 100 MeV like the neutrinos, or $\Delta N_{\rm eff} \approx 0.39$ if it decouples at $T > 100$ MeV (before the photon production at muon annihilation, hence undergoing fractional dilution).

In this paper we follow the usual phenomenological approach, where one constrains $N_{\rm eff}$ as a free parameter with a wide flat prior, although we comment on a few discrete cases separately below. Values of $N_{\rm eff} < 3.046$ are less well motivated, since they would require the standard neutrinos to be incompletely thermalized or additional photon production after neutrino decoupling, but we include this range for completeness.

Figure 31 shows that *Planck* is entirely consistent with the standard value $N_{\rm eff} = 3.046$. However, a significant density of additional radiation is still allowed, with the (68%) constraints

$$N_{\rm eff} = 3.13 \pm 0.32 \quad \textit{Planck}\ \text{TT+lowP}, \tag{60a}$$
$$N_{\rm eff} = 3.15 \pm 0.23 \quad \textit{Planck}\ \text{TT+lowP+BAO}, \tag{60b}$$
$$N_{\rm eff} = 2.99 \pm 0.20 \quad \textit{Planck}\ \text{TT, TE, EE+lowP}, \tag{60c}$$
$$N_{\rm eff} = 3.04 \pm 0.18 \quad \textit{Planck}\ \text{TT, TE, EE+lowP+BAO}. \tag{60d}$$

Notice the significantly tighter constraint with the inclusion of *Planck* high-ℓ polarization, with $\Delta N_{\rm eff} < 1$ at over 4σ from *Planck* alone. This constraint is not very stable between likelihoods, with the `CamSpec` likelihood giving a roughly 0.8σ *lower* value of $N_{\rm eff}$. However, the strong limit from polarization is also consistent with the joint *Planck* TT+lowP+BAO result, so Eq. (60b) leads to the robust conclusion that $\Delta N_{\rm eff} < 1$ at over 3σ. The addition of *Planck* lensing has very little effect on this constraint.

For $N_{\rm eff} > 3$, the *Planck* data favour higher values of the Hubble parameter than the *Planck* base ΛCDM value, which as discussed in Sect. 5.4 may be in better agreement with some direct measurements of H_0 . This is because *Planck* accurately measures the acoustic scale $r_*/D_{\rm A}$; increasing $N_{\rm eff}$ means (via the Friedmann equation) that the early Universe expands faster, so the sound horizon at recombination, r_*, is smaller and hence recombination has to be closer (larger H_0 and hence smaller $D_{\rm A}$) for it to subtend the same angular size observed by *Planck*. However, models with $N_{\rm eff} > 3$ and a higher Hubble constant also have higher values of the fluctuation amplitude σ_8, as shown by the coloured samples in Fig. 31. As a result, these models *increase* the tensions between the CMB measurements and astrophysical measurements of σ_8 discussed in Sect. 5.6. It therefore seems unlikely that additional radiation alone can help to resolve tensions with large-scale structure data.

The energy density in the early Universe can also be probed by the predictions of BBN. In particular $\Delta N_{\rm eff} > 0$ increases the primordial expansion rate, leading to earlier freeze-out, with a higher neutron density and hence a greater abundance of helium and deuterium after BBN has completed. A detailed discussion of the implications of *Planck* for BBN is given in Sect. 6.5. Observations of both the primordial helium and deuterium abundance are compatible with the predictions of standard BBN for the *Planck* base ΛCDM value of the baryon density. The *Planck*+BBN constraints on $N_{\rm eff}$ (Eqs. (75) and (76)) are compatible, and slightly tighter than Eq. (60b).

Although there is a large continuous range of plausible $N_{\rm eff}$ values, it is worth mentioning briefly a few of the discrete values from fully thermalized models. This serves as an indication of how strongly *Planck* prefers base ΛCDM, and also how the inferred values of other cosmological parameters might be affected by this particular extension to base ΛCDM. As discussed above, one fully thermalized neutrino ($\Delta N_{\rm eff} \approx 1$) is ruled out at over 3σ, and is disfavoured by $\Delta\chi^2 \approx 8$ compared to base ΛCDM by *Planck* TT+lowP, and much more strongly in combination with

Planck high-ℓ polarization or BAO data. The thermalized boson models that give $\Delta N_{\rm eff} = 0.39$ or $\Delta N_{\rm eff} = 0.57$ are disfavoured by $\Delta\chi^2 \approx 1.5$ and $\Delta\chi^2 \approx 3$, respectively, and are therefore not strongly excluded. We focus on the former, since it is also consistent with the *Planck* TT+lowP+BAO constraint at 2σ. As shown in Fig. 31, larger $N_{\rm eff}$ corresponds to a region of parameter space with significantly higher Hubble parameter,

$$H_0 = 70.6 \pm 1.0 \quad (68\%, \textit{Planck}\ \text{TT+lowP};\ \Delta N_{\rm eff} = 0.39). \quad (61)$$

This can be compared to the direct measurements of H_0 discussed in Sect. 5.4. Evidently, Eq. (61) is consistent with the H_0 prior adopted in this paper (Eq. (30)), but this example shows that an accurate direct measurement of H_0 can potentially provide evidence for new physics beyond that probed by *Planck*. As shown in Fig. 31, the $\Delta N_{\rm eff} = 0.39$ cosmology also has a significantly higher small-scale fluctuation amplitude and the spectral index $n_{\rm s}$ is also bluer, with

$$\left.\begin{aligned}\sigma_8 &= 0.850 \pm 0.015\\ n_{\rm s} &= 0.983 \pm 0.006\end{aligned}\right\}\ \textit{Planck}\ \text{TT+lowP};\ \Delta N_{\rm eff} = 0.39. \quad (62)$$

The σ_8 range in this model is higher than preferred by the *Planck* lensing likelihood in base ΛCDM. However, the fit to the *Planck* lensing likelihood is model dependent and the lensing degeneracy direction also associates high H_0 and low $\Omega_{\rm m}$ values with higher σ_8. The joint *Planck* TT+lowP+lensing constraint does pull σ_8 down slightly to $\sigma_8 = 0.84 \pm 0.01$ and provides an acceptable fit to the *Planck* data. For *Planck* TT+lowP+lensing, the difference in χ^2 between the best fit base ΛCDM model and the extension with $\Delta N_{\rm eff} = 0.39$ is only $\Delta\chi^2_{\rm CMB} \approx 2$. The higher spectral index with $\Delta N_{\rm eff} = 0.39$ gives a decrease in large-scale power, fitting the low $\ell < 30$ *Planck TT* spectrum better by $\Delta\chi^2 \approx 1$, but at the same time the high-ℓ data prefer $\Delta N_{\rm eff} \approx 0$. Correlations with other cosmological parameters can be seen in Fig. 20. Clearly, a very effective way of testing these models would be to obtain reliable, accurate, astrophysical measurements of H_0 and σ_8.

In summary, models with $\Delta N_{\rm eff} = 1$ are disfavoured by *Planck* combined with BAO data at about the 3σ level. Models with fractional changes of $\Delta N_{\rm eff} \approx 0.39$ are mildly disfavoured by *Planck*, but require higher H_0 and σ_8 compared to base ΛCDM.

6.4.3. Simultaneous constraints on $N_{\rm eff}$ and neutrino mass

As discussed in the previous sections, neither a higher neutrino mass nor additional radiation density alone can resolve all of the tensions between *Planck* and other astrophysical data. However, the presence of additional massive particles, such as massive sterile neutrinos, could potentially improve the situation by introducing enough freedom to allow higher values of the Hubble constant *and* lower values of σ_8. As mentioned in Sect. 6.4.2, massive sterile neutrinos offer a possible solution to reactor neutrino oscillation anomalies (Kopp et al. 2013; Giunti et al. 2013) and this has led to significant recent interest in this class of models (Hamann & Hasenkamp 2013; Wyman et al. 2014; Battye & Moss 2014; Leistedt et al. 2014; Bergström et al. 2014; MacCrann et al. 2015). Alternatively, active neutrinos could have significant degenerate masses above the minimal baseline value together with additional massless particles contributing to $N_{\rm eff}$. Many more complicated scenarios could also be envisaged.

In the case of massless radiation density, the cosmological predictions are independent of the actual form of the distribution function, since all particles travel at the speed of light. However, for massive particles the results are more model dependent. To formulate a well-defined model, we follow PCP13 and consider the case of one massive sterile neutrino parameterized by $m^{\rm eff}_{\nu,\,\rm sterile} \equiv (94.1\,\Omega_{\nu,\rm sterile}h^2)$ eV, in addition to the two approximately massless and one massive neutrino of the baseline model. For thermally-distributed sterile neutrinos, $m^{\rm eff}_{\nu,\,\rm sterile}$ is related to the true mass via

$$m^{\rm eff}_{\nu,\,\rm sterile} = (T_{\rm s}/T_\nu)^3 m^{\rm thermal}_{\rm sterile} = (\Delta N_{\rm eff})^{3/4} m^{\rm thermal}_{\rm sterile}, \quad (63)$$

and for the cosmologically-equivalent Dodelson-Widrow (DW) case (Dodelson & Widrow 1994) the relation is given by

$$m^{\rm eff}_{\nu,\,\rm sterile} = \chi_{\rm s}\, m^{\rm DW}_{\rm sterile}, \quad (64)$$

with $\Delta N_{\rm eff} = \chi_{\rm s}$. We impose a prior on the physical thermal mass, $m^{\rm thermal}_{\rm sterile} < 10$ eV, when generating parameter chains, to exclude regions of parameter space in which the particles are so massive that their effect on the CMB spectra is identical to that of cold dark matter. Although we consider only the specific case of one massive sterile neutrino with a thermal (or DW) distribution, our constraints will be reasonably accurate for other models, for example eV-mass particles produced as non-thermal decay products (Hasenkamp 2014).

Figure 32 shows that although *Planck* is perfectly consistent with no massive sterile neutrinos, a significant region of parameter space with fractional $\Delta N_{\rm eff}$ is allowed, where σ_8 is lower than in the base ΛCDM model. This is also the case for massless sterile neutrinos combined with massive active neutrinos. In the single massive sterile model, the combined constraints are

$$\left.\begin{aligned}N_{\rm eff} &< 3.7\\ m^{\rm eff}_{\nu,\,\rm sterile} &< 0.52\ \text{eV}\end{aligned}\right\}\ 95\%,\ \textit{Planck}\ \text{TT+lowP+lensing+BAO}. \quad (65)$$

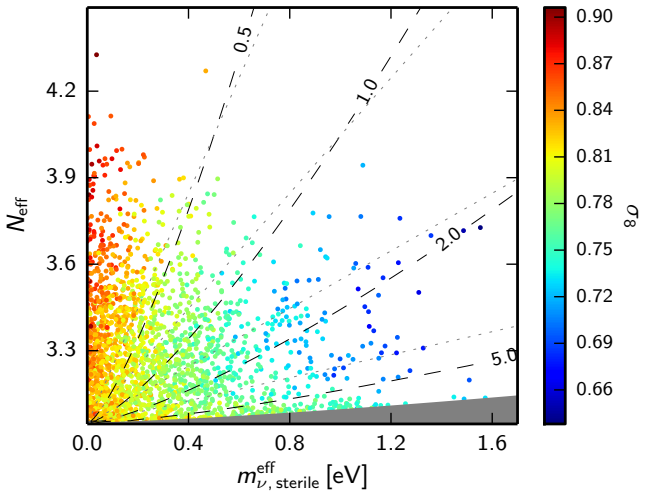

Fig. 32. Samples from *Planck* TT+lowP in the $N_{\rm eff}$–$m^{\rm eff}_{\nu,\,\rm sterile}$ plane, colour-coded by σ_8, for models with one massive sterile neutrino family, with effective mass $m^{\rm eff}_{\nu,\,\rm sterile}$, and the three active neutrinos as in the base ΛCDM model. The physical mass of the sterile neutrino in the thermal scenario, $m^{\rm thermal}_{\rm sterile}$, is constant along the grey dashed lines, with the indicated mass in eV; the grey shading shows the region excluded by our prior $m^{\rm thermal}_{\rm sterile} < 10$ eV, which cuts out most of the area where the neutrinos behave nearly like dark matter. The physical mass in the Dodelson-Widrow scenario, $m^{\rm DW}_{\rm sterile}$, is constant along the dotted lines (with the value indicated on the adjacent dashed lines).

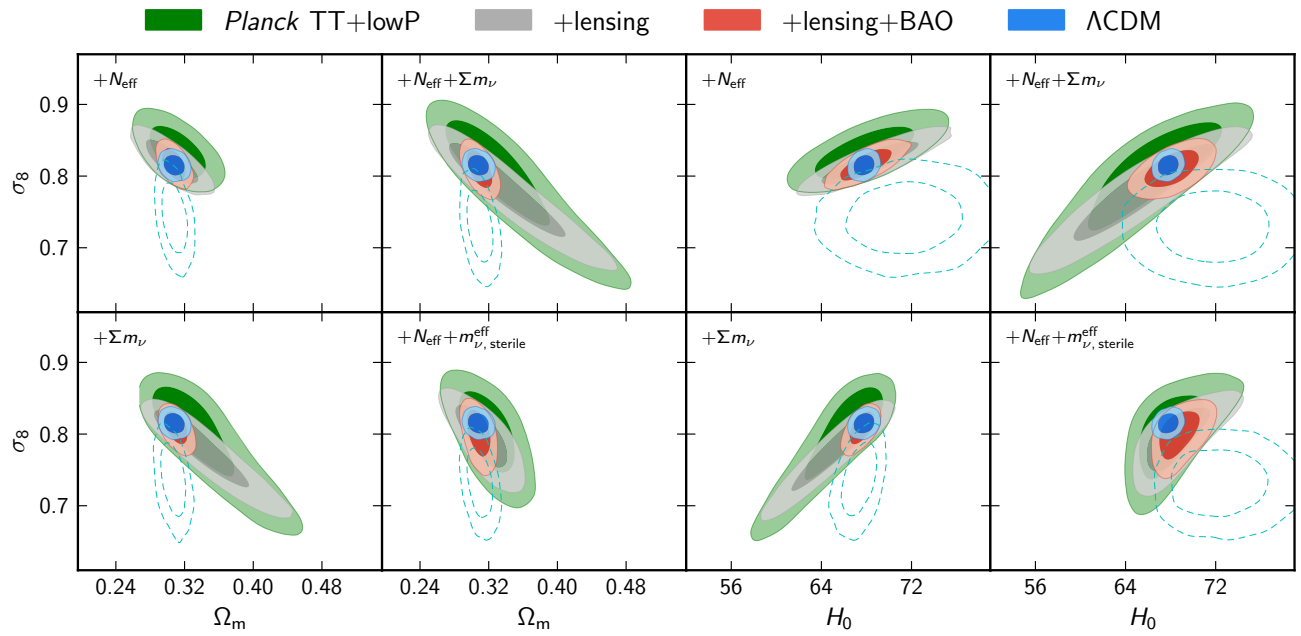

Fig. 33. 68% and 95% constraints from *Planck* TT+lowP (green), *Planck* TT+lowP+lensing (grey), and *Planck* TT+lowP+lensing+BAO (red) on the late-Universe parameters H_0, σ_8, and Ω_m in various neutrino extensions of the base ΛCDM model. The blue contours show the base ΛCDM constraints from *Planck* TT+lowP+lensing+BAO. The dashed cyan contours show joint constraints from the H13 CFHTLenS galaxy weak lensing likelihood (with angular cuts as in Fig. 18) at constant CMB acoustic scale θ_{MC} (fixed to the *Planck* TT+lowP ΛCDM best fit) combined with BAO and the Hubble constant measurement of Eq. (30). These additional constraints break large parameter degeneracies in the weak lensing likelihood that would otherwise obscure the comparison with the *Planck* contours. Here priors on other parameters applied to the CFHTLenS analysis are as described in Sect. 5.5.2.

The upper tail of $m^{\rm eff}_{\nu,\,\rm sterile}$ is largely associated with high physical masses near to the prior cutoff; if instead we restrict to the region where $m^{\rm thermal}_{\rm sterile} < 2$ eV the constraint is

$$\left.\begin{array}{r} N_{\rm eff} < 3.7 \\ m^{\rm eff}_{\nu,\,\rm sterile} < 0.38 \text{ eV} \end{array}\right\} \ 95\%,\ \textit{Planck}\ \text{TT+lowP+lensing+BAO}. \tag{66}$$

Massive sterile neutrinos with mixing angles large enough to help resolve the reactor anomalies would typically imply full thermalization in the early Universe, and hence give $\Delta N_{\rm eff} = 1$ for each additional species. Such a high value of $N_{\rm eff}$, especially combined with $m_{\rm sterile} \approx 1$ eV, as required by reactor anomaly solutions, were virtually ruled out by previous cosmological data (Mirizzi et al. 2013; Archidiacono et al. 2013a; Gariazzo et al. 2013). This conclusion is strengthened by the analysis presented here, since $N_{\rm eff} = 4$ is excluded at greater than 99% confidence. Unfortunately, there does not appear to be a consistent resolution to the reactor anomalies, unless thermalization of the massive neutrinos can be suppressed, for example, by large lepton asymmetry, new interactions, or particle decay (see Gariazzo et al. 2014; Bergström et al. 2014, and references therein).

We have also considered the case of additional radiation and degenerate massive active neutrinos, with the combined constraint

$$\left.\begin{array}{r} N_{\rm eff} = 3.2 \pm 0.5 \\ \sum m_\nu < 0.32 \text{ eV} \end{array}\right\} \ 95\%,\ \textit{Planck}\ \text{TT+lowP+lensing+BAO}. \tag{67}$$

Again *Planck* shows no evidence for a deviation from the base ΛCDM model.

6.4.4. Neutrino models and tension with external data

The extended models discussed in this section allow *Planck* to be consistent with a wider range of late-Universe parameters than in base ΛCDM. Figure 33 summarizes the constraints on Ω_m, σ_8, and H_0 for the various models that we have considered. The inferred Hubble parameter can increase or decrease, as required to maintain the observed acoustic scale, depending on the relative contribution of additional radiation (changing the sound horizon) and neutrino mass (changing mainly the angular diameter distance). However, all of the models follow similar degeneracy directions in the Ω_m–σ_8 and H_0–σ_8 planes, so these models remain predictive: *large common areas of the parameter space are excluded in all of these models*. The two-parameter extensions are required to fit substantially lower values of σ_8 without also decreasing H_0 below the values determined from direct measurements, but the scope for doing this is clearly limited.

External data sets need to be reanalysed consistently in extended models, since the extensions change the growth of structure, angular distances, and the matter-radiation equality scale. For example, the dashed lines in Fig. 33 show how different models affect the CFHTLenS galaxy weak lensing constraints from Heymans et al. (2013) (see Sect. 5.5.2), when restricted to the region of parameter space consistent with the *Planck* acoustic scale measurements and the local Hubble parameter. The filled green, grey, and red contours in Fig. 33 show the CMB constraints on these models for various data combinations. The tightest of these constraints comes from the *Planck* TT+lowP+lensing+BAO combination. The blue contours show the constraints in the base ΛCDM cosmology. The red contours are broader than the blue contours and there is greater overlap with the CFHTLenS contours, *but this offers only a marginal improvement compared to base* ΛCDM (compare with Fig. 18; see also the discussions in Leistedt et al. 2014 and Battye et al. 2015). For each of these models, the CFHTLenS results prefer

lower values of σ_8. Allowing for a higher neutrino mass lowers σ_8 from *Planck*, but does not help alleviate the discrepancy with the CFHTLenS data, since the *Planck* data prefer a lower value of H_0. A joint analysis of the CFHTLenS likelihood with *Planck* TT+lowP shows a $\Delta\chi^2 < 1$ preference for the extended neutrino models compared to base ΛCDM, and the fits to *Planck* TT+lowP are worse in all cases. In base ΛCDM the CFHTLenS data prefer a region of parameter space $\Delta\chi^2 \approx 4$ away from the *Planck* TT+lowP+CFHTLenS joint fit, indicative of the tension between the data sets. This is only slightly relieved to $\Delta\chi^2 \approx 3$ in the extended models.

In summary, modifications to the neutrino sector alone cannot easily explain the discrepancies between *Planck* and other astrophysical data described in Sect. 5.5, including the inference of a low value of σ_8 from rich cluster counts.

6.4.5. Testing perturbations in the neutrino background

As shown in the previous sections, the *Planck* data provide evidence for a cosmic neutrino background at a very high significance level. Neutrinos affect the CMB anisotropies at the background level, by changing the expansion rate before recombination and hence relevant quantities such as the sound horizon and the damping scales. Neutrinos also affect the CMB anisotropies via their perturbations. Perturbations in the neutrino background are coupled through gravity to the perturbations in the photon background, and can be described (for massless neutrinos) by the following set of equations (Hu 1998; Hu et al. 1999; Trotta & Melchiorri 2005; Archidiacono et al. 2011):

$$\dot{\delta}_\nu = \frac{\dot{a}}{a}\left(1-3c_{\rm eff}^2\right)\left(\delta_\nu + 3\frac{\dot{a}}{a}\frac{q_\nu}{k}\right) - k\left(q_\nu + \frac{2}{3k}\dot{h}\right), \quad (68a)$$

$$\dot{q}_\nu = k\,c_{\rm eff}^2\left(\delta_\nu + 3\frac{\dot{a}}{a}\frac{q_\nu}{k}\right) - \frac{\dot{a}}{a}q_\nu - \frac{2}{3}k\pi_\nu, \quad (68b)$$

$$\dot{\pi}_\nu = 3k\,c_{\rm vis}^2\left(\frac{2}{5}q_\nu + \frac{4}{15k}(\dot{h}+6\dot{\eta})\right) - \frac{3}{5}kF_{\nu,3}, \quad (68c)$$

$$\dot{F}_{\nu,\ell} = \frac{k}{2\ell+1}\left(\ell F_{\nu,\ell-1} - (\ell+1)F_{\nu,\ell+1}\right), \quad (\ell \geq 3). \quad (68d)$$

Here dots denote derivatives with respect to conformal time, δ_ν is the neutrino density contrast, q_ν is the neutrino velocity perturbation, π_ν the anisotropic stress, $F_{\nu,\ell}$ are higher-order moments of the neutrino distribution function, and h and η are the scalar metric perturbations in the synchronous gauge. In these equations, $c_{\rm eff}^2$ is the neutrino sound speed in its own reference frame and $c_{\rm vis}^2$ parameterizes the anisotropic stress. For standard non-interacting massless neutrinos $c_{\rm eff}^2 = c_{\rm vis}^2 = 1/3$. Any deviation from the expected values could provide a hint of non-standard physics in the neutrino sector.

A greater (lower) neutrino sound speed would increase (decrease) the neutrino pressure, leading to a lower (higher) perturbation amplitude. On the other hand, changing $c_{\rm vis}^2$ alters the viscosity of the neutrino fluid. For $c_{\rm vis}^2 = 0$, the neutrinos act as a perfect fluid, supporting undamped acoustic oscillations.

Several previous studies have used this approach to constrain $c_{\rm eff}^2$ and $c_{\rm vis}^2$ using cosmological data (see, e.g., Trotta & Melchiorri 2005; Smith et al. 2012; Archidiacono et al. 2013b; Gerbino et al. 2013; Audren et al. 2015), with the motivation that deviations from the expected values could be a hint of non-standard physics in the neutrino sector. Non-standard interactions could involve, for example, neutrino coupling with light scalar particles (Hannestad 2005; Beacom et al. 2004; Bell 2005; Sawyer 2006). If neutrinos are strongly coupled at recombination, this would result in a lower value for $c_{\rm vis}^2$ than in the standard model. Alternatively, the presence of early dark energy that mimics a relativistic component at recombination could possibly lead to a value for $c_{\rm eff}^2$ that differs from 1/3 (see, e.g., Calabrese et al. 2011).

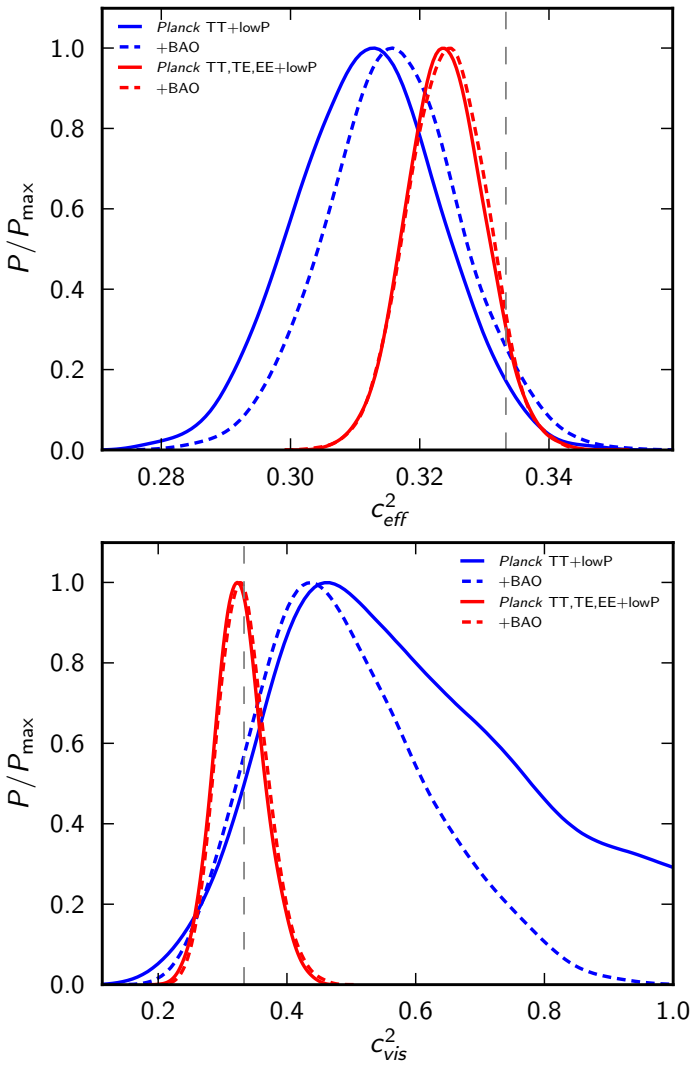

Fig. 34. 1D posterior distributions for the neutrino perturbation parameters $c_{\rm eff}^2$ (*top*) and $c_{\rm vis}^2$ (*bottom*). Dashed vertical lines indicate the conventional values $c_{\rm eff}^2 = c_{\rm vis}^2 = 1/3$.

In this analysis, for simplicity, we assume $N_{\rm eff} = 3.046$ and massless neutrinos. By using an equivalent parameterization for massive neutrinos (Audren et al. 2015) we have checked that assuming one massive neutrino with $\Sigma m_\nu \approx 0.06$ eV, as in the base model used throughout this paper, has no impact on the constraints on $c_{\rm eff}^2$ and $c_{\rm vis}^2$ reported in this section[29]. We adopt a flat prior between zero and unity for both $c_{\rm vis}^2$ and $c_{\rm eff}^2$.

The top and bottom panels of Fig. 34 show the posterior distributions of $c_{\rm eff}^2$ and $c_{\rm vis}^2$ from *Planck* TT+lowP, *Planck* TT+lowP+BAO, *Planck* TT,TE,EE+lowP, and *Planck* TT,TE,EE+lowP+BAO. The mean values and 68% errors on $c_{\rm eff}^2$

[29] We also do not explore extended cosmologies in this section, since no significant degeneracies are expected between ($\sum m_\nu$, $N_{\rm eff}$, w, $\mathrm{d}n_{\rm s}/\mathrm{d}\ln k$) and ($c_{\rm eff}^2$, $c_{\rm vis}^2$) (Audren et al. 2015).

and $c^2_{\rm vis}$ are

$$\left.\begin{aligned} c^2_{\rm eff} &= 0.312 \pm 0.011 \\ c^2_{\rm vis} &= 0.47^{+0.26}_{-0.12} \end{aligned}\right\} \textit{Planck}\ \text{TT+lowP}, \tag{69a}$$

$$\left.\begin{aligned} c^2_{\rm eff} &= 0.316 \pm 0.010 \\ c^2_{\rm vis} &= 0.44^{+0.15}_{-0.10} \end{aligned}\right\} \textit{Planck}\ \text{TT+lowP+BAO}, \tag{69b}$$

$$\left.\begin{aligned} c^2_{\rm eff} &= 0.3240 \pm 0.0060 \\ c^2_{\rm vis} &= 0.327 \pm 0.037 \end{aligned}\right\} \textit{Planck}\ \text{TT,TE,EE+lowP}, \tag{69c}$$

$$\left.\begin{aligned} c^2_{\rm eff} &= 0.3242 \pm 0.0059 \\ c^2_{\rm vis} &= 0.331 \pm 0.037 \end{aligned}\right\} \textit{Planck}\ \text{TT,TE,EE+lowP+BAO}. \tag{69d}$$

Constraints on these parameters are consistent with the conventional values $c^2_{\rm eff} = c^2_{\rm vis} = 1/3$. A vanishing value of $c^2_{\rm vis}$, which might imply a strong interaction between neutrinos and other species, is excluded at more than the 95% level arising from the *Planck* temperature data. This conclusion is greatly strengthened (to about 9σ) when *Planck* polarization data are included. As discussed in Bashinsky & Seljak (2004), neutrino anisotropic stresses introduce a phase shift in the CMB angular power spectra, which is more visible in polarization than temperature because of the sharper acoustic peaks. This explains why we see such a dramatic reduction in the error on $c^2_{\rm vis}$ when including polarization data.

The precision of our results is consistent with the forecasts discussed in Smith et al. (2012), and we find strong evidence, purely from CMB observations, for neutrino anisotropies with the standard values $c^2_{\rm vis} = 1/3$ and $c^2_{\rm eff} = 1/3$.

6.5. Primordial nucleosynthesis

6.5.1. Details of analysis approach

Standard big bang nucleosynthesis (BBN) predicts light element abundances as a function of parameters relevant to the CMB, such as the baryon-to-photon density ratio $\eta_{\rm b} \equiv n_{\rm b}/n_\gamma$, the radiation density parameterized by $N_{\rm eff}$, and the chemical potential of the electron neutrinos. In PCP13, we presented consistency checks between the *Planck* 2013 results, light element abundance data, and standard BBN. The goal of Sect. 6.5.2 below is to update these results and to provide improved tests of the standard BBN model. In Sect. 6.5.3 we show how *Planck* data can be used to constrain nuclear reaction rates, and in Sect. 6.5.4 we will present the most stringent CMB bounds to date on the primordial helium fraction.

For simplicity, our analysis assumes a negligible leptonic asymmetry in the electron neutrino sector. For a fixed photon temperature today (which we take to be $T_0 = 2.7255$ K), $\eta_{\rm b}$ can be related to $\omega_{\rm b} \equiv \Omega_{\rm b}h^2$, up to a small (and negligible) uncertainty associated with the primordial helium fraction. Standard BBN then predicts the abundance of each light element as a function of only two parameters, $\omega_{\rm b}$ and $\Delta N_{\rm eff} \equiv N_{\rm eff} - 3.046$, with a theoretical error coming mainly from uncertainties in the neutron lifetime and a few nuclear reaction rates.

We will confine our discussion to BBN predictions for the primordial abundances[30] of ^{4}He and deuterium, expressed, respectively as $Y^{\rm BBN}_{\rm P} = 4n_{\rm He}/n_{\rm b}$ and $y_{\rm DP} = 10^5 n_{\rm D}/n_{\rm H}$. We will not discuss other light elements, such as tritium and lithium, because the observed abundance measurements and their interpretation is more controversial (see Fields et al. 2014, for a recent review). As in PCP13, the BBN predictions for $Y^{\rm BBN}_{\rm P}(\omega_{\rm b}, \Delta N_{\rm eff})$ and $y_{\rm DP}(\omega_{\rm b}, \Delta N_{\rm eff})$ are given by Taylor expansions obtained with the `PArthENoPE` code (Pisanti et al. 2008), similar to the ones presented in Iocco et al. (2009), but updated by the `PArthENoPE` team with the latest observational data on nuclear rates and on the neutron life-time:

$$\begin{aligned} Y^{\rm BBN}_{\rm P} &= 0.2311 + 0.9502\omega_{\rm b} - 11.27\omega^2_{\rm b} \\ &\quad + \Delta N_{\rm eff}\left(0.01356 + 0.008581\omega_{\rm b} - 0.1810\omega^2_{\rm b}\right) \\ &\quad + \Delta N^2_{\rm eff}\left(-0.0009795 - 0.001370\omega_{\rm b} + 0.01746\omega^2_{\rm b}\right), \end{aligned} \tag{70}$$

$$\begin{aligned} y_{\rm DP} &= 18.754 - 1534.4\omega_{\rm b} + 48656\omega^2_{\rm b} - 552670\omega^3_{\rm b} \\ &\quad + \Delta N_{\rm eff}\left(2.4914 - 208.11\omega_{\rm b} + 6760.9\omega^2_{\rm b} - 78007\omega^3_{\rm b}\right) \\ &\quad + \Delta N^2_{\rm eff}\left(0.012907 - 1.3653\omega_{\rm b} + 37.388\omega^2_{\rm b} - 267.78\omega^3_{\rm b}\right). \end{aligned} \tag{71}$$

By averaging over several measurements, the Particle Data Group 2014 (Olive et al. 2014) estimates the neutron life-time to be $\tau_{\rm n} = (880.3 \pm 1.1)$ s at 68% CL[31]. The expansions in Eqs. (70) and (71) are based on this central value, and we assume that Eq. (70) predicts the correct helium fraction up to a standard error $\sigma(Y^{\rm BBN}_{\rm P}) = 0.0003$, obtained by propagating the error on $\tau_{\rm n}$.

The uncertainty on the deuterium fraction is dominated by that on the rate of the reaction $\mathrm{d(p,\gamma)^3He}$. For that rate, in PCP13 we relied on the result of Serpico et al. (2004), obtained by fitting several experiments. The expansions of Eqs. (70) and (71) now adopt the latest experimental determination by Adelberger et al. (2011) and use the best-fit expression in their Eq. (29). We also rely on the uncertainty quoted in Adelberger et al. (2011) and propagate it to the deuterium fraction. This gives a standard error $\sigma(y_{\rm DP}) = 0.06$, which is more conservative than the error adopted in PCP13.

6.5.2. Primordial abundances from *Planck* data and standard BBN

We first investigate the consistency of standard BBN and the CMB by fixing the radiation density to its standard value, i.e., $N_{\rm eff} = 3.046$, based on the assumption of standard neutrino decoupling and no extra light relics. We can then use *Planck* data to measure $\omega_{\rm b}$, assuming base ΛCDM, and test for consistency with experimental abundance measurements. The 95% CL bounds obtained for the base ΛCDM model for various data

[30] BBN calculations usually refer to nucleon number density fractions rather than mass fractions. To avoid any ambiguity with the helium mass fraction $Y_{\rm P}$, normally used in CMB physics, we use superscripts to distinguish between the two definitions $Y^{\rm CMB}_{\rm P}$ and $Y^{\rm BBN}_{\rm P}$. Typically, $Y^{\rm BBN}_{\rm P}$ is about 0.5% higher than $Y^{\rm CMB}_{\rm P}$.

[31] However, the most recent individual measurement by Yue et al. (2013) gives $\tau_{\rm n} = [887.8 \pm 1.2\ (\text{stat.}) \pm 1.9\ (\text{syst.})]$ s, which is discrepant at 3.3σ with the previous average (including only statistical errors). Hence one should bear in mind that systematic effects could be underestimated in the Particle Data Group result. Adopting the central value of Yue et al. (2013) would shift our results by a small amount (by a factor of 1.0062 for $Y_{\rm P}$ and 1.0036 for $y_{\rm DP}$).

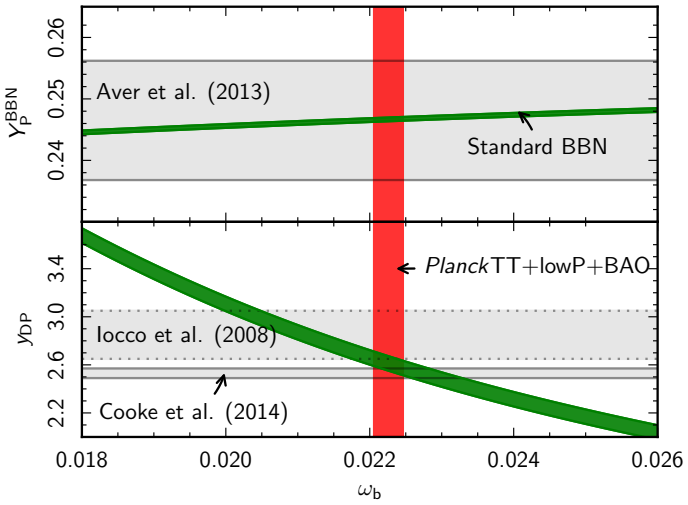

Fig. 35. Predictions of standard BBN for the primordial abundance of ^{4}He (*top*) and deuterium (*bottom*), as a function of the baryon density ω_b. The width of the green stripes corresponds to 68% uncertainties on nuclear reaction rates and on the neutron lifetime. The horizontal bands show observational bounds on primordial element abundances compiled by various authors, and the red vertical band shows the *Planck* TT+lowP+BAO bounds on ω_b (all with 68% errors). The BBN predictions and CMB results shown here assume $N_{\rm eff} = 3.046$ and no significant lepton asymmetry.

combinations are

$$\omega_b = \begin{cases} 0.02222^{+0.00045}_{-0.00043} & \textit{Planck}\ \text{TT+lowP}, \\ 0.02226^{+0.00040}_{-0.00039} & \textit{Planck}\ \text{TT+lowP+BAO}, \\ 0.02225^{+0.00032}_{-0.00030} & \textit{Planck}\ \text{TT,TE,EE+lowP}, \\ 0.02229^{+0.00029}_{-0.00027} & \textit{Planck}\ \text{TT,TE,EE+lowP+BAO}, \end{cases} \quad (72)$$

corresponding to a predicted primordial ^{4}He number density fraction (95% CL) of

$$Y_P^{BBN} = \begin{cases} 0.24665^{+(0.00020)\ 0.00063}_{-(0.00019)\ 0.00063} & \textit{Planck}\ \text{TT+lowP}, \\ 0.24667^{+(0.00018)\ 0.00063}_{-(0.00018)\ 0.00063} & \textit{Planck}\ \text{TT+lowP+BAO}, \\ 0.24667^{+(0.00014)\ 0.00062}_{-(0.00014)\ 0.00062} & \textit{Planck}\ \text{TT,TE,EE+lowP}, \\ 0.24668^{+(0.00013)\ 0.00061}_{-(0.00013)\ 0.00061} & \textit{Planck}\ \text{TT,TE,EE+lowP+BAO}, \end{cases} \quad (73)$$

and deuterium fraction (95% CL)

$$y_{DP} = \begin{cases} 2.620^{+(0.083)\ 0.15}_{-(0.085)\ 0.15} & \textit{Planck}\ \text{TT+lowP}, \\ 2.612^{+(0.075)\ 0.14}_{-(0.074)\ 0.14} & \textit{Planck}\ \text{TT+lowP+BAO}, \\ 2.614^{+(0.057)\ 0.13}_{-(0.060)\ 0.13} & \textit{Planck}\ \text{TT,TE,EE+lowP}, \\ 2.606^{+(0.051)\ 0.13}_{-(0.054)\ 0.13} & \textit{Planck}\ \text{TT,TE,EE+lowP+BAO}. \end{cases} \quad (74)$$

The first set of error bars (in parentheses) in Eqs. (73) and (74) reflect only the uncertainty on ω_b. The second set includes the theoretical uncertainty on the BBN predictions, added in quadrature to the errors from ω_b. The total errors in the predicted helium abundances are dominated by the BBN uncertainty, as in PCP13. For deuterium, the *Planck* 2015 results improve the determination of ω_b to the point where the theoretical errors are comparable or larger than the errors from the CMB. In other words, for base ΛCDM the predicted abundances cannot be improved substantially by further measurements of the CMB. This also means that *Planck* results can, in principle, be used to investigate nuclear reaction rates that dominate the theoretical uncertainty (see Sect. 6.5.3).

The results of Eqs. (73) and (74) are well within the ranges indicated by the latest measurements of primordial abundances, as illustrated in Fig. 35. The helium data compilation of Aver et al. (2013) gives $Y_P^{BBN} = 0.2465 \pm 0.0097$ (68% CL), and the *Planck* prediction is near the middle of this range[32]. As summarized by Aver et al. (2013) and Peimbert (2008), helium abundance measurements derived from emission lines in low-metallicity H II regions are notoriously difficult and prone to systematic errors. As a result, many discrepant helium abundance measurements can be found in the literature. Izotov et al. (2014) have reported $Y_P^{BBN} = 0.2551 \pm 0.0022$, which is discrepant with the base ΛCDM predictions by 3.4σ. Such a high helium fraction could be accommodated by increasing $N_{\rm eff}$ (see Fig. 36 and Sect. 6.5.4); however, at present it is not clear whether the error quoted by Izotov et al. (2014) accurately reflects systematic uncertainties, including in particular the error in extrapolating to zero metallicity.

Historically, deuterium abundance measurements have shown excess scatter over that expected from statistical errors, indicating the presence of systematic uncertainties in the observations. Figure 35 shows the data compilation of Iocco et al. (2009), $y_{DP} = 2.87 \pm 0.22$ (68% CL), which includes measurements based on damped Lyα and Lyman limit systems. We also show the more recent results by Cooke et al. (2014; see also Pettini & Cooke 2012) based on their observations of low-metallicity damped Lyα absorption systems in two quasars (SDSS J1358+6522, $z_{\rm abs} = 3.06726$ and SDSS J1419+0829, $z_{\rm abs} = 3.04973$) and a reanalysis of archival spectra of damped Lyα systems in three further quasars that satisfy strict selection criteria. The Cooke et al. (2014) analysis gives $y_{DP} = 2.53 \pm 0.04$ (68% CL), somewhat lower than the central Iocco et al. (2009) value, and with a much smaller error. The Cooke et al. (2014) value is almost certainly the more reliable measurement, as evidenced by the consistency of the deuterium abundances of the five systems in their analysis. The *Planck* base ΛCDM predictions of Eq. (74) lie within 1σ of the Cooke et al. (2014) result. This is a remarkable success for the standard theory of BBN.

It is worth noting that the *Planck* data are so accurate that ω_b is insensitive to the underlying cosmological model. In our grid of extensions to base ΛCDM the largest degradation of the error in ω_b is in models that allow $N_{\rm eff}$ to vary. In these models, the mean value of ω_b is almost identical to that for base ΛCDM, but the error on ω_b increases by about 30%. The value of ω_b is stable to even more radical changes to the cosmology, for example, adding general isocurvature modes (Planck Collaboration XX 2016).

If we relax the assumption that $N_{\rm eff} = 3.046$ (but adhere to the hypothesis that electron neutrinos have a standard distribution, with a negligible chemical potential), BBN predictions depend on both parameters (ω_b and $N_{\rm eff}$). Following the same methodology as in Sect. 6.4.4 of PCP13, we can identify the region of the ω_b–$N_{\rm eff}$ parameter space that is compatible with direct measurements of the primordial helium and deuterium

[32] A substantial part of this error comes from the regression to zero metallicity. The mean of the 17 measurements analysed by Aver et al. (2013) is $\langle Y_P^{BBN} \rangle = 0.2535 \pm 0.0036$, i.e., about 1.7σ higher than the *Planck* predictions of Eq. (73).

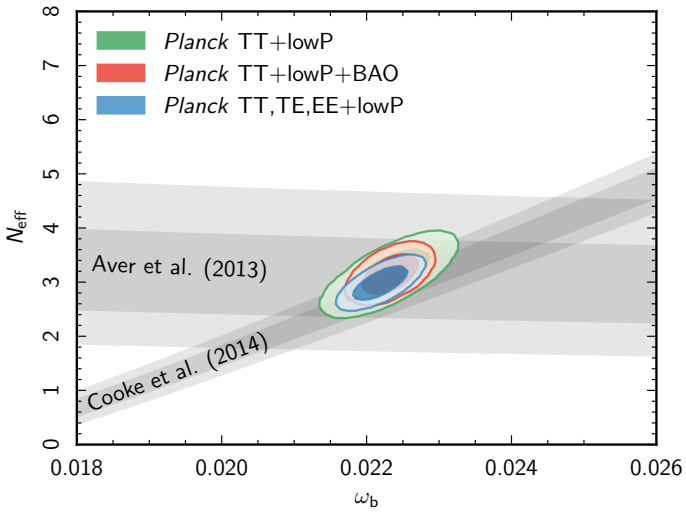

Fig. 36. Constraints in the $\omega_{\rm b}$–$N_{\rm eff}$ plane from *Planck* and *Planck*+BAO data (68% and 95% contours) compared to the predictions of BBN, given primordial element abundance measurements. We show the 68% and 95% confidence regions derived from ^{4}He bounds compiled by Aver et al. (2013) and from deuterium bounds compiled by Cooke et al. (2014). In the CMB analysis, $N_{\rm eff}$ is allowed to vary as an additional parameter to base ΛCDM, with $Y_{\rm P}$ fixed as a function of $\omega_{\rm b}$ and $N_{\rm eff}$, according to BBN predictions. These constraints assume no significant lepton asymmetry.

abundances, including the BBN theoretical errors. This is illustrated in Fig. 36 for the $N_{\rm eff}$ extension to base ΛCDM. The region preferred by CMB observations lies at the intersection between the helium and deuterium abundance 68% CL preferred regions and is compatible with the standard value of $N_{\rm eff} = 3.046$. This confirms the beautiful agreement between CMB and BBN physics. Figure 36 also shows that the *Planck* polarization data help in reducing the degeneracy between $\omega_{\rm b}$ and $N_{\rm eff}$.

We can actually make a more precise statement by combining the posterior distribution on $\omega_{\rm b}$ and $N_{\rm eff}$) obtained for *Planck* with that inferred from helium and deuterium abundance, including observational and theoretical errors. This provides joint CMB+BBN predictions on these parameters. After marginalizing over $\omega_{\rm b}$, the 95% CL preferred ranges for $N_{\rm eff}$ are

$$N_{\rm eff} = \begin{cases} 3.11^{+0.59}_{-0.57} & \text{He+}\textit{Planck}\text{ TT+lowP,} \\ 3.14^{+0.44}_{-0.43} & \text{He+}\textit{Planck}\text{ TT+lowP+BAO,} \\ 2.99^{+0.39}_{-0.39} & \text{He+}\textit{Planck}\text{ TT,TE,EE+lowP,} \end{cases} \quad (75)$$

when combining *Planck* with the helium abundance estimated by Aver et al. (2013), or

$$N_{\rm eff} = \begin{cases} 2.95^{+0.52}_{-0.52} & \text{D+}\textit{Planck}\text{ TT+lowP,} \\ 3.01^{+0.38}_{-0.37} & \text{D+}\textit{Planck}\text{ TT+lowP+BAO,} \\ 2.91^{+0.37}_{-0.37} & \text{D+}\textit{Planck}\text{ TT,TE,EE+lowP,} \end{cases} \quad (76)$$

when combining with the deuterium abundance measured by Cooke et al. (2014). These bounds represent the best currently-available estimates of $N_{\rm eff}$ and are remarkably consistent with the standard model prediction.

The allowed region in $\omega_{\rm b}$–$N_{\rm eff}$ space does not increase significantly when other parameters are allowed to vary at the same time. From our grid of extended models, we have checked that this conclusion holds in models with neutrino masses, tensor fluctuations, or running of the scalar spectral index, for example.

6.5.3. Constraints from *Planck* and deuterium observations on nuclear reaction rates

We have seen that primordial element abundances estimated from direct observations are consistent with those inferred from *Planck* data under the assumption of standard BBN. However, the *Planck* determination of $\omega_{\rm b}$ is so precise that the theoretical errors in the BBN predictions are now a dominant source of uncertainty. As noted by Cooke et al. (2014), one can begin to think about using CMB measurements together with accurate deuterium abundance measurements to learn about the underlying BBN physics.

While for helium the theoretical error comes mainly from the uncertainties in the neutron lifetime, for deuterium it is dominated by uncertainties in the radiative capture process d(p, γ)^{3}He, converting deuterium into helium. The present experimental uncertainty for the S-factor at low energy (relevant for BBN), is in the range 6–10% (Ma et al. 1997). However, as noted by several authors (see, e.g., Nollett & Holder 2011; Di Valentino et al. 2014) the best-fit value of $S(E)$ inferred from experimental data in the range $30\,{\rm keV} \leq E \leq 300\,{\rm keV}$ is about 5–10% lower than theoretical expectations (Viviani et al. 2000; Marcucci et al. 2005). The `PArthENoPE` BBN code assumes the lower experimental value for d(p, γ)^{3}He, and this might explain why the deuterium abundance determined by Cooke et al. (2014) is slightly lower than the value inferred by *Planck*.

To investigate this further, following the methodology of Di Valentino et al. (2014), we perform a combined analysis of *Planck* and deuterium observations, to constrain the value of the d(p, γ)^{3}He reaction rate. As in Di Valentino et al. (2014), we parameterize the thermal rate $R_2(T)$ of the d(p, γ)^{3}He process in the `PArthENoPE` code by introducing a rescaling factor A_2 of the experimental rate $R_2^{\rm ex}(T)$, i.e., $R_2(T) = A_2\, R_2^{\rm ex}(T)$, and solve for A_2 using various *Planck*+BAO data combinations, given the Cooke et al. (2014) deuterium abundance measurements.

Assuming the base ΛCDM model we find (68% CL)

$$A_2 = 1.106 \pm 0.071 \quad \textit{Planck}\text{ TT+lowP}, \quad (77a)$$
$$A_2 = 1.098 \pm 0.067 \quad \textit{Planck}\text{ TT+lowP+BAO}, \quad (77b)$$
$$A_2 = 1.110 \pm 0.062 \quad \textit{Planck}\text{ TT, TE, EE+lowP}, \quad (77c)$$
$$A_2 = 1.109 \pm 0.058 \quad \textit{Planck}\text{ TT, TE, EE+lowP+BAO}. \quad (77d)$$

The posteriors for A_2 are shown in Fig. 37. These results suggest that the d(p, γ)^{3}He reaction rate may be have been underestimated by about 10%. Evidently, tests of the standard BBN picture appear to have reached the point where they are limited by uncertainties in nuclear reaction rates. There is therefore a strong case to improve the precision of experimental measurements (e.g., Anders et al. 2014) and theoretical computations of key nuclear reaction rates relevant for BBN.

6.5.4. Model-independent bounds on the helium fraction from *Planck*

Instead of inferring the primordial helium abundance from BBN codes using ($\omega_{\rm b}$, $N_{\rm eff}$) constraints from *Planck*, we can measure it directly, since variations in $Y_{\rm P}^{\rm BBN}$ modify the density of free electrons between helium and hydrogen recombination and therefore affect the damping tail of the CMB anisotropies.

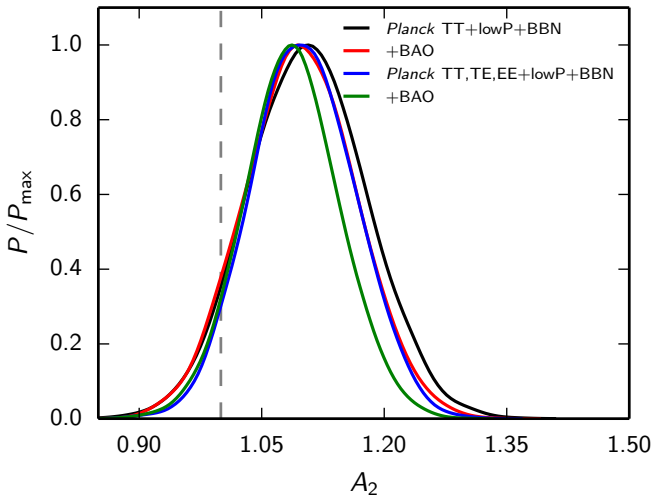

Fig. 37. Posteriors for the A_2 reaction rate parameter for various data combinations. The vertical dashed line shows the value $A_2 = 1$ that corresponds to the current experimental estimate of the $\mathrm{d(p,\gamma)^3He}$ rate used in the `PArthENoPE` BBN code.

If we allow $Y_{\rm P}^{\rm CMB}$ to vary as an additional parameter to base ΛCDM, we find the following constraints (at 95% CL):

$$Y_{\rm P}^{\rm BBN} = \begin{cases} 0.253^{+0.041}_{-0.042} & \textit{Planck}\ \text{TT+lowP}, \\ 0.255^{+0.036}_{-0.038} & \textit{Planck}\ \text{TT+lowP+BAO}, \\ 0.251^{+0.026}_{-0.027} & \textit{Planck}\ \text{TT,TE,EE+lowP}, \\ 0.253^{+0.025}_{-0.026} & \textit{Planck}\ \text{TT,TE,EE+lowP+BAO}. \end{cases} \quad (78)$$

Joint constraints on $Y_{\rm P}^{\rm BBN}$ and $\omega_{\rm b}$ are shown in Fig. 38. The addition of *Planck* polarization measurements results in a substantial reduction in the uncertainty on the helium fraction. In fact, the standard deviation on $Y_{\rm P}^{\rm BBN}$ in the case of *Planck* TT,TE,EE+lowP is only 30% larger than the observational error quoted by Aver et al. (2013). As emphasized throughout this paper, the systematic effects in the *Planck* polarization spectra, although at low levels, have not been accurately characterized at this time. Readers should therefore treat the polarization constraints with some caution. Nevertheless, as shown in Fig. 38, all three data combinations agree well with the observed helium abundance measurements and with the predictions of standard BBN.

There is a well-known parameter degeneracy between $Y_{\rm P}$ and the radiation density (see the discussion in PCP13). Helium abundance predictions from the CMB are therefore particularly sensitive to the addition of the parameter $N_{\rm eff}$ to base ΛCDM. Allowing both $Y_{\rm P}^{\rm BBN}$ and $N_{\rm eff}$ to vary we find the following constraints (at 95% CL):

$$Y_{\rm P}^{\rm BBN} = \begin{cases} 0.252^{+0.058}_{-0.065} & \textit{Planck}\ \text{TT+lowP}, \\ 0.251^{+0.058}_{-0.064} & \textit{Planck}\ \text{TT+lowP+BAO}, \\ 0.263^{+0.034}_{-0.037} & \textit{Planck}\ \text{TT,TE,EE+lowP}, \\ 0.262^{+0.035}_{-0.037} & \textit{Planck}\ \text{TT,TE,EE+lowP+BAO}. \end{cases} \quad (79)$$

Contours in the $Y_{\rm P}^{\rm BBN}$–$N_{\rm eff}$ plane are shown in Fig. 39. Here again, the impact of *Planck* polarization data is important, and helps to substantially reduce the degeneracy between these two

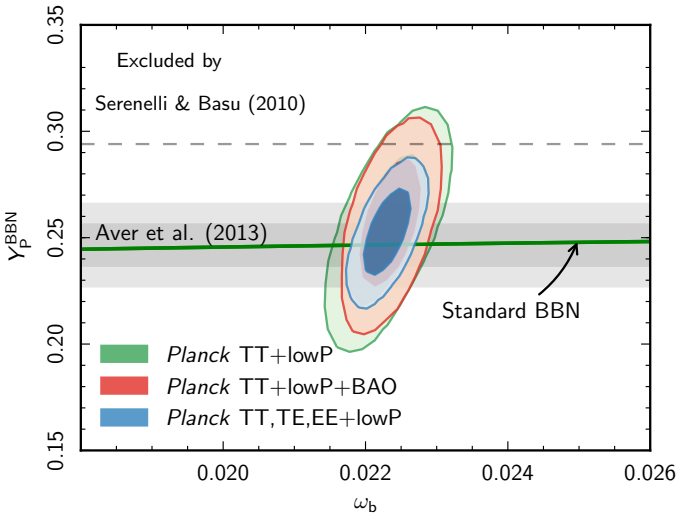

Fig. 38. Constraints in the $\omega_{\rm b}$–$Y_{\rm P}^{\rm BBN}$ plane from *Planck* and *Planck*+BAO, compared to helium abundance measurements. Here 68% and 95% contours are plotted for the CMB(+BAO) data combinations when $Y_{\rm P}^{\rm BBN}$ is allowed to vary as an additional parameter to base ΛCDM. The horizontal band shows observational bounds on ^{4}He compiled by Aver et al. (2013) with 68% and 95% errors, while the dashed line at the top of the figure delineates the conservative 95% upper bound inferred from the Solar helium abundance by Serenelli & Basu (2010). The green stripe shows the predictions of standard BBN for the primordial abundance of ^{4}He as a function of the baryon density. Both BBN predictions and CMB results assume $N_{\rm eff} = 3.046$ and no significant lepton asymmetry.

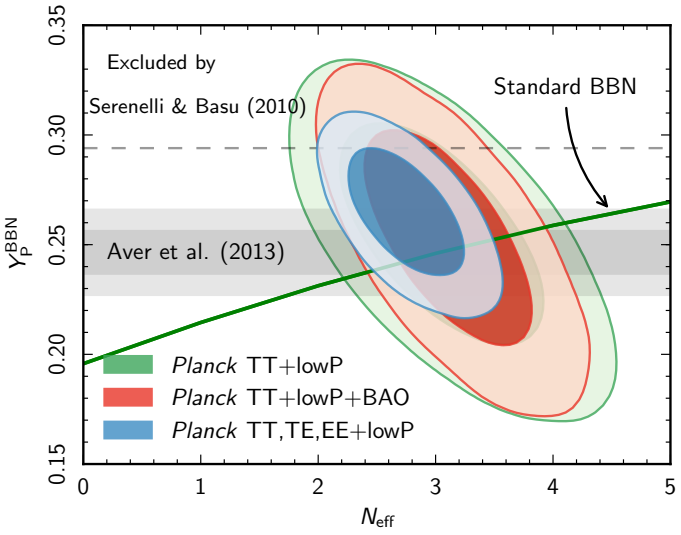

Fig. 39. As in Fig. 38, but now allowing $Y_{\rm P}^{\rm BBN}$ and $N_{\rm eff}$ to vary as parameter extensions to base ΛCDM.

parameters. The *Planck* TT,TE,EE+lowP contours are in very good agreement with standard BBN and $N_{\rm eff} = 3.046$. However, even if we relax the assumption of standard BBN, the CMB does not allow high values of $N_{\rm eff}$. It is therefore difficult to accommodate an extra thermalized relativistic species, even if the standard BBN prior on the helium fraction is relaxed.

6.6. Dark matter annihilation

Energy injection from dark matter (DM) annihilation can alter the recombination history, leading to changes in the

temperature and polarization power spectra of the CMB (e.g., Chen & Kamionkowski 2004; Padmanabhan & Finkbeiner 2005). As demonstrated in several papers (e.g., Galli et al. 2009a; Slatyer et al. 2009; Finkbeiner et al. 2012), CMB anisotropies offer an opportunity to constrain the nature of DM. Furthermore, CMB experiments such as *Planck* can achieve limits on the annihilation cross-section that are relevant for the interpretation of the rise in the cosmic-ray positron fraction at energies $\gtrsim$10 GeV observed by PAMELA, *Fermi*, and AMS (Adriani et al. 2009; Ackermann et al. 2012; Aguilar et al. 2014). The CMB constraints are complementary to those determined from other astrophysical probes, such as the γ-ray observations of dwarf galaxies by the *Fermi* satellite (Ackermann et al. 2014).

The way in which DM annihilations heat and ionize the gaseous background depends on the nature of the cascade of particles produced following annihilation and, in particular, on the production of $e^{\pm}$ pairs and photons that couple to the gas. The fraction of the rest mass energy that is injected into the gas can be modelled by an "efficiency factor", $f(z)$, which is typically in the range 0.01−1 and depends on redshift[33]. Computations of $f(z)$ for various annihilation channels can be found in Slatyer et al. (2009), Hütsi et al. (2009), and Evoli et al. (2013). The rate of energy release per unit volume by annihilating DM can therefore be written as

$$\frac{\mathrm{d}E}{\mathrm{d}t\mathrm{d}V}(z) = 2\,g\,\rho_{\rm crit}^2 c^2 \Omega_{\rm c}^2 (1+z)^6 p_{\rm ann}(z), \tag{80}$$

where $p_{\rm ann}$ is defined as

$$p_{\rm ann}(z) \equiv f(z)\frac{\langle\sigma v\rangle}{m_\chi}. \tag{81}$$

Here $\rho_{\rm crit}$ the critical density of the Universe today, m_χ is the mass of the DM particle, and $\langle\sigma v\rangle$ is the thermally-averaged annihilation cross-section times the velocity (explicitly the so-called Mller velocity); we will refer to this quantity loosely as the "cross-section" hereafter. In Eq. (80), g is a degeneracy factor that is equal to 1/2 for Majorana particles and 1/4 for Dirac particles. In this paper, the constraints will refer to Majorana particles. Note that to produce the observed dark matter density from thermal DM relics requires an annihilation cross-section of $\langle\sigma v\rangle \approx 3\times10^{-26}\,\mathrm{cm^3\,s^{-1}}$ (assuming s-wave annihilation) at the time of freeze-out (see, e.g., the review by Profumo 2013).

Both the amplitude and redshift dependence of the efficiency factor $f(z)$ depend on the details of the annihilation process (e.g., Slatyer et al. 2009). The functional shape of $f(z)$ can be taken into account using generalized parameterizations or principal components (Finkbeiner et al. 2012; Hutsi et al. 2011), similar to the analysis of the recombination history presented in Sect. 6.7.4. However, as shown in Galli et al. (2011), Giesen et al. (2012), and Finkbeiner et al. (2012), to a first approximation the redshift dependence of $f(z)$ can be ignored, since current CMB data (including *Planck*) are sensitive to energy injection over a relatively narrow range of redshift, typically $z \approx 1000$–600. The effects of DM annihilation can therefore be reasonably well parameterized by a single constant parameter, $p_{\rm ann}$ (with $f(z)$ set to a constant $f_{\rm eff}$), which encodes the dependence on the properties of the DM particles. In the following, we calculate constraints on the $p_{\rm ann}$ parameter, assuming that it is constant, and then project these constraints on to a particular dark matter model assuming $f_{\rm eff} \equiv f(z = 600)$, since the effect of dark matter annihilation peaks at $z \approx 600$ (see Finkbeiner et al. 2012). The $f(z)$ functions used here are those calculated in Slatyer et al. (2009), with the updates described in Galli et al. (2013) and Madhavacheril et al. (2014). Finally, we estimate the fractions of injected energy that affect the gaseous background, from heating, ionizations, or Lyα excitations, using the updated calculations described in Galli et al. (2013) and Valdes et al. (2010), following Shull & van Steenberg (1985).

We compute the theoretical angular power spectrum in the presence of DM annihilations by modifying the `recfast` routine (Seager et al. 1999) in the `camb` code as in Galli et al. (2011)[34]. We then add $p_{\rm ann}$ as an additional parameter to those of the base ΛCDM cosmology. Table 6 shows the constraints for various data combinations.

The constraints on $p_{\rm ann}$ from the *Planck* TT+lowP spectra are about 3 times weaker than the 95% limit of $p_{\rm ann} < 2.1\times10^{-27}\,\mathrm{cm^3\,s^{-1}\,GeV^{-1}}$ derived from WMAP9, which includes WMAP polarization data at low multipoles. On the other hand, the *Planck* TE or EE spectra improve the constraints on $p_{\rm ann}$ by about an order of magnitude compared to those from *Planck* TT alone. This is because the main effect of dark matter annihilation is to increase the width of last scattering, leading to a suppression of the amplitude of the peaks, both in

Table 6. Constraints on $p_{\rm ann}$ in units of $\mathrm{cm^3\,s^{-1}\,GeV^{-1}}$.

Data combinations	$p_{\rm ann}$ (95% upper limits)
TT+lowP	$<.7\times10^{-27}$
EE+lowP	$<1.4\times10^{-27}$
TE+lowP	$<5.9\times10^{-28}$
TT+lowP+lensing	$<4.4\times10^{-27}$
TT,TE,EE+lowP	$<4.1\times10^{-28}$
TT,TE,EE+lowP+lensing	$<3.4\times10^{-28}$
TT,TE,EE+lowP+ext	$<3.5\times10^{-28}$

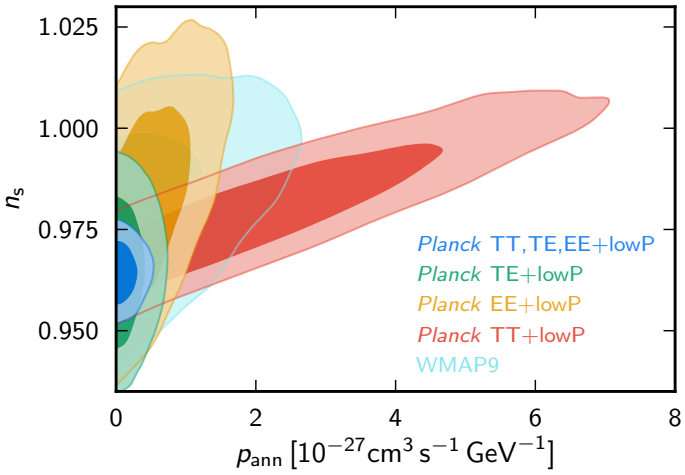

Fig. 40. 2D marginal distributions in the $p_{\rm ann}$–$n_{\rm s}$ plane for *Planck* TT+lowP (red), *Planck* EE+lowP (yellow), *Planck* TE+lowP (green), and *Planck* TT,TE,EE+lowP (blue) data combinations. We also show the constraints obtained using WMAP9 data (light blue).

[33] To maintain consistency with other papers on dark matter annihilation, we retain the notation $f(z)$ for the efficiency factor in this section; it should not be confused with the growth rate factor introduced in Eq. (32).

[34] We checked that we obtain similar results using either the `HyRec` code (Ali-Haimoud & Hirata 2011), as detailed in Giesen et al. (2012), or `CosmoRec` (Chluba & Thomas 2011), instead of `recfast`.

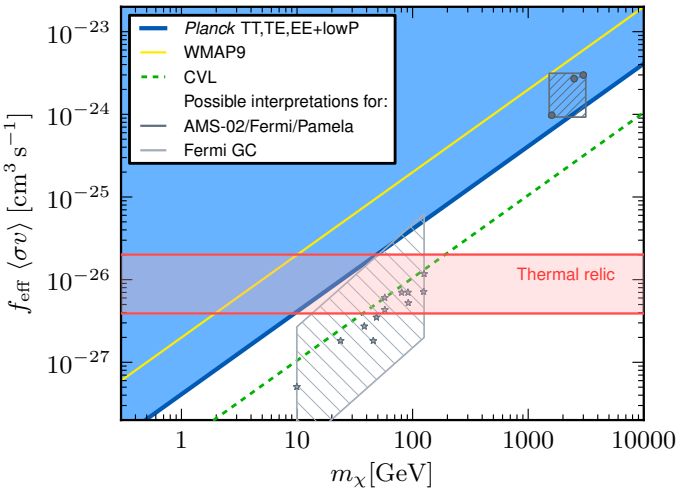

Fig. 41. Constraints on the self-annihilation cross-section at recombination, $\langle\sigma v\rangle_{z_*}$, times the efficiency parameter, $f_{\rm eff}$ (Eq. (81)). The blue area shows the parameter space excluded by the *Planck* TT, TE, EE+lowP data at 95% CL. The yellow line indicates the constraint using WMAP9 data. The dashed green line delineates the region ultimately accessible to a cosmic-variance-limited experiment with angular resolution comparable to that of *Planck*. The horizontal red band includes the values of the thermal-relic cross-section multiplied by the appropriate $f_{\rm eff}$ for different DM annihilation channels. The dark grey circles show the best-fit DM models for the PAMELA/AMS-02/*Fermi* cosmic-ray excesses, as calculated in Cholis & Hooper (2013, caption of their figure 6). The light grey stars show the best-fit DM models for the *Fermi* Galactic centre γ-ray excess, as calculated by Calore et al. (2015, their tables I, II, and III), with the light grey area indicating the astrophysical uncertainties on the best-fit cross-sections.

temperature and polarization. As a result, the effects of DM annihilation on the power spectra at high multipole are degenerate with other parameters of base ΛCDM, such as $n_{\rm s}$ and $A_{\rm s}$ (Chen & Kamionkowski 2004; Padmanabhan & Finkbeiner 2005). At large angular scales ($\ell \lesssim 200$), however, dark matter annihilation can produce an enhancement in polarization, caused by the increased ionization fraction in the freeze-out tail following recombination. As a result, large-angle polarization information is crucial for breaking the degeneracies between parameters, as illustrated in Fig. 40. The strongest constraints on $p_{\rm ann}$ therefore come from the full *Planck* temperature and polarization likelihood and there is little improvement if other astrophysical data, or *Planck* lensing, are added[35].

We verified the robustness of the *Planck* TT,TE,EE+lowP constraint by also allowing other parameter extensions of base ΛCDM ($N_{\rm eff}$, ${\rm d}n_{\rm s}/{\rm d}\ln k$, or $Y_{\rm P}$) to vary together with $p_{\rm ann}$. We found that the constraint is weakened by up to 20%. Furthermore, we have verified that we obtain consistent results when relaxing the priors on the amplitudes of the Galactic dust templates or if we use the `CamSpec` likelihood instead of the baseline `Plik` likelihood.

Figure 41 shows the constraints from WMAP9, *Planck* TT,TE,EE+lowP, and a forecast for a cosmic-variance-limited experiment with similar angular resolution to *Planck*[36]. The horizontal red band includes the values of the thermal-relic cross-section multiplied by the appropriate $f_{\rm eff}$ for different DM annihilation channels. For example, the upper red line corresponds to $f_{\rm eff} = 0.67$, which is appropriate for a DM particle of mass $m_\chi = 10\,{\rm GeV}$ annihilating into e^+e^-, while the lower red line corresponds to $f_{\rm eff} = 0.13$, for a DM particle annihilating into $2\pi^+\pi^-$ through an intermediate mediator (see, e.g., Arkani-Hamed et al. 2009). The *Planck* data exclude at 95% confidence level a thermal relic cross-section for DM particles of mass $m_\chi \lesssim 44\,{\rm Gev}$ annihilating into e^+e^- ($f_{\rm eff} \approx 0.6$), $m_\chi \lesssim 16\,{\rm GeV}$ annihilating into $\mu^+\mu^-$ or $b\bar{b}$ ($f_{\rm eff} \approx 0.2$), and $m_\chi \lesssim 11\,{\rm GeV}$ annihilating into $\tau^+\tau^-$ ($f_{\rm eff} \approx 0.15$).

The dark grey shaded area in Fig. 41 shows the approximate allowed region of parameter space, as calculated by Cholis & Hooper (2013) on the assumption that the PAMELA, AMS, and *Fermi* cosmic-ray excesses are caused by DM annihilation; the dark grey dots indicate the best-fit dark matter models described in that paper (for a recent discussion on best-fitting models, see also Boudaud et al. 2015). The favoured value of the cross-section is about two orders of magnitude higher than the thermal relic cross-section ($\approx 3\times10^{-26}\,{\rm cm}^3\,{\rm s}^{-1}$). Attempts to reconcile such a high cross-section with the relic abundance of DM include a Sommerfeld enhanced cross-section (that may saturate at $\langle\sigma v\rangle \approx 10^{-24}\,{\rm cm}^3\,{\rm s}^{-1}$) or non-thermal production of DM (see, e.g., the discussion by Madhavacheril et al. 2014). Both of these possibilities are strongly disfavoured by the *Planck* data. We cannot, however, exclude more exotic possibilities, such as DM annihilation through a p-wave channel with a cross-section that scales as v^2 (Diamanti et al. 2014). Since the relative velocity of DM particles at recombination is many orders of magnitude smaller than in the Galactic halo, such a model cannot be constrained using CMB data.

Observations from the *Fermi* Large Area Telescope of extended γ-ray emission towards the centre of the Milky Way, peaking at energies of around 1−3 GeV, have been interpreted as evidence for annihilating DM (e.g.,Goodenough & Hooper 2009; Gordon & Macías 2013; Daylan et al.2016; Abazajian et al. 2014; Lacroix et al. 2014). The light grey stars in Fig. 41 show specific models of DM annihilation designed to fit the *Fermi* γ-ray excess (Calore et al. 2015), while the light grey box shows the uncertainties of the best-fit cross-sections due to imprecise knowledge of the Galactic DM halo profile. Although the interpretation of the *Fermi* excess remains controversial (because of uncertainties in the astrophysical backgrounds), DM annihilation remains a possible explanation. The best-fit models of Calore et al. (2015) are consistent with the *Planck* constraints on DM annihilation.

6.7. Testing recombination physics with Planck

The cosmological recombination process determines how CMB photons decoupled from baryons around redshift $z \approx 10^3$, when the Universe was about 400 000 years old. The importance of this transition on the CMB anisotropies has long been recognized (Sunyaev & Zeldovich 1970; Peebles & Yu 1970). The most advanced computations of the ionization history (e.g., Ali-Haïmoud & Hirata 2010; Ali-Haimoud & Hirata 2011; Chluba & Thomas 2011; Chluba et al. 2012) account for many subtle atomic physics and radiative transfer effects that were not included in the earliest calculations (Zeldovich et al. 1968; Peebles 1968).

With precision data from *Planck*, we are sensitive to sub-percent variations of the free electron fraction

[35] It is interesting to note that the constraint derived from *Planck* TT,TE,EE+lowP is consistent with the forecast given in Galli et al. (2009a), $p_{\rm ann} < 3\times10^{-28}\,{\rm cm}^3\,{\rm s}^{-1}\,{\rm GeV}^{-1}$.

[36] We assumed here that the cosmic-variance-limited experiment would measure the angular power spectra up to a maximum multipole of $\ell_{\rm max} = 2500$, observing a sky fraction $f_{\rm sky} = 0.65$.

around last-scattering (e.g., Hu et al. 1995; Seager et al. 2000; Seljak et al. 2003). Quantifying the impact of uncertainties in the ionization history around the maximum of the Thomson visibility function on predictions of the CMB power spectra is thus crucial for the scientific interpretation of data from *Planck*. In particular, for tests of models of inflation and extensions to ΛCDM, the interpretation of the CMB data can be significantly compromised by inaccuracies in the recombination calculation (e.g., Wong et al. 2008; Rubiño-Martín et al. 2010; Shaw & Chluba 2011). This problem can be approached in two ways, either by using modified recombination models with a specific physical process (or parameter) in mind, or in a semi-blind, model-independent way. Both approaches provide useful insights in assessing the robustness of the results from *Planck*.

Model-dependent limits on varying fundamental constants (Kaplinghat et al. 1999; Scóccola et al. 2009; Galli et al. 2009b), annihilating or decaying particles (e.g., Chen & Kamionkowski 2004; Padmanabhan & Finkbeiner 2005; Zhang et al. 2006, and Sect. 6.6), or more general sources of extra ionization and excitation photons (Peebles et al. 2000; Doroshkevich et al. 2003; Galli et al. 2008), have been discussed extensively in the literature.

As already discussed in PCP13, the choice for *Planck* has been to use the rapid calculations of the `recfast` code, modified using corrections calculated with the more precise codes. To start this sub-section we quantify the effect on the analysis of *Planck* data of the remaining uncertainties in the standard recombination history obtained with different recombination codes (Sect. 6.7.1). We also derive CMB anisotropy-based measurements of the hydrogen 2s−1s two-photon decay rate, $A_{2s\rightarrow1s}$ (Sect. 6.7.2), and the average CMB temperature, T_0 derived at the last-scattering epoch (Sect. 6.7.3). These two parameters strongly affect the recombination history but are usually kept fixed when fitting models to CMB data (as in the analyses described in previous sections). Section 6.7.4 describes model-independent constraints on perturbed recombination scenarios. A discussion of these cases provides both a test of the consistency of the CMB data with the standard recombination scenario and also a demonstration of the impressive sensitivity of *Planck* to small variations in the ionization history at $z \approx 1100$.

6.7.1. Comparison of different recombination codes

Even for pre-*Planck* data, it was realized that the early recombination calculations of Zeldovich et al. (1968) and Peebles (1968) had to be improved. This led to the development of the widely-used and computationally quick `recfast` code (Seager et al. 1999, 2000). However, for *Planck*, the recombination model of `recfast` in its original form is not accurate enough. Percent-level corrections, due to detailed radiative transfer and atomic physics effects have to be taken into account. Ignoring these effects can bias the inferred cosmological parameters, some by as much as a few standard deviations.

The recombination problem was solved as a common effort of several groups (Dubrovich & Grachev 2005; Kholupenko et al. 2007; Chluba & Sunyaev 2006b; Rubiño-Martín et al. 2006; Karshenboim & Ivanov 2008; Wong & Scott 2007; Switzer & Hirata 2008; Grin & Hirata 2010; Ali-Haïmoud & Hirata 2010). This work was undertaken, to a large extent, in preparation for the precision data from *Planck*. Both `CosmoRec` (Chluba & Thomas 2011) and `HyRec` (Ali-Haimoud & Hirata 2011) allow fast and precise computations of the ionization history, explicitly capturing the physics of the recombination problem. For the standard cosmology, the ionization histories obtained from these two codes in their default settings agree to within 0.05% for hydrogen recombination ($600 \lesssim z \lesssim 1600$) and 0.35% during helium recombination[37] ($1600 \lesssim z \lesssim 3000$). The effect of these small differences on the CMB power spectra is $\lesssim 0.1\%$ at $\ell < 4000$ and so has a negligible impact on the interpretation of precision CMB data; for the standard six parameters of base ΛCDM, we find that the largest effect is a bias in $\ln(10^{10}A_s)$ at the level of $0.04\sigma \approx 0.0012$ for *Planck* TT,TE,EE+lowP+BAO.

For *Planck* analyses, the recombination model of `recfast` is used by default. In `recfast`, the precise dynamics of recombination is not modelled physically, but approximated with fitting-functions calibrated against the full recombination calculations assuming a reference cosmology (Seager et al. 1999, 2000; Wong et al. 2008). At the level of precision required for *Planck*, the `recfast` approach is sufficiently accurate, provided that the cosmologies are close to base ΛCDM (Rubiño-Martín et al. 2010; Shaw & Chluba 2011). Comparing the latest version of `recfast` (`camb` version) with `CosmoRec`, we find agreement to within 0.2% for hydrogen recombination ($600 \lesssim z \lesssim 1600$) and 0.2% during helium recombination for the standard ionization history. The effect on the CMB power spectra is $\lesssim$0.15% at $\ell < 4000$, although with slightly more pronounced shifts in the peak positions than when comparing `CosmoRec` and `HyRec`. For the base ΛCDM model, we find that the largest bias is on n_s, at the level of 0.15σ (≈0.0006) for *Planck* TT,TE,EE+lowP+BAO. Although this is about 5 times larger than the difference in n_s between `CosmoRec` and `HyRec`, this bias is nevertheless unimportant at the current level of precision (and smaller than the differences seen from different likelihoods, see Sect. 3.1).

Finally we compare `CosmoRec` with `recfast` in its original form (i.e., before recalibrating the fitting-functions on refined recombination calculations). For base ΛCDM, we expect to see biases of $\Delta\Omega_b h^2 \approx -2.1\sigma \approx -0.00028$ and $\Delta n_s \approx -3.3\sigma \approx -0.012$ (Shaw & Chluba 2011). Using the actual data (*Planck* TT,TE,EE+lowP+BAO) we find biases of $\Delta\Omega_b h^2 \approx -1.8\sigma \approx -0.00024$ and $\Delta n_s \approx -2.6\sigma \approx -0.010$, very close to the expected values. This illustrates explicitly the importance of the improvements of `CosmoRec` and `HyRec` over the original version of `recfast` for the interpretation of *Planck* data. However, `CosmoRec` and `HyRec` themselves are much more computationally intensive than the modified `recfast`, which is why we use `recfast` in most *Planck* cosmological analyses.

6.7.2. Measuring $A_{2s\rightarrow1s}$ with *Planck*

The crucial role of the 2s−1s two-photon decay channel for the dynamics of hydrogen recombination has been appreciated since the early days of CMB research (Zeldovich et al. 1968; Peebles 1968). Recombination is an out-of-equilibrium process and energetic photons emitted in the far Wien tail of the CMB by Lyman continuum and series transitions keep the primordial plasma ionized for a much longer period than expected from simple equilibrium recombination physics. Direct recombinations to the ground state of hydrogen are prohibited, causing a modification of the free electron number density, N_e, by only $\Delta N_e/N_e \approx 10^{-6}$ around $z \approx 10^3$ (Chluba & Sunyaev 2007). Similarly, the slow escape of photons from the Lyα resonance reduces the effective Ly-α transition rate to $A^*_{2p\rightarrow1s} \approx 1-10\,\mathrm{s}^{-1}$ (by more than seven orders of magnitude), making it comparable to the vacuum

[37] Helium recombination is treated in more detail by `CosmoRec` (e.g., Rubiño-Martín et al. 2008; Chluba et al. 2012), which explains most of the difference.

2s−1s two-photon decay rate of $A_{2s\to1s} \approx 8.22\,s^{-1}$. About 57% of all hydrogen atoms in the Universe became neutral through the 2s−1s channel (e.g., Wong et al. 2006; Chluba & Sunyaev 2006a), and subtle effects, such as the induced 2s−1s two-photon decay and Lyα re-absorption, need to be considered in precision recombination calculations (Chluba & Sunyaev 2006b; Kholupenko & Ivanchik 2006; Hirata 2008).

The high sensitivity of the recombination process to the 2s−1s two-photon transition rate also implies that instead of simply adopting a value for $A_{2s\to1s}$ from theoretical computations (Breit & Teller 1940; Spitzer & Greenstein 1951; Goldman 1989) one can directly determine it with CMB data. From the theoretical point of view it would be surprising to find a value that deviates significantly from $A_{2s\to1s} = 8.2206\,s^{-1}$, derived from the most detailed computation (Labzowsky et al. 2005). However, laboratory measurements of this transition rate are extremely challenging (O'Connell et al. 1975; Krüger & Oed 1975; Cesar et al. 1996). The most stringent limit is for the differential decay rate, $A_{2s\to1s}(\lambda)\,d\lambda = (1.5 \pm 0.65)\,s^{-1}$ (a 43% error) at wavelengths $\lambda = 255.4$−232.0 nm, consistent with the theoretical value of $A_{2s\to1s}(\lambda)\,d\lambda = 1.02\,s^{-1}$ in the same wavelength range (Krüger & Oed 1975). With precision data from *Planck* we are in a position to perform the best measurement to date, using cosmological data to inform us about atomic transition rates at last scattering (as also emphasized by Mukhanov et al. 2012).

The 2s−1s two-photon rate affects the CMB anisotropies only through its effect on the recombination history. A larger value of $A_{2s\to1s}$, accelerates recombination, allowing photons and baryons to decouple earlier, an effect that shifts the acoustic peaks towards smaller scales. In addition, slightly less damping occurs, as in the case of the stimulated 2s−1s two-photon decays (Chluba & Sunyaev 2006b). This implies that for flat cosmologies, variations of $A_{2s\to1s}$ correlate with $\Omega_c h^2$ and H_0 (which affect the distance to the last scattering surface), while $A_{2s\to1s}$ anti-correlates with $\Omega_b h^2$ and n_s (which modify the slope of the damping tail). Despite these degeneracies, one expects that *Planck* will provide a measurement of $A_{2s\to1s}$ to within $\pm0.5\,s^{-1}$, corresponding to an approximately 6% uncertainty (Mukhanov et al. 2012).

In Fig. 42, we show the marginalized posterior for $A_{2s\to1s}$ from *Planck* and for *Planck* combined with BAO. Using `CosmoRec` to compute the recombination history, we find

$$A_{2s\to1s} = 7.70 \pm 1.01\,s^{-1} \quad \textit{Planck}\ \text{TT+lowP}, \tag{82a}$$
$$A_{2s\to1s} = 7.72 \pm 0.60\,s^{-1} \quad \textit{Planck}\ \text{TT, TE, EE+lowP}, \tag{82b}$$
$$A_{2s\to1s} = 7.71 \pm 0.99\,s^{-1} \quad \textit{Planck}\ \text{TT+lowP+BAO}, \tag{82c}$$
$$A_{2s\to1s} = 7.75 \pm 0.61\,s^{-1} \quad \textit{Planck}\ \text{TT, TE, EE+lowP+BAO}. \tag{82d}$$

These results are in very good agreement with the theoretical value, $A_{2s\to1s} = 8.2206\,s^{-1}$. For *Planck* TT,TE,EE+lowP+BAO, approximately 8% precision is reached using cosmological data. These constraints are not sensitive to the addition of BAO, or other external data (JLA+H_0). The slight shift away from the theoretical value is accompanied by small (fractions of a σ) shifts in n_s, $\Omega_c h^2$, and H_0, to compensate for the effects of $A_{2s\to1s}$ on the distance to the last scattering surface and damping tail. This indicates that additional constraints on the acoustic scale are required to fully break degeneracies between these parameters and their effects on the CMB power spectrum, a task that could be achieved in the future using large-scale structure surveys and next generation CMB experiments.

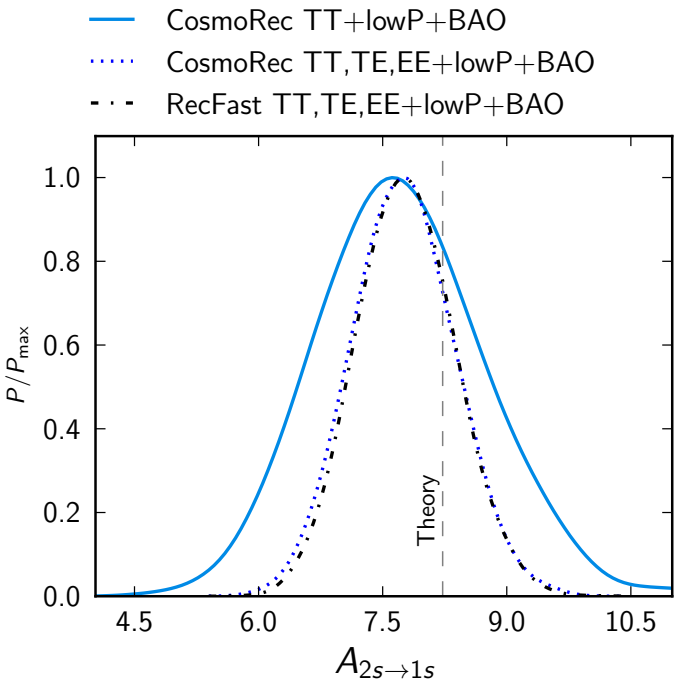

Fig. 42. Marginalized posterior for $A_{2s\to1s}$, obtained using `CosmoRec`, with and without small-scale polarization data. We find good agreement with the theoretical value of $A_{2s\to1s} = 8.2206\,s^{-1}$. For comparison, we also show the result for *Planck* TT,TE,EE+lowP+BAO obtained with `recfast`, emphasizing the consistency of different treatments.

The values for $A_{2s\to1s}$ quoted above were obtained using `CosmoRec`. When varying $A_{2s\to1s}$, the range of cosmologies becomes large enough to potentially introduce a mismatch of the `recfast` fitting-functions that could affect the posterior. In particular, with `recfast` the 2s−1s two-photon and Lyα channels are not treated separately, so that changes specific to the 2s−1s decay channel propagate inconsistently[38]. However, repeating the analysis with `recfast`, we find $A_{2s\to1s} = 7.78 \pm 0.58\,s^{-1}$ (see Fig. 42), for *Planck* TT,TE,EE+lowP+BAO, which is in excellent agreement with `CosmoRec`, showing that these effects can be neglected.

6.7.3. Measuring T_0 at last-scattering with *Planck*

Our best constraint on the CMB monopole temperature comes from the measurements of the CMB spectrum with COBE/FIRAS, giving a 0.02% determination of T_0 (Fixsen et al. 1996; Fixsen 2009). Other constraints from molecular lines typically reach 1% precision (see Table 2 in Fixsen 2009, for an overview), while independent BBN constraints provide 5−10% limits (Simha & Steigman 2008; Jeong et al. 2014).

The CMB anisotropies provide additional ways of determining the value of T_0 (for fixed values of $N_{\rm eff}$ and Y_P). One is through the energy distribution of the CMB anisotropies (Fixsen et al. 1996; Fixsen 2003; Chluba 2014) and another through their power spectra (Opher & Pelinson 2004, 2005; Chluba 2014). Even small changes in T_0, compatible with the COBE/FIRAS error, affect the ionization history at the 0.5% level around last-scattering, propagating to a roughly 0.1%

[38] One effect is that by increasing $A_{2s\to1s}$ fewer Lyα photons are produced. This reduces the Lyα feedback correction to the 2s−1s channel, which further accelerates recombination, an effect that is not captured with `recfast` in the current implementation.

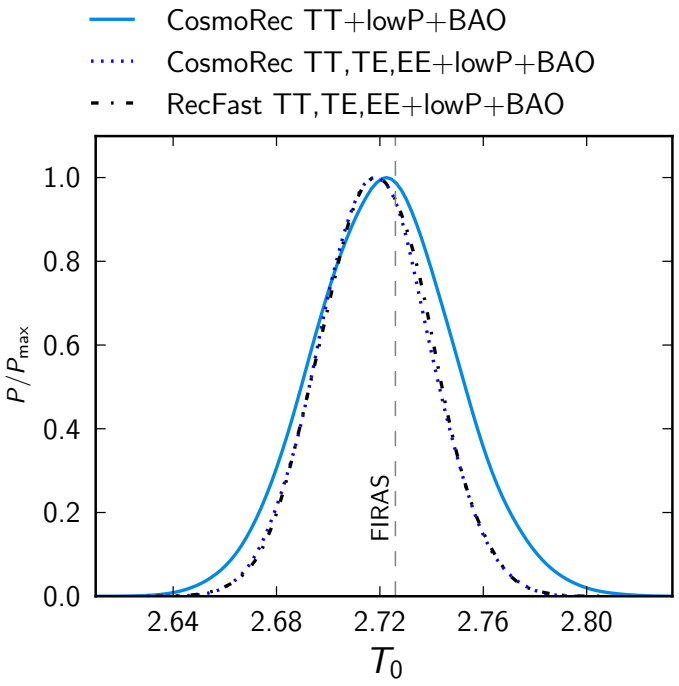

Fig. 43. Marginalized posterior for T_0. We find excellent agreement with the COBE/FIRAS measurement. For comparison, we show the result for *Planck* TT,TE,EE+lowP+BAO obtained using both `CosmoRec` and `recfast`, emphasizing the consistency of different treatments.

uncertainty in the CMB power spectrum (Chluba & Sunyaev 2008). Overall, the effect of this uncertainty on the parameters of ΛCDM models is small (Hamann & Wong 2008); however, without prior knowledge of T_0 from the COBE/FIRAS measurement, the situation would change significantly.

The CMB monopole affects the CMB anisotropies in several ways. Most importantly, for larger T_0, photons decouple from baryons at lower redshift, since more ionizing photons are present in the Wien-tail of the CMB. This effect is amplified because of the exponential dependence of the atomic level populations on the ratio of the ionization potentials and CMB temperature. In addition, increasing T_0 lowers the expansion timescale of the Universe and the redshift of matter-radiation equality, while increasing the photon sound speed. Some of these effects are also produced by varying $N_{\rm eff}$; however, the effects of T_0 on the ionization history and photon sound speed are distinct.

With CMB data alone, the determination of T_0 is degenerate with other parameters, but the addition of other data sets breaks this degeneracy. Marginalized posterior distributions for T_0 are shown in Fig. 43. Using `CosmoRec`, we find

$$T_0 = 2.722 \pm 0.027\,{\rm K} \quad \textit{Planck}\ {\rm TT{+}lowP{+}BAO}, \tag{83a}$$
$$T_0 = 2.718 \pm 0.021\,{\rm K} \quad \textit{Planck}\ {\rm TT, TE, EE{+}lowP{+}BAO}, \tag{83b}$$

and similar results are obtained with `recfast`. This is in excellent agreement with the COBE/FIRAS measurement, $T_0 = 2.7255 \pm 0.0006$ K (Fixsen et al. 1996; Fixsen 2009). These measurements of T_0 reach a precision that is comparable to the accuracy obtained with interstellar molecules. Since the systematics of these independent methods are very different, this result demonstrates the consistency of all these data. Allowing T_0 to vary causes the errors of the other cosmological parameters to increase. The strongest effect is on $\theta_{\rm MC}$, which is highly degenerate with T_0. The error on $\theta_{\rm MC}$ increases by a factor of roughly 25 if T_0 is allowed to vary. The error on $\Omega_{\rm b}h^2$ increases by a factor of about 4, while the errors on $n_{\rm s}$ and $\Omega_{\rm c}h^2$ increase by factors of 1.5−2, and the other cosmological parameters are largely unaffected by variations in T_0. Because of the strong degeneracy with $\theta_{\rm MC}$, no constraint on T_0 can be obtained using *Planck* data alone. External data, such as BAO, are therefore required to break this geometric degeneracy.

It is important to emphasize that the CMB measures the temperature at a redshift of $z \approx 1100$, so the comparison with measurements of T_0 at the present day is effectively a test of the constancy of $aT_{\rm CMB}$, where $a \approx 1/1100$ is the scale-factor at the time of last-scattering. It is remarkable that we are able to test the constancy of $aT_{\rm CMB} \equiv T_0$ over such a large dynamic range in redshift. Of course, if we did find that $aT_{\rm CMB}$ around recombination were discrepant with T_0 now, then we would need to invent a finely-tuned late-time photon injection mechanism[39] to explain the anomaly. Fortunately, the data are consistent with the standard $T_{\rm CMB} \propto (1+z)$ scaling of the CMB temperature.

Another approach to measuring $aT_{\rm CMB}$ is through the thermal Sunyaev-Zeldovich effect in rich clusters of galaxies at various redshifts (Fabbri et al. 1978; Rephaeli 1980), although it is unclear how one would interpret a failure of this test without an explicit model. In practice this approach is consistent with a scaling $aT_{\rm CMB} =$ constant, but with lower precision than obtained here from *Planck* (e.g., Battistelli et al. 2002; Luzzi et al. 2009; Saro et al. 2014; Hurier et al. 2014). A simple $T_{\rm CMB} = T_0(1+z)^{1-\beta}$ modification to the standard temperature redshift relation is frequently discussed in the literature (though this case is not justified by any physical model and is difficult to realize without creating a CMB spectral distortion, see Chluba 2014). For this parameterization we find

$$\beta = (0.2 \pm 1.4) \times 10^{-3} \quad \textit{Planck}\ {\rm TT{+}lowP{+}BAO}, \tag{84a}$$
$$\beta = (0.4 \pm 1.1) \times 10^{-3} \quad \textit{Planck}\ {\rm TT, TE, EE{+}lowP{+}BAO}, \tag{84b}$$

where we have adopted a recombination redshift of $z_* = 1100$[40]. Because of the long lever-arm in redshift afforded by the CMB, this is an improvement over earlier constraints by more than an order of magnitude (e.g., Hurier et al. 2014).

In a self-consistent picture, changes of T_0 would also affect the BBN era. We might therefore consider a simultaneous variation of $N_{\rm eff}$ and $Y_{\rm P}$ to reflect the variation of the neutrino energy density accompanying a putative variation in the photon energy density. Since we find $aT_{\rm CMB}$ at recombination to be highly consistent with the observed CMB temperature from COBE/FIRAS, considering this extra variation seems unnecessary. Instead, we may view the $aT_{\rm CMB}$ variation investigated here as further support for the limits discussed in Sects. 6.4 and 6.5.

6.7.4. Semi-blind perturbed recombination analysis

The high sensitivity of small-scale CMB anisotropies to the ionization history of the Universe around the epoch of recombination allows us to constrain possible deviations from the standard recombination scenario in a model-independent way (Farhang et al. 2012, 2013). The method relies on an eigenanalysis (often referred to as a principle component analysis) of perturbations in the free electron fraction, $X_{\rm e}(z) = N_{\rm e}/N_{\rm H}$, where $N_{\rm H}$ denotes the number density of hydrogen nuclei. The eigenmodes selected are specific to the data used in the analysis.

[39] Pure energy release in the form of heating of ordinary matter would leave a Compton y-distortion (Zeldovich & Sunyaev 1969) at these late times (Burigana et al. 1991; Hu & Silk 1993; Chluba & Sunyaev 2012).
[40] The test depends on the logarithm of the redshift and so is insensitive to the precise value adopted for z_*.

Table 7. Standard parameters and the first three X_e-modes, as determined for *Planck* TT,TE,EE+lowP+BAO.

Parameter	+ 1 mode	+ 2 modes	+ 3 modes
$\Omega_b h^2$ . . .	0.02229 ± 0.00017	0.02237 ± 0.00018	0.02237 ± 0.00019
$\Omega_c h^2$ . . .	0.1190 ± 0.0010	0.1186 ± 0.0011	0.1187 ± 0.0012
H_0	67.64 ± 0.48	67.80 ± 0.51	67.80 ± 0.56
τ	0.065 ± 0.012	0.068 ± 0.013	0.068 ± 0.013
n_s	0.9667 ± 0.0053	0.9677 ± 0.0055	0.9678 ± 0.0067
$\ln(10^{10} A_s)$	3.062 ± 0.023	3.066 ± 0.024	3.066 ± 0.024
μ_1	-0.03 ± 0.12	0.03 ± 0.14	0.02 ± 0.15
μ_2	. . .	-0.17 ± 0.18	-0.18 ± 0.19
μ_3	. . .	. . .	-0.02 ± 0.88

Similar approaches have been used to constrain deviations of the reionization history from the simplest models (Mortonson & Hu 2008) and annihilating dark matter scenarios (Finkbeiner et al. 2012), both with the prior assumption that the standard recombination physics is fully understood, as well as for constraining trajectories in inflation Planck Collaboration XX (2016) and dark energy Planck Collaboration XIV (2016) parameterizations.

Here, we use *Planck* data to find preferred ionization fraction trajectories $X_e(z)$ composed of low-order perturbation eigenmodes to the standard history (X_e-modes). The X_e-modes are constructed through the eigen-decomposition of the inverse of the Fisher information matrix for base ΛCDM (the six cosmological parameters and the nuisance parameters) and recombination perturbation parameters (see Farhang et al. 2012, for details). This procedure allows us to estimate the errors on the eigenmode amplitudes, μ_i, providing a rank ordering of the X_e-modes and their information content.

The first three X_e-modes for *Planck* TT,TE,EE+lowP are illustrated in Fig. 44, together with their impact on the differential visibility function. Figure 45 shows the response of the CMB temperature and polarization power spectra to these eigenmodes. The first mode mainly leads to a change in the width and height of the Thomson visibility function (bottom panel of Fig. 44). This implies less diffusion damping, which is also reflected in the modifications to the CMB power spectra (as shown in Fig. 45). The second mode causes the visibility maximum to shift towards higher redshifts for $\mu_2 > 0$, which leads to a shift of the CMB extrema to smaller scales; however, for roughly constant width of the visibility function it also introduces less damping at small scales. The third mode causes a combination of changes in both the position and width of the visibility function, with a pronounced effect on the location of the acoustic peaks. For the analysis of *Planck* data combinations, we only use X_e-modes that are optimized for *Planck* TT,TE,EE+lowP.

We modified `CosmoMC` to estimate the mode amplitudes. The results for *Planck* TT,TE,EE+lowP+BAO are presented in Table 7. Although all mode amplitudes are consistent with standard recombination, adding the second X_e-mode causes mild shifts in H_0 and τ. For *Planck* TT+lowP, we find $\mu_1 = -0.11 \pm 0.51$ and $\mu_2 = -0.23 \pm 0.50$, using the *Planck* TT,TE,EE+lowP eigenmodes, again consistent with the standard recombination scenario. Adding the polarization data improves the errors by more than a factor of 2. However, the mode amplitudes are insensitive to the addition of external data.

With pre-*Planck* data, only the amplitude, μ_1, of the first eigenmode could be constrained. The corresponding change in the ionization history translates mainly into a change in the slope of the CMB damping tail, with this mode resembling the first mode determined using *Planck* data (Fig. 44).

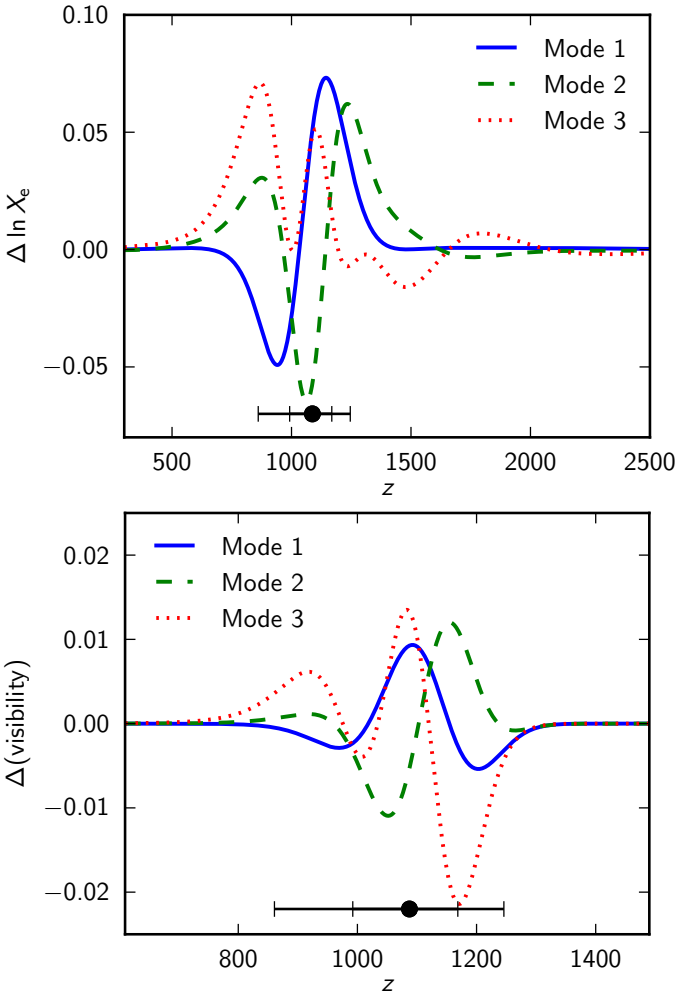

Fig. 44. Eigen-modes of the recombination history, marginalized over the standard six cosmological and *Planck* nuisance parameters. The *upper panel* shows the first three X_e-modes constructed for *Planck* TT,TE,EE+lowP data. The *lower panel* show changes in the differential visibility corresponding to 1σ deviations from the standard recombination scenario for the first three X_e-modes. The maximum of the Thomson visibility function and width are indicated in both figures.

The WMAP9+SPT data gave a non-zero value for the first eigenmode at about 2σ, $\mu_1^{\rm SPT} = -0.80 \pm 0.37$. However, the WMAP9+ACT data gave $\mu_1^{\rm ACT} = 0.14 \pm 0.45$ and the combined pre-*Planck* data (WMAP+ACT+SPT) gave $\mu_1^{\rm pre} = -0.44 \pm 0.33$, both consistent with the standard recombination scenario (Calabrese et al. 2013). The variation among these results is another manifestation of the tensions between different pre-*Planck* CMB data, as discussed in PCP13.

Although not optimal for *Planck* data, we also compute the amplitudes of the first three X_e-modes constructed for the WMAP9+SPT data set. This provides a more direct comparison with the pre-*Planck* constraints. For *Planck* TT,TE,EE+lowP+BAO we obtain $\mu_1^{\rm SPT} = -0.10 \pm 0.13$ and $\mu_2^{\rm SPT} = -0.13 \pm 0.18$. The mild tension of the pre-*Planck* data with the standard recombination scenario disappears when using *Planck* data. This is especially impressive, since the errors have improved by more than a factor of 2. By projecting onto the *Planck* modes, we find that the first two SPT modes can be expressed as $\mu_1^{\rm SPT} \approx 0.69\mu_1 + 0.66\mu_2 \approx -0.09$ and $\mu_2^{\rm SPT} \approx -0.70\mu_1 + 0.64\mu_2 \approx -0.13$, which emphasizes the consistency of the results. Adding the first three SPT modes,

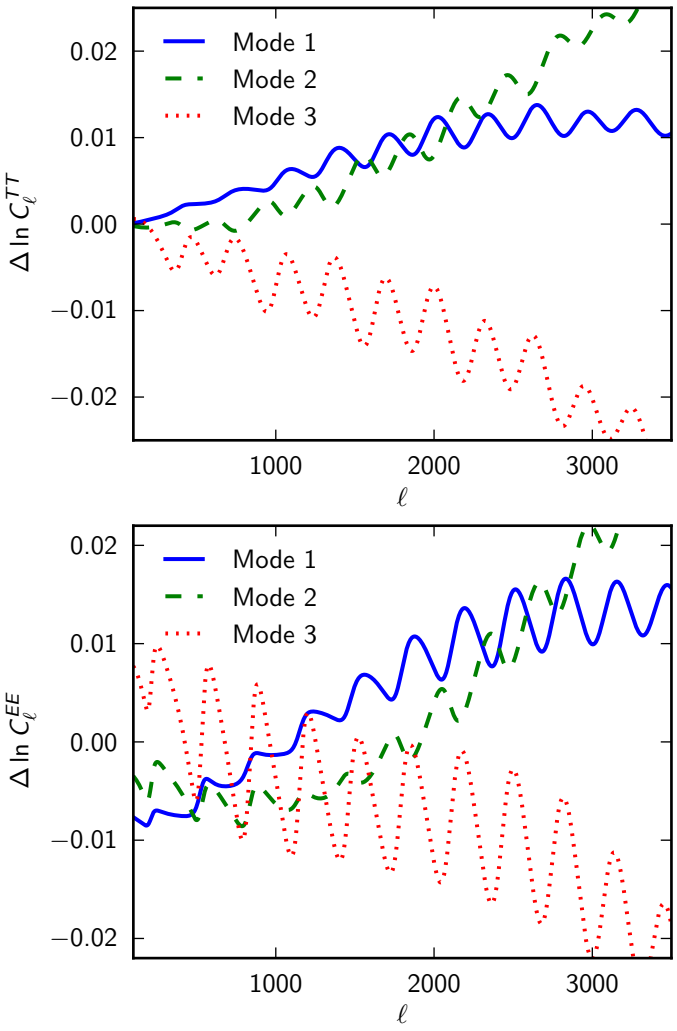

Fig. 45. Changes in the TT (*upper panel*) and EE (*lower panel*) power spectra caused by a 1σ deviation from the standard recombination scenario for the first three X_e-modes (see Fig. 44).

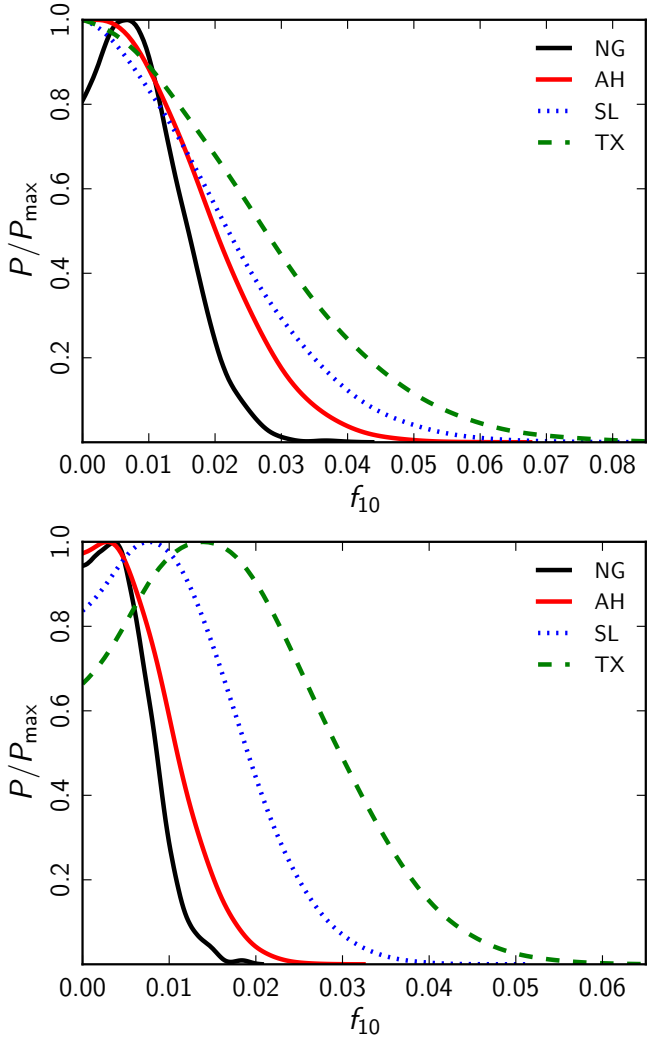

Fig. 46. Marginalized posterior distributions for the fractional contribution, f_{10}, of the defect contribution to the temperature power spectrum at $\ell = 10$ (see the text for the precise definition). Here we show the constraints for the Nambu-Goto cosmic strings (NG, solid black), field-theory simulations of Abelian-Higgs cosmic strings (AH, solid red), semi-local strings (SL, dotted blue), and global textures (TX, dashed green). The *upper panel* shows the 1D posterior for the *Planck*+lowP data, while constraints shown in the *lower panel* additionally use the TE and EE data.

we obtain $\mu_1^{\rm SPT} = -0.09 \pm 0.13$, $\mu_2^{\rm SPT} = -0.14 \pm 0.21$, and $\mu_3^{\rm SPT} = -0.12 \pm 0.86$, which again is consistent with the standard model of recombination. The small changes in the mode amplitudes when adding the third mode arise because the SPT modes are not optimal for *Planck* and so are correlated.

6.8. Cosmic defects

Topological defects are a generic by-product of symmetry-breaking phase transitions and a common phenomenon in condensed matter systems. Cosmic defects of various types can be formed in phase transitions in the early Universe (Kibble 1976). In particular, cosmic strings can be produced in some supersymmetric and grand-unified theories at the end of inflation (Jeannerot et al. 2003), as well as in higher-dimensional theories (e.g., Polchinski 2005). Constraints on the abundance of cosmic strings and other defects therefore place limits on a range of models of the early Universe. More discussion on the formation, evolution, and cosmological role of topological defects can be found, for example, in the reviews by Vilenkin & Shellard (2000), Hindmarsh & Kibble (1995), and Copeland & Kibble (2010).

In this section we revisit the power spectrum-based constraints on the abundance of cosmic strings and other topological defects using the 2015 *Planck* data, including *Planck* polarization measurements. The general approach follows that described in the *Planck* 2013 analysis of cosmic defects (Planck Collaboration XXV 2014), so here we focus on the updated constraints rather than on details of the methodology.

Topological defects are non-perturbative excitations of the underlying field theory and their study requires numerical simulations. Unfortunately, since the Hubble scale, c/H_0, is over 50 orders of magnitude greater that the thickness of a GUT-scale string, approximately $(\hbar/\mu c)^{1/2}$ with μ the mass per unit length of the string, it is impractical to simulate the string dynamics exactly in the late Universe. For this reason one needs to make approximations. One approach considers the limit of an infinitely thin string, which corresponds to using the Nambu-Goto ("NG") action for the string dynamics. In an alternative approach, the actual field dynamics for a given model are solved on a lattice.

Table 8. 95% upper limits on the parameter f_{10} and on the derived parameter $G\mu/c^2$ for the defect models discussed in the text.

	TT+lowP		TT,TE,EE+lowP	
Defect type	f_{10}	$G\mu/c^2$	f_{10}	$G\mu/c^2$
NG	<0.020	$< 1.8 \times 10^{-7}$	<0.011	$<1.3 \times 10^{-7}$
AH	<0.030	$< 3.3 \times 10^{-7}$	<0.015	$<2.4 \times 10^{-7}$
SL	<0.039	$<10.6 \times 10^{-7}$	<0.024	$<8.5 \times 10^{-7}$
TX	<0.047	$< 9.8 \times 10^{-7}$	<0.036	$<8.6 \times 10^{-7}$

Notes. We show results for *Planck* TT+lowP data as well as for *Planck* TT, TE, EE+lowP.

In this case it is necessary to resolve the string core, which generally requires more computationally intensive simulations than in the NG approach. Lattice simulations, however, can include additional physics, such as field radiation that is not present in NG simulations. Here we will use field-theory simulations of the Abelian-Higgs action ("AH"); details of these simulations are discussed in Bevis et al. (2007, 2010).

The field-theory approach also allows one to simulate theories in which the defects are not cosmic strings and so cannot be described by the NG action. Examples include semi-local strings ("SL", Urrestilla et al. 2008) and global defects. Here we will specifically consider the breaking of a global $O(4)$ symmetry resulting in texture defects ("TX").

For the field-theory defects, we measure the energy-momentum tensor from the simulations and insert it as an additional constituent into a modified version of the CMBEASY Boltzmann code (Doran 2005) to predict the defect contribution to the CMB temperature and polarization power spectra (see, e.g., Durrer et al. 2002). The same approach can be applied to NG strings, but rather than using simulations directly, we model the strings using the unconnected segment model ("USM", Albrecht et al. 1999; Pogosian & Vachaspati 1999). In this model, strings are represented by a set of uncorrelated straight segments, with scaling properties chosen to match those determined from numerical simulations. In this case, the string energy-momentum tensor can be computed analytically and used as an active source in a modified Boltzmann code. For this analysis we use CMBACT version 4 [41], whereas Planck Collaboration XXV (2014) used version 3. There have been several improvements to the code since the 2013 analysis, including a correction to the normalization of vector mode spectra. However, the largest change comes from an improved treatment of the scaling properties. The string correlation length and velocity are described by an updated velocity-dependent one-scale model (Martins & Shellard 2002), which provides better agreement with numerical simulations. Small-scale structure of the string, which was previously a free parameter, is accounted for by the one-scale model.

The CMB power spectra from defects are proportional to $(G\mu/c^2)^2$. We scale the computed template CMB spectra, and add these to the inflationary and foreground power spectra, to form the theory spectra that enter the likelihood. In practice, we parameterize the defects with their relative contribution to the TT spectrum at multipole $\ell = 10$, $f_{10} \equiv C_{10}^{TT(\mathrm{defect})}/C_{10}^{TT(\mathrm{total})}$. We vary f_{10} and the standard six parameters of the base ΛCDM model, using CosmoMC. We also report our results in terms of the derived parameter $G\mu/c^2$.

[41] http://www.sfu.ca/~levon/cmbact.html

The constraints on f_{10} and the inferred limits on $G\mu/c^2$ are summarized in Table 8. The marginalized 1D posterior distribution functions are shown in Fig. 46. For *Planck* TT+lowP we find that the results are similar to the *Planck*+WP constraints reported in Planck Collaboration XXV (2014), for the AH model, or somewhat better for SL and TX. However, the addition of the *Planck* high-ℓ TE and EE polarization data leads to a significant improvement compared to the 2013 constraints.

For the NG string model, the results based on *Planck* TT+lowP are slightly weaker than the 2013 *Planck*+WP constraints. This is caused by a difference in the updated defect spectrum from the USM model, which has a less pronounced peak and shifts towards the AH spectrum. With the inclusion of polarization, *Planck* TT,TE,EE+lowP improves the upper limit on f_{10} by a factor of 2, as for the AH model. The differences between the AH and NG results quoted here can be regarded as a rough indication of the uncertainty in the theoretical string power spectra.

In summary, we find no evidence for cosmic defects from the *Planck* 2015 data, with tighter limits than before.

7. Conclusions[42]

(1) The six-parameter base ΛCDM model continues to provide a very good match to the more extensive 2015 *Planck* data, including polarization. This is the most important conclusion of this paper.

(2) The 2015 *Planck* TT, TE, EE, and lensing spectra are consistent with each other under the assumption of the base ΛCDM cosmology. However, when comparing the TE and EE spectra computed for different frequency combinations, we find evidence for systematic effects caused by temperature-to-polarization leakage. These effects are at low levels and have little impact on the science conclusions of this paper.

(3) We have presented the first results on polarization from the LFI at low multipoles. The LFI polarization data, together with *Planck* lensing and high-multipole temperature data, gives a reionization optical depth of $\tau = 0.066 \pm 0.016$ and a reionization redshift of $z_{\mathrm{re}} = 8.8^{+1.7}_{-1.4}$. These numbers are in good agreement with those inferred from the WMAP9 polarization data cleaned for polarized dust emission using HFI 353-GHz maps. They are also in good agreement with results from *Planck* temperature and lensing data, i.e., excluding any information from polarization at low multipoles.

(4) The absolute calibration of the *Planck* 2015 HFI spectra is higher by 2% (in power) compared to 2013, largely resolving the calibration difference noted in PCP13 between WMAP and *Planck*. In addition, there have been a number of small changes to the low-level *Planck* processing and more accurate calibrations of the HFI beams. The 2015 *Planck* likelihood also makes more aggressive use of sky than in PCP13 and incorporates some refinements to the modelling of unresolved foregrounds. Apart from differences in τ (caused by switching to the LFI low-multipole polarization likelihood, as described in item 3 above) and the amplitude-τ combination $A_{\mathrm{s}}e^{-2\tau}$ (caused by the change in absolute calibration), the 2015 parameters for base ΛCDM are in good agreement with those reported in PCP13.

(5) The *Planck* TT, TE, and EE spectra are accurately described by a purely adiabatic spectrum of fluctuations with

[42] As in the abstract, here we quote 68% confidence limits on measured parameters and 95% upper limits on other parameters.

a spectral tilt $n_s = 0.968 \pm 0.006$, consistent with the predictions of single-field inflationary models. Combining *Planck* data with BAO, we find tight limits on the spatial curvature of the Universe, $|\Omega_K| < 0.005$, again consistent with the inflationary prediction of a spatially-flat Universe.

(6) The *Planck* data show no evidence for tensor modes. Adding a tensor amplitude as a one-parameter extension to base ΛCDM, we derive a 95% upper limit of $r_{0.002} < 0.11$. This is consistent with the *B*-mode polarization analysis reported in BKP, resolving the apparent discrepancy between the *Planck* constraints on *r* and the BICEP2 results reported by BICEP2 Collaboration (2014). In fact, by combining the *Planck* and BKP likelihoods, we find an even tighter constraint, $r_{0.002} < 0.09$, strongly disfavouring inflationary models with a $V(\phi) \propto \phi^2$ potential.

(7) The *Planck* data show no evidence for any significant running of the spectral index. We also set strong limits on a possible departure from a purely adiabatic spectrum, either through an admixture of fully-correlated isocurvature modes or from cosmic defects.

(8) The *Planck* best-fit base ΛCDM cosmology (we quote numbers for *Planck* TT+lowP+lensing here) is in good agreement with results from BAO surveys, and with the recent JLA sample of Type Ia SNe. The Hubble constant in this cosmology is $H_0 = (67.8 \pm 0.9)$ km s^{-1}Mpc^{-1}, consistent with the direct measurement of H_0 of Eq. (30) used as an H_0 prior in this paper. The *Planck* base ΛCDM cosmology is also consistent with the recent analysis of redshift-space distortions of the BOSS CMASS-DR11 data by Samushia et al. (2014) and Beutler et al. (2014a). The amplitude of the present-day fluctuation spectrum, σ_8, of the *Planck* base ΛCDM cosmology is higher than inferred from weak lensing measurements from the CFHTLenS survey (Heymans et al. 2012; Erben et al. 2013) and, possibly, from counts of rich clusters of galaxies (including *Planck* cluster counts reported in Planck Collaboration XXIV 2016). The *Planck* base ΛCDM cosmology is also discordant with Lyα BAO measurements at $z \approx 2.35$ (Delubac et al. 2015; Font-Ribera et al. 2014). At present, the reasons for these tensions are unclear.

(9) By combining the *Planck* TT+lowP+lensing data with other astrophysical data, including the JLA supernovae, the equation of state for dark energy is constrained to $w = -1.006 \pm 0.045$ and is therefore compatible with a cosmological constant, as assumed in the base ΛCDM cosmology.

(10) We have presented a detailed analysis of possible extensions to the neutrino sector of the base ΛCDM model. Combining *Planck* TT+lowP+lensing with BAO we find $N_{\rm eff} = 3.15 \pm 0.23$ for the effective number of relativistic degrees of freedom, consistent with the value $N_{\rm eff} = 3.046$ of the standard model. The sum of neutrino masses is constrained to $\sum m_\nu < 0.23$ eV. The *Planck* data strongly disfavour fully thermalized sterile neutrinos with $m_{\rm sterile} \approx 1$ eV that have been proposed as a solution to reactor neutrino oscillation anomalies. From *Planck*, we find no evidence for new neutrino physics. Standard neutrinos with masses larger than those in the minimal mass hierarchy are still allowed, and could be detectable in combination with future astrophysical and CMB lensing data.

(11) The standard theory of big bang nucleosynthesis, with $N_{\rm eff} = 3.046$ and negligible leptonic asymmetry in the electron neutrino sector, is in excellent agreement with *Planck* data and observations of primordial light element abundances. This agreement is particularly striking for deuterium, for which accurate primordial abundance measurements have been reported recently (Cooke et al. 2014). The BBN theoretical predictions for deuterium are now dominated by uncertainties in nuclear reaction rates (principally the d(p, γ)^{3}He radiative capture process), rather than from *Planck* uncertainties in the physical baryon density $\omega_{\rm b} \equiv \Omega_{\rm b} h^2$.

(12) We have investigated the temperature and polarization signatures associated with annihilating dark matter and possible deviations from the standard recombination history. Again, we find no evidence for new physics from the *Planck* data.

In summary, the *Planck* temperature and polarization spectra presented in Figs. 1 and 3 are more precise (and accurate) than those from any previous CMB experiment, and improve on the 2013 spectra presented in PCP13. Yet we find no signs for any significant deviation from the base ΛCDM cosmology. Similarly, the analysis of 2015 *Planck* data reported in Planck Collaboration XVII (2016) sets unprecedentedly tight limits on primordial non-Gaussianity. The *Planck* results offer powerful evidence in favour of simple inflationary models, which provide an attractive mechanism for generating the slightly tilted spectrum of (nearly) Gaussian adiabatic perturbations that match our data to such high precision. In addition, the *Planck* data show that the neutrino sector of the theory is consistent with the assumptions of the base ΛCDM model and that the dark energy is compatible with a cosmological constant. If there is new physics beyond base ΛCDM, then the corresponding observational signatures in the CMB are weak and difficult to detect. This is the legacy of the *Planck* mission for cosmology.

Acknowledgements. The Planck Collaboration acknowledges the support of: ESA; CNES and CNRS/INSU-IN2P3-INP (France); ASI, CNR, and INAF (Italy); NASA and DoE (USA); STFC and UKSA (UK); CSIC, MINECO, JA, and RES (Spain); Tekes, AoF, and CSC (Finland); DLR and MPG (Germany); CSA (Canada); DTU Space (Denmark); SER/SSO (Switzerland); RCN (Norway); SFI (Ireland); FCT/MCTES (Portugal); ERC and PRACE (EU). A description of the Planck Collaboration and a list of its members, indicating which technical or scientific activities they have been involved in, can be found at http://www.cosmos.esa.int/web/planck/planck-collaboration. Some of the results in this paper have been derived using the HEALPix package. The research leading to these results has received funding from the European Research Council under the European Union's Seventh Framework Programme (FP/2007−2013)/ERC Grant Agreement No. [616170] and from the UK Science and Technology Facilities Council [grant number ST/L000652/1]. Part of this work was undertaken on the STFC DiRAC HPC Facilities at the University of Cambridge, funded by UK BIS National E-infrastructure capital grants, and on the Andromeda cluster of the University of Geneva. A large set of cosmological parameter constraints from different data combinations, and including many separate extensions to the 6-parameter base ΛCDM model, are available at http://pla.esac.esa.int/pla/#cosmology.

References

Abazajian, K. N., Acero, M. A., Agarwalla, S. K., et al. 2012, ArXiv e-prints [arXiv:1204.5379]
Abazajian, K. N., Arnold, K., Austermann, J., et al. 2015a, Astropart. Phys., 63, 55
Abazajian, K. N., Arnold, K., Austermann, J., et al. 2015b, Astropart. Phys., 63, 66
Abazajian, K. N., Canac, N., Horiuchi, S., & Kaplinghat, M. 2014, Phys. Rev. D, 90, 023526
Ackermann, M., Ajello, M., Allafort, A., et al. 2012, Phys. Rev. Lett., 108, 011103
Ackermann, M., Albert, A., Anderson, B., et al. 2014, Phys. Rev. D, 89, 042001
Addison, G. E., Dunkley, J., & Spergel, D. N. 2012, MNRAS, 427, 1741
Ade, P. A. R., Akiba, Y., Anthony, A. E., et al. 2014, Phys. Rev. Lett., 113, 021301
Adelberger, E., Balantekin, A., Bemmerer, D., et al. 2011, Rev. Mod. Phys., 83, 195
Adriani, O., Barbarino, G. C., Bazilevskaya, G. A., et al. 2009, Nature, 458, 607
Aguilar, M., Aisa, D., Alvino, A., et al. 2014, Phys. Rev. Lett., 113, 121102

Albrecht, A., Battye, R. A., & Robinson, J. 1999, Phys. Rev. D, 59, 023508
Alcock, C., & Paczynski, B. 1979, Nature, 281, 358
Ali-Haïmoud, Y., & Hirata, C. M. 2010, Phys. Rev. D, 82, 063521
Ali-Haimoud, Y., & Hirata, C. M. 2011, Phys. Rev. D, 83, 043513
Amendola, L., Gordon, C., Wands, D., & Sasaki, M. 2002, Phys. Rev. Lett., 88, 211302
Anders, M., Trezzi, D., Menegazzo, R., et al. 2014, Phys. Rev. Lett., 113, 042501
Anderson, L., Aubourg, E., Bailey, S., et al. 2012, MNRAS, 427, 3435
Anderson, L., Aubourg, É., Bailey, S., et al. 2014, MNRAS, 441, 24
Archidiacono, M., Calabrese, E., & Melchiorri, A. 2011, Phys. Rev. D, 84, 123008
Archidiacono, M., Fornengo, N., Giunti, C., Hannestad, S., & Melchiorri, A. 2013a, Phys. Rev. D, 87, 125034
Archidiacono, M., Giusarma, E., Melchiorri, A., & Mena, O. 2013b, Phys. Rev. D, 87, 103519
Arkani-Hamed, N., Finkbeiner, D. P., Slatyer, T. R., & Weiner, N. 2009, Phys. Rev. D, 79, 015014
Aubourg, E., Bailey, S., Bautista, J. E., et al. 2015, Phys. Rev. D, 92, 123516
Audren, B., Lesgourgues, J., Benabed, K., & Prunet, S. 2013, J. Cosmology Astropart. Phys., 2, 001
Audren, B., Bellini, E., Cuesta, A. J., et al. 2015, JCAP, 1503, 036
Aver, E., Olive, K. A., Porter, R., & Skillman, E. D. 2013, JCAP, 1311, 017
Bartelmann, M., & Schneider, P. 2001, Phys. Rep., 340, 291
Bashinsky, S., & Seljak, U. 2004, Phys. Rev. D, 69, 083002
Battistelli, E. S., De Petris, M., Lamagna, L., et al. 2002, ApJ, 580, L101
Battye, R. A., & Moss, A. 2014, Phys. Rev. Lett., 112, 051303
Battye, R. A., Charnock, T., & Moss, A. 2015, Phys. Rev. D, 91, 103508
Beacom, J. F., Bell, N. F., & Dodelson, S. 2004, Phys. Rev. Lett., 93, 121302
Bean, R., Dunkley, J., & Pierpaoli, E. 2006, Phys. Rev. D, 74, 063503
Bell, N. F. 2005, Nucl. Phys. B Proc. Suppl., 138, 76
Bennett, C. L., Halpern, M., Hinshaw, G., et al. 2003, ApJS, 148, 1
Bennett, C. L., Hill, R. S., Hinshaw, G., et al. 2011, ApJS, 192, 17
Bennett, C. L., Larson, D., Weiland, J. L., et al. 2013, ApJS, 208, 20
Bennett, C. L., Larson, D., Weiland, J. L., & Hinshaw, G. 2014, ApJ, 794, 135
Benson, B. A., de Haan, T., Dudley, J. P., et al. 2013, ApJ, 763, 147
Bergström, J., Gonzalez-Garcia, M. C., Niro, V., & Salvado, J. 2014, JHEP, 10, 104
Béthermin, M., Daddi, E., Magdis, G., et al. 2012, ApJ, 757, L23
Betoule, M., Marriner, J., Regnault, N., et al. 2013, A&A, 552, A124
Betoule, M., Kessler, R., Guy, J., et al. 2014, A&A, 568, A22
Betts, S., et al. 2013, in Community Summer Study 2013: Snowmass on the Mississippi (CSS2013) Minneapolis, MN, USA, July 29–August 6
Beutler, F., Blake, C., Colless, M., et al. 2011, MNRAS, 416, 3017
Beutler, F., Blake, C., Colless, M., et al. 2012, MNRAS, 423, 3430
Beutler, F., Saito, S., Seo, H.-J., et al. 2014a, MNRAS, 443, 1065
Beutler, F., Saito, S., Brownstein, J. R., et al. 2014b, MNRAS, 444, 3501
Bevis, N., Hindmarsh, M., Kunz, M., & Urrestilla, J. 2007, Phys. Rev. D, 75, 065015
Bevis, N., Hindmarsh, M., Kunz, M., & Urrestilla, J. 2010, Phys. Rev. D, 82, 065004
Bianchi, D., Guzzo, L., Branchini, E., et al. 2012, MNRAS, 427, 2420
BICEP2 Collaboration. 2014, Phys. Rev. Lett., 112, 241101
BICEP2/Keck Array and Planck Collaborations 2015, Phys. Rev. Lett., 114, 101301
Blake, C., Kazin, E. A., Beutler, F., et al. 2011, MNRAS, 418, 1707
Blake, C., Brough, S., Colless, M., et al. 2012, MNRAS, 425, 405
Böhringer, H., Chon, G., & Collins, C. A. 2014, A&A, 570, A31
Bond, J., Efstathiou, G., & Tegmark, M. 1997, MNRAS, 291, L33
Boudaud, M., Aupetit, S., Caroff, S., et al. 2015, A&A, 575, A67
Bousso, R., Harlow, D., & Senatore, L. 2015, Phys. Rev. D, 91, 083527
Breit, G., & Teller, E. 1940, ApJ, 91, 215
Bucher, M., Goldhaber, A. S., & Turok, N. 1995, Phys. Rev. D, 52, 3314
Bucher, M., Moodley, K., & Turok, N. 2001a, Phys. Rev. Lett., 87, 191301
Bucher, M., Moodley, K., & Turok, N. 2001b, Phys. Rev. D, 62, 083508
Buchmuller, W., Domcke, V., & Kamada, K. 2013, Phys. Lett. B, 726, 467
Burigana, C., Danese, L., & de Zotti, G. 1991, A&A, 246, 49
Calabrese, E., Slosar, A., Melchiorri, A., Smoot, G. F., & Zahn, O. 2008, Phys. Rev. D, 77, 123531
Calabrese, E., de Putter, R., Huterer, D., Linder, E. V., & Melchiorri, A. 2011, Phys. Rev. D, 83, 023011
Calabrese, E., Hlozek, R. A., Battaglia, N., et al. 2013, Phys. Rev. D, 87, 103012
Calore, F., Cholis, I., McCabe, C., & Weniger, C. 2015, Phys. Rev. D, 91, 063003
Cesar, C. L., Fried, D. G., Killian, T. C., et al. 1996, Phys. Rev. Lett., 77, 255
Chen, X.-L., & Kamionkowski, M. 2004, Phys. Rev. D, 70, 043502
Chluba, J. 2014, MNRAS, 443, 1881
Chluba, J., & Sunyaev, R. A. 2006a, A&A, 458, L29
Chluba, J., & Sunyaev, R. A. 2006b, A&A, 446, 39
Chluba, J., & Sunyaev, R. A. 2007, A&A, 475, 109
Chluba, J., & Sunyaev, R. A. 2008, A&A, 478, L27
Chluba, J., & Sunyaev, R. A. 2012, MNRAS, 419, 1294
Chluba, J., & Thomas, R. M. 2011, MNRAS, 412, 748
Chluba, J., Fung, J., & Switzer, E. R. 2012, MNRAS, 423, 3227
Cholis, I., & Hooper, D. 2013, Phys. Rev. D, 88, 023013
Choudhury, T. R., Puchwein, E., Haehnelt, M. G., & Bolton, J. S. 2015, MNRAS, 452, 261
Chuang, C.-H., Prada, F, Pellejero-Ibanez, M., et al. 2016, MNRAS, 461, 3781
Cocco, A. G., Mangano, G., & Messina, M. 2007, JCAP, 0706, 015
Coleman, S. R., & De Luccia, F. 1980, Phys. Rev. D, 21, 3305
Conley, A., Guy, J., Sullivan, M., et al. 2011, ApJS, 192, 1
Conlon, J. P., & Marsh, M. C. D. 2013, JHEP, 1310, 214
Cooke, R., Pettini, M., Jorgenson, R. A., Murphy, M. T., & Steidel, C. C. 2014, ApJ, 781, 31
Copeland, E. J., & Kibble, T. 2010, Proc. Roy. Soc. Lond. A, 466, 623
Copeland, E. J., Sami, M., & Tsujikawa, S. 2006, Int. J. Mod. Phys. D, 15, 1753
Creminelli, P., Dubovsky, S., López Nacir, D., et al. 2015, Phys. Rev. D, 92, 123528
Cuesta, A. J., Verde, L., Riess, A., & Jimenez, R. 2015, MNRAS, 448, 3463
Czerny, M., Kobayashi, T., & Takahashi, F. 2014, Phys. Lett. B, 735, 176
Das, S., Louis, T., Nolta, M. R., et al. 2014, JCAP, 4, 14
Daylan, T., Finkbeiner, D. P., Hooper, D., et al. 2016, Phys. Dark Univ., 12, 1
de la Torre, S., Guzzo, L., Peacock, J. A., et al. 2013, A&A, 557, A54
Delubac, T., Bautista, J. E., Busca, N. G., et al. 2015, A&A, 574, A59
Di Valentino, E., Gustavino, C., Lesgourgues, J., et al. 2014, Phys. Rev. D, 90, 023543
Diamanti, R., Lopez-Honorez, L., Mena, O., Palomares-Ruiz, S., & Vincent, A. C. 2014, JCAP, 1402, 017
Dodelson, S., & Widrow, L. M. 1994, Phys. Rev. Lett., 72, 17
Doran, M. 2005, JCAP, 0510, 011
Doroshkevich, A. G., Naselsky, I. P., Naselsky, P. D., & Novikov, I. D. 2003, ApJ, 586, 709
Drexlin, G., Hannen, V., Mertens, S., & Weinheimer, C. 2013, Adv. High Energy Phys., 2013, 293986
Dubrovich, V. K., & Grachev, S. I. 2005, Astron. Lett., 31, 359
Dunkley, J., Calabrese, E., Sievers, J., et al. 2013, JCAP, 7, 25
Durrer, R., Kunz, M., & Melchiorri, A. 2002, Phys. Rept., 364, 1
Efstathiou, G. 2004, MNRAS, 349, 603
Efstathiou, G. 2006, MNRAS, 370, 343
Efstathiou, G. 2014, MNRAS, 440, 1138
Efstathiou, G., & Migliaccio, M. 2012, MNRAS, 423, 2492
Ellis, J., Nanopoulos, D. V., & Olive, K. A. 2013, Phys. Rev. Lett., 111, 111301
Erben, T., Hildebrandt, H., Miller, L., et al. 2013, MNRAS, 433, 2545
Evoli, C., Pandolfi, S., & Ferrara, A. 2013, MNRAS, 433, 1736
Fabbri, R., Melchiorri, F., & Natale, V. 1978, Ap&SS, 59, 223
Fan, X., Strauss, M. A., Becker, R. H., et al. 2006, AJ, 132, 117
Fang, W., Hu, W., & Lewis, A. 2008, Phys. Rev. D, 78, 087303
Farhang, M., Bond, J. R., & Chluba, J. 2012, ApJ, 752, 88
Farhang, M., Bond, J. R., Chluba, J., & Switzer, E. R. 2013, ApJ, 764, 137
Ferrara, S., Kallosh, R., Linde, A., & Porrati, M. 2013, Phys. Rev. D, 88, 085038
Fields, B. D., Molaro, P., & Sarkar, S. 2014, Chin. Phys. C, 38, 339
Finkbeiner, D. P., Galli, S., Lin, T., & Slatyer, T. R. 2012, Phys. Rev. D, 85, 043522
Fixsen, D. J. 2003, ApJ, 594, L67
Fixsen, D. J. 2009, ApJ, 707, 916
Fixsen, D. J., Cheng, E. S., Gales, J. M., et al. 1996, ApJ, 473, 576
Flauger, R., Hill, J. C., & Spergel, D. N. 2014, JCAP, 8, 39
Font-Ribera, A., Kirkby, D., Busca, N., et al. 2014, JCAP, 5, 27
Freedman, W. L., Madore, B. F., Scowcroft, V., et al. 2012, ApJ, 758, 24
Freivogel, B., Kleban, M., Rodriguez Martinez, M., & Susskind, L. 2006, JHEP, 0603, 039
Fu, L., Kilbinger, M., Erben, T., et al. 2014, MNRAS, 441, 2725
Fuskeland, U., Wehus, I. K., Eriksen, H. K., & Næss, S. K. 2014, ApJ, 790, 104
Galli, S., Bean, R., Melchiorri, A., & Silk, J. 2008, Phys. Rev. D, 78, 063532
Galli, S., Iocco, F., Bertone, G., & Melchiorri, A. 2009a, Phys. Rev. D, 80, 023505
Galli, S., Melchiorri, A., Smoot, G. F., & Zahn, O. 2009b, Phys. Rev. D, 80, 023508
Galli, S., Iocco, F., Bertone, G., & Melchiorri, A. 2011, Phys. Rev. D, 84, 027302
Galli, S., Slatyer, T. R., Valdes, M., & Iocco, F. 2013, Phys. Rev. D, 88, 063502
Galli, S., Benabed, K., Bouchet, F., et al. 2014, Phys. Rev. D, 90, 063504
Garcia-Bellido, J., Roest, D., Scalisi, M., & Zavala, I. 2014, Phys. Rev. D, 90, 123539
Gariazzo, S., Giunti, C., & Laveder, M. 2013, JHEP, 1311, 211
Gariazzo, S., Giunti, C., & Laveder, M. 2014, ArXiv e-prints [arXiv:1404.6160]
George, E. M., Reichardt, C. L., Aird, K. A., et al. 2015, ApJ, 799, 177

Gerbino, M., Di Valentino, E., & Said, N. 2013, Phys. Rev. D, 88, 063538
Giesen, G., Lesgourgues, J., Audren, B., & Ali-Haimoud, Y. 2012, JCAP, 1212, 008
Gil-Marín, H., Percival, W. J., Brownstein, J. R., et al. 2016, MNRAS, 460, 4188
Giunti, C., Laveder, M., Li, Y., & Long, H. 2013, Phys. Rev. D, 88, 073008
Goldman, S. P. 1989, Phys. Rev. A, 40, 1185
Goodenough, L., & Hooper, D. 2009, ArXiv e-prints [arXiv:0910.2998]
Gordon, C., & Lewis, A. 2003, Phys. Rev. D, 67, 123513
Gordon, C., & Macías, O. 2013, Phys. Rev. D, 88, 083521
Górski, K. M., Hivon, E., Banday, A. J., et al. 2005, ApJ, 622, 759
Gott, J. 1982, Nature, 295, 304
Grin, D., & Hirata, C. M. 2010, Phys. Rev. D, 81, 083005
Grin, D., Dore, O., & Kamionkowski, M. 2011, Phys. Rev. D, 84, 123003
Grin, D., Hanson, D., Holder, G. P., Doré, O., & Kamionkowski, M. 2014, Phys. Rev. D, 89, 023006
Gunn, J. E., & Peterson, B. A. 1965, ApJ, 142, 1633
Hamann, J., & Hasenkamp, J. 2013, JCAP, 1310, 044
Hamann, J., & Wong, Y. Y. Y. 2008, JCAP, 3, 25
Hamimeche, S., & Lewis, A. 2008, Phys. Rev. D, 77, 103013
Hannestad, S. 2005, JCAP, 0502, 011
Hanson, D., Hoover, S., Crites, A., et al. 2013, Phys. Rev. Lett., 111, 141301
Harnois-Déraps, J., van Waerbeke, L., Viola, M., & Heymans, C. 2015, MNRAS, 450, 1212
Hasenkamp, J. 2014, JCAP, 1409, 048
Hasenkamp, J., & Kersten, J. 2013, JCAP, 1308, 024
Hasselfield, M., Moodley, K., Bond, J. R., et al. 2013a, ApJS, 209, 17
Hasselfield, M., Hilton, M., Marriage, T. A., et al. 2013b, JCAP, 1307, 008
Heymans, C., Van Waerbeke, L., Miller, L., et al. 2012, MNRAS, 427, 146
Heymans, C., Grocutt, E., Heavens, A., et al. 2013, MNRAS, 432, 2433
Hindmarsh, M., & Kibble, T. 1995, Rept. Prog. Phys., 58, 477
Hinshaw, G., Spergel, D. N., Verde, L., et al. 2003, ApJS, 148, 135
Hinshaw, G., Larson, D., Komatsu, E., et al. 2013, ApJS, 208, 19
Hirata, C. M. 2008, Phys. Rev. D, 78, 023001
Hoekstra, H., Herbonnet, R., Muzzin, A., et al. 2015, MNRAS, 449, 685
Hou, Z., Reichardt, C. L., Story, K. T., et al. 2014, ApJ, 782, 74
Howlett, C., Ross, A., Samushia, L., Percival, W., & Manera, M. 2015, MNRAS, 449, 848
Hu, W. 1998, ApJ, 506, 485
Hu, W., & Sawicki, I. 2007, Phys. Rev. D, 76, 104043
Hu, W., & Silk, J. 1993, Phys. Rev. D, 48, 485
Hu, W., Scott, D., Sugiyama, N., & White, M. 1995, Phys. Rev. D, 52, 5498
Hu, W., Eisenstein, D. J., Tegmark, M., & White, M. 1999, Phys. Rev. D, 59, 023512
Humphreys, E. M. L., Reid, M. J., Moran, J. M., Greenhill, L. J., & Argon, A. L. 2013, ApJ, 775, 13
Hurier, G., Aghanim, N., Douspis, M., & Pointecouteau, E. 2014, A&A, 561, A143
Hutsi, G., Chluba, J., Hektor, A., & Raidal, M. 2011, A&A, 535, A26
Hütsi, G., Hektor, A., & Raidal, M. 2009, A&A, 505, 999
Iocco, F., Mangano, G., Miele, G., Pisanti, O., & Serpico, P. D. 2009, Phys. Rep., 472, 1
Izotov, Y., Thuan, T., & Guseva, N. 2014, MNRAS, 445, 778
Jeannerot, R., Rocher, J., & Sakellariadou, M. 2003, Phys. Rev. D, 68, 103514
Jeong, D., Pradler, J., Chluba, J., & Kamionkowski, M. 2014, Phys. Rev. Lett., 113, 061301
Kallosh, R., & Linde, A. 2013, JCAP, 6, 28
Kaplinghat, M., Scherrer, R. J., & Turner, M. S. 1999, Phys. Rev. D, 60, 023516
Karshenboim, S. G., & Ivanov, V. G. 2008, Astron. Lett., 34, 289
Kazin, E. A., Koda, J., Blake, C., et al. 2014, MNRAS, 441, 3524
Kesden, M., Cooray, A., & Kamionkowski, M. 2003, Phys. Rev. D, 67, 123507
Kholupenko, E. E., & Ivanchik, A. V. 2006, Astron. Lett., 32, 795
Kholupenko, E. E., Ivanchik, A. V., & Varshalovich, D. A. 2007, MNRAS, 378, L39
Kibble, T. 1976, J. Phys. A, 9, 1387
Kilbinger, M., Fu, L., Heymans, C., et al. 2013, MNRAS, 430, 2200
Kitching, T. D., Heavens, A. F., Alsing, J., et al. 2014, MNRAS, 442, 1326
Komatsu, E., Dunkley, J., Nolta, M. R., et al. 2009, ApJS, 180, 330
Kopp, J., Machado, P. A. N., Maltoni, M., & Schwetz, T. 2013, JHEP, 1305, 050
Kosowsky, A., & Turner, M. S. 1995, Phys. Rev. D, 52, 1739
Krüger, H., & Oed, A. 1975, Phys. Lett. A, 54, 251
Labzowsky, L. N., Shonin, A. V., & Solovyev, D. A. 2005, J. Phys. B Atomic Mol. Phys., 38, 265
Lacroix, T., Boehm, C., & Silk, J. 2014, Phys. Rev. D, 90, 043508
Larson, D., Dunkley, J., Hinshaw, G., et al. 2011, ApJS, 192, 16
Leistedt, B., Peiris, H. V., & Verde, L. 2014, Phys. Rev. Lett., 113, 041301
Lesgourgues, J. 2011, ArXiv e-prints [arXiv:1104.2932]
Lesgourgues, J., & Pastor, S. 2006, Phys. Rep., 429, 307
Lewis, A. 2013, Phys. Rev. D, 87, 103529
Lewis, A., & Bridle, S. 2002, Phys. Rev. D, 66, 103511
Lewis, A., & Challinor, A. 2006, Phys. Rep., 429, 1
Lewis, A., Challinor, A., & Lasenby, A. 2000, ApJ, 538, 473
Linde, A. 1999, Phys. Rev. D, 59, 023503
Linde, A. 2003, JCAP, 5, 2
Long, A. J., Lunardini, C., & Sabancilar, E. 2014, JCAP, 1408, 038
Lueker, M., Reichardt, C. L., Schaffer, K. K., et al. 2010, ApJ, 719, 1045
Luzzi, G., Shimon, M., Lamagna, L., et al. 2009, ApJ, 705, 1122
Lyth, D. H. 1997, Phys. Rev. Lett., 78, 1861
Lyth, D., & Wands, D. 2002, Phys. Lett. B, 524, 5
Ma, L., Karwowski, H. J., Brune, C. R., et al. 1997, Phys. Rev. C, 55, 588
MacCrann, N., Zuntz, J., Bridle, S., Jain, B., & Becker, M. R. 2015, MNRAS, 451, 2877
Madhavacheril, M. S., Sehgal, N., & Slatyer, T. R. 2014, Phys. Rev. D, 89, 103508
Mandelbaum, R., Slosar, A., Baldauf, T., et al. 2013, MNRAS, 432, 1544
Mangano, G., Miele, G., Pastor, S., & Peloso, M. 2002, Phys. Lett. B, 534, 8
Mantz, A. B., von der Linden, A., Allen, S. W., et al. 2015, MNRAS, 446, 2205
Marcucci, L., Viviani, M., Schiavilla, R., Kievsky, A., & Rosati, S. 2005, Phys. Rev. C, 72, 014001
Martins, C., & Shellard, E. 2002, Phys. Rev. D, 65, 043514
McCarthy, I. G., Le Brun, A. M. C., Schaye, J., & Holder, G. P. 2014, MNRAS, 440, 3645
Meerburg, P. D. 2014, Phys. Rev. D, 90, 063529
Minor, Q. E., & Kaplinghat, M. 2015, Phys. Rev. D, 91, 063504
Mirizzi, A., Mangano, G., Saviano, N., et al. 2013, Phys. Lett. B, 726, 8
Mollerach, S. 1990, Phys. Rev. D, 42, 313
Mortonson, M. J., & Hu, W. 2008, ApJ, 672, 737
Mortonson, M. J., & Seljak, U. 2014, JCAP, 10, 35
Mosher, J., Guy, J., Kessler, R., et al. 2014, ApJ, 793, 16
Mukhanov, V. F., & Chibisov, G. V. 1981, JETPL, 33, 532
Mukhanov, V., Kim, J., Naselsky, P., Trombetti, T., & Burigana, C. 2012, JCAP, 6, 40
Nakamura, K., & Petcov, S. T. 2014, in Chin. Phys. C, 38, Rev. Part. Phys., ed. K. Olive, 090001
Nollett, K. M., & Holder, G. P. 2011, ArXiv e-prints [arXiv:1112.2683]
O'Connell, D., Kollath, K. J., Duncan, A. J., & Kleinpoppen, H. 1975, J. Phys. B Atom. Mol. Phys., 8, L214
Oka, A., Saito, S., Nishimichi, T., Taruya, A., & Yamamoto, K. 2014, MNRAS, 439, 2515
Okumura, T., Seljak, U., & Desjacques, V. 2012, JCAP, 11, 14
Olive, K. A., Agashe, K., Amsler, C., et al. 2014, Chin. Phys., C38, 090001
Opher, R., & Pelinson, A. 2004, Phys. Rev. D, 70, 063529
Opher, R., & Pelinson, A. 2005, MNRAS, 362, 167
Padmanabhan, N., & Finkbeiner, D. P. 2005, Phys. Rev. D, 72, 023508
Palanque-Delabrouille, N., Yèche, C., Lesgourgues, J., et al. 2015, JCAP, 1502, 045
Pan, Z., Knox, L., & White, M. 2014, MNRAS, 445, 2941
Peebles, P. J. E. 1968, ApJ, 153, 1
Peebles, P. J. E., & Yu, J. T. 1970, ApJ, 162, 815
Peebles, P. J. E., Seager, S., & Hu, W. 2000, ApJ, 539, L1
Peimbert, M. 2008, Current Science, 95, 1165
Percival, W. J., & White, M. 2009, MNRAS, 393, 297
Percival, W. J., Reid, B. A., Eisenstein, D. J., et al. 2010, MNRAS, 401, 2148
Perlmutter, S., Aldering, G., Goldhaber, G., et al. 1999, ApJ, 517, 565
Pettini, M., & Cooke, R. 2012, MNRAS, 425, 2477
Pisanti, O., Cirillo, A., Esposito, S., et al. 2008, Comput. Phys. Commun., 178, 956
Planck Collaboration I. 2014, A&A, 571, A1
Planck Collaboration XV. 2014, A&A, 571, A15
Planck Collaboration XVI. 2014, A&A, 571, A16
Planck Collaboration XVII. 2014, A&A, 571, A17
Planck Collaboration XX. 2014, A&A, 571, A20
Planck Collaboration XXII. 2014, A&A, 571, A22
Planck Collaboration XXIII. 2014, A&A, 571, A23
Planck Collaboration XXIV. 2014, A&A, 571, A24
Planck Collaboration XXV. 2014, A&A, 571, A25
Planck Collaboration XXX. 2014, A&A, 571, A30
Planck Collaboration XXXI. 2014, A&A, 571, A31
Planck Collaboration I. 2016, A&A, 594, A1
Planck Collaboration II. 2016, A&A, 594, A2
Planck Collaboration III. 2016, A&A, 594, A3
Planck Collaboration IV. 2016, A&A, 594, A4
Planck Collaboration V. 2016, A&A, 594, A5
Planck Collaboration VI. 2016, A&A, 594, A6
Planck Collaboration VII. 2016, A&A, 594, A7
Planck Collaboration VIII. 2016, A&A, 594, A8
Planck Collaboration IX. 2016, A&A, 594, A9

Planck Collaboration X. 2016, A&A, 594, A10
Planck Collaboration XI. 2016, A&A, 594, A11
Planck Collaboration XII. 2016, A&A, 594, A12
Planck Collaboration XIII. 2016, A&A, 594, A13
Planck Collaboration XIV. 2016, A&A, 594, A14
Planck Collaboration XV. 2016, A&A, 594, A15
Planck Collaboration XVI. 2016, A&A, 594, A16
Planck Collaboration XVII. 2016, A&A, 594, A17
Planck Collaboration XVIII. 2016, A&A, 594, A18
Planck Collaboration XIX. 2016, A&A, 594, A19
Planck Collaboration XX. 2016, A&A, 594, A20
Planck Collaboration XXI. 2016, A&A, 594, A21
Planck Collaboration XXII. 2016, A&A, 594, A22
Planck Collaboration XXIII. 2016, A&A, 594, A23
Planck Collaboration XXIV. 2016, A&A, 594, A24
Planck Collaboration XXV. 2016, A&A, 594, A25
Planck Collaboration XXVI. 2016, A&A, 594, A26
Planck Collaboration XXVII. 2016, A&A, 594, A27
Planck Collaboration XXVIII. 2016, A&A, 594, A28
Planck Collaboration Int. XVI. 2014, A&A, 566, A54
Planck Collaboration Int. XXII. 2015, A&A, 576, A107
Planck Collaboration Int. XXX. 2016, A&A, 586, A133
Planck Collaboration Int. XLVI. 2016, A&A, in press, DOI: 10.1051/0004-6361/201628890
Pogosian, L., & Vachaspati, T. 1999, Phys. Rev. D, 60, 083504
POLARBEAR Collaboration 2014a, ApJ, 794, 171
POLARBEAR Collaboration 2014b, Phys. Rev. Lett., 112, 131302
Polchinski, J. 2005, Int. J. Mod. Phys. A, 20, 3413
Profumo, S. 2013, ArXiv e-prints [arXiv:1301.0952]
Reichardt, C. L., Shaw, L., Zahn, O., et al. 2012, ApJ, 755, 70
Reid, B. A., Seo, H.-J., Leauthaud, A., Tinker, J. L., & White, M. 2014, MNRAS, 444, 476
Rephaeli, Y. 1980, ApJ, 241, 858
Rest, A., Scolnic, D., Foley, R. J., et al. 2014, ApJ, 795, 44
Riess, A. G., Filippenko, A. V., Challis, P., et al. 1998, AJ, 116, 1009
Riess, A. G., Macri, L., Casertano, S., et al. 2011, ApJ, 730, 119
Rigault, M., Aldering, G., Kowalski, M., et al. 2015, ApJ, 802, 20
Robertson, B. E., Furlanetto, S. R., Schneider, E., et al. 2013, ApJ, 768, 71
Roest, D. 2014, JCAP, 1401, 007
Ross, A. J., Samushia, L., Howlett, C., et al. 2015, MNRAS, 449, 835
Rubiño-Martín, J. A., Chluba, J., & Sunyaev, R. A. 2006, MNRAS, 371, 1939
Rubiño-Martín, J. A., Chluba, J., & Sunyaev, R. A. 2008, A&A, 485, 377
Rubiño-Martín, J. A., Chluba, J., Fendt, W. A., & Wandelt, B. D. 2010, MNRAS, 403, 439
Samushia, L., Reid, B. A., White, M., et al. 2014, MNRAS, 439, 3504
Saro, A., Liu, J., Mohr, J. J., et al. 2014, MNRAS, 440, 2610
Sawyer, R. F. 2006, Phys. Rev. D, 74, 043527
Schmittfull, M. M., Challinor, A., Hanson, D., & Lewis, A. 2013, Phys. Rev. D, 88, 063012
Scóccola, C. G., Landau, S. J., & Vucetich, H. 2009, Mem. Soc. Astron. It., 80, 814
Scolnic, D., Rest, A., Riess, A., et al. 2014, ApJ, 795, 45
Seager, S., Sasselov, D. D., & Scott, D. 1999, ApJ, 523, L1
Seager, S., Sasselov, D. D., & Scott, D. 2000, ApJS, 128, 407
Seljak, U., Sugiyama, N., White, M., & Zaldarriaga, M. 2003, Phys. Rev. D, 68, 083507
Serenelli, A. M., & Basu, S. 2010, ApJ, 719, 865
Serpico, P. D., Esposito, S., Iocco, F., et al. 2004, JCAP, 0412, 010
Shaw, J. R., & Chluba, J. 2011, MNRAS, 415, 1343
Shull, J. M., & van Steenberg, M. E. 1985, ApJ, 298, 268
Silverstein, E., & Westphal, A. 2008, Phys. Rev. D, 78, 106003
Simet, M., Battaglia, N., Mandelbaum, R., & Seljak, U. 2015, ArXiv e-prints [arXiv:1502.01024]
Simha, V., & Steigman, G. 2008, JCAP, 6, 16
Slatyer, T. R., Padmanabhan, N., & Finkbeiner, D. P. 2009, Phys. Rev. D, 80, 043526
Smith, R. E., Peacock, J. A., Jenkins, A., et al. 2003, MNRAS, 341, 1311
Smith, T. L., Das, S., & Zahn, O. 2012, Phys. Rev. D, 85, 023001
Smoot, G. F., Bennett, C. L., Kogut, A., et al. 1992, ApJ, 396, L1
Song, Y.-S., & Percival, W. J. 2009, JCAP, 10, 4
Spergel, D. N., Verde, L., Peiris, H. V., et al. 2003, ApJS, 148, 175
Spergel, D. N., Flauger, R., & Hložek, R. 2015, Phys. Rev. D, 91, 023518
Spitzer, Jr., L., & Greenstein, J. L. 1951, ApJ, 114, 407
Starobinsky, A. A. 1979, JETPL, 30, 682
Starobinsky, A. A. 1980, Phys. Lett. B, 91, 99
Story, K. T., Reichardt, C. L., Hou, Z., et al. 2013, ApJ, 779, 86
Story, K. T., Hanson, D., Ade, P. A. R., et al. 2015, ApJ, 810, 50
Sunyaev, R. A., & Zeldovich, Y. B. 1970, Ap&SS, 7, 3
Suzuki, N., Rubin, D., Lidman, C., et al. 2012, ApJ, 746, 85
Switzer, E. R., & Hirata, C. M. 2008, Phys. Rev. D, 77, 083006
Takahashi, R., Sato, M., Nishimichi, T., Taruya, A., & Oguri, M. 2012, ApJ, 761, 152
Tammann, G. A., & Reindl, B. 2013, A&A, 549, A136
Tammann, G. A., Sandage, A., & Reindl, B. 2008, A&ARv, 15, 289
Trac, H., Bode, P., & Ostriker, J. P. 2011, ApJ, 727, 94
Trotta, R., & Melchiorri, A. 2005, Phys. Rev. Lett., 95, 011305
Tsujikawa, S. 2010, Lect. Notes Phys., 800, 99
Urrestilla, J., Bevis, N., Hindmarsh, M., Kunz, M., & Liddle, A. R. 2008, JCAP, 0807, 010
Valdes, M., Evoli, C., & Ferrara, A. 2010, MNRAS, 404, 1569
van Engelen, A., Sherwin, B. D., Sehgal, N., et al. 2015, ApJ, 808, 7
Viero, M. P., Wang, L., Zemcov, M., et al. 2013, ApJ, 772, 77
Vilenkin, A., & Shellard, E. 2000, Cosmic Strings and Other Topological Defects, Cambridge Monographs on Mathematical Physics (Cambridge University Press)
Viviani, M., Kievsky, A., Marcucci, L. E., Rosati, S., & Schiavilla, R. 2000, Phys. Rev. C, 61, 064001
von der Linden, A., Mantz, A., Allen, S. W., et al. 2014, MNRAS, 443, 1973
Weinberg, S. 2013, Phys. Rev. Lett., 110, 241301
White, M., Reid, B., Chuang, C.-H., et al. 2015, MNRAS, 447, 234
Wong, W. Y., & Scott, D. 2007, MNRAS, 375, 1441
Wong, W. Y., Seager, S., & Scott, D. 2006, MNRAS, 367, 1666
Wong, W. Y., Moss, A., & Scott, D. 2008, MNRAS, 386, 1023
Wyman, M., Rudd, D. H., Vanderveld, R. A., & Hu, W. 2014, Phys. Rev. Lett., 112, 051302
Yue, A., Dewey, M., Gilliam, D., et al. 2013, Phys. Rev. Lett., 111, 222501
Zaldarriaga, M., Spergel, D. N., & Seljak, U. 1997, ApJ, 488, 1
Zeldovich, Y. B., Kurt, V. G., & Syunyaev, R. A. 1968, Zhurnal Eksperimental noi i Teoreticheskoi Fiziki, 55, 278
Zeldovich, Y. B., & Sunyaev, R. A. 1969, Ap&SS, 4, 301
Zhang, L., Chen, X., Lei, Y.-A., & Si, Z.-G. 2006, Phys. Rev. D, 74, 103519

[1] APC, AstroParticule et Cosmologie, Université Paris Diderot, CNRS/IN2P3, CEA/lrfu, Observatoire de Paris, Sorbonne Paris Cité, 10 rue Alice Domon et Léonie Duquet, 75205 Paris Cedex 13, France
[2] Aalto University Metsähovi Radio Observatory and Dept of Radio Science and Engineering, PO Box 13000, 00076 AALTO, Finland
[3] African Institute for Mathematical Sciences, 6-8 Melrose Road, Muizenberg, 7945 Cape Town, South Africa
[4] Agenzia Spaziale Italiana Science Data Center, via del Politecnico snc, 00133 Roma, Italy
[5] Aix Marseille Université, CNRS, LAM (Laboratoire d'Astrophysique de Marseille) UMR 7326, 13388 Marseille, France
[6] Aix Marseille Université, Centre de Physique Théorique, 163 Avenue de Luminy, 13288 Marseille, France
[7] Astrophysics Group, Cavendish Laboratory, University of Cambridge, J J Thomson Avenue, Cambridge CB3 0HE, UK
[8] Astrophysics & Cosmology Research Unit, School of Mathematics, Statistics & Computer Science, University of KwaZulu-Natal, Westville Campus, Private Bag X54001, 4000 Durban, South Africa
[9] Atacama Large Millimeter/submillimeter Array, ALMA Santiago Central Offices, Alonso de Cordova 3107, Vitacura, Casilla 763 0355, Santiago, Chile
[10] CGEE, SCS Qd 9, Lote C, Torre C, 4° andar, Ed. Parque Cidade Corporate, CEP 70308-200, Brasília, DF, Brazil
[11] CITA, University of Toronto, 60 St. George St., Toronto, ON M5S 3H8, Canada
[12] CNRS, IRAP, 9 Av. colonel Roche, BP 44346, 31028 Toulouse Cedex 4, France
[13] CRANN, Trinity College, Dublin, Ireland
[14] California Institute of Technology, Pasadena, California, USA
[15] Centre for Theoretical Cosmology, DAMTP, University of Cambridge, Wilberforce Road, Cambridge CB3 0WA, UK
[16] Centro de Estudios de Física del Cosmos de Aragón (CEFCA), Plaza San Juan, 1, planta 2, 44001 Teruel, Spain
[17] Computational Cosmology Center, Lawrence Berkeley National Laboratory, Berkeley, California, USA

[18] Consejo Superior de Investigaciones Científicas (CSIC), 28049 Madrid, Spain
[19] DSM/Irfu/SPP, CEA-Saclay, 91191 Gif-sur-Yvette Cedex, France
[20] DTU Space, National Space Institute, Technical University of Denmark, Elektrovej 327, 2800 Kgs. Lyngby, Denmark
[21] Département de Physique Théorique, Université de Genève, 24, Quai E. Ansermet, 1211 Genève 4, Switzerland
[22] Departamento de Astrofísica, Universidad de La Laguna (ULL), 38206 La Laguna, Tenerife, Spain
[23] Departamento de Física, Universidad de Oviedo, Avda. Calvo Sotelo s/n, 33007 Oviedo, Spain
[24] Department of Astronomy and Astrophysics, University of Toronto, 50 Saint George Street, 38100 Toronto, Ontario, Canada
[25] Department of Astrophysics/IMAPP, Radboud University Nijmegen, PO Box 9010, 6500 GL Nijmegen, The Netherlands
[26] Department of Physics & Astronomy, University of British Columbia, 6224 Agricultural Road, Vancouver, British Columbia, Canada
[27] Department of Physics and Astronomy, Dana and David Dornsife College of Letter, Arts and Sciences, University of Southern California, Los Angeles, CA 90089, USA
[28] Department of Physics and Astronomy, Johns Hopkins University, Bloomberg Center 435, 3400 N. Charles St., Baltimore, MD 21218, USA
[29] Department of Physics and Astronomy, University College London, London WC1E 6BT, UK
[30] Department of Physics and Astronomy, University of Sussex, Brighton BN1 9QH, UK
[31] Department of Physics, Florida State University, Keen Physics Building, 77 Chieftan Way, Tallahassee, Florida, USA
[32] Department of Physics, Gustaf Hällströmin katu 2a, University of Helsinki, 00560 Helsinki, Finland
[33] Department of Physics, Princeton University, Princeton, New Jersey, NJ 08540, USA
[34] Department of Physics, University of California, Berkeley, California, CA 94720, USA
[35] Department of Physics, University of California, One Shields Avenue, Davis, California, CA 93106, USA
[36] Department of Physics, University of California, Santa Barbara, California, USA
[37] Department of Physics, University of Illinois at Urbana-Champaign, 1110 West Green Street, Urbana, Illinois, IL 61801 USA
[38] Dipartimento di Fisica e Astronomia G. Galilei, Università degli Studi di Padova, via Marzolo 8, 35131 Padova, Italy
[39] Dipartimento di Fisica e Scienze della Terra, Università di Ferrara, via Saragat 1, 44122 Ferrara, Italy
[40] Dipartimento di Fisica, Università La Sapienza, P. le A. Moro 2, 00185 Roma, Italy
[41] Dipartimento di Fisica, Università degli Studi di Milano, via Celoria, 16, 20133 Milano, Italy
[42] Dipartimento di Fisica, Università degli Studi di Trieste, via A. Valerio 2, 34127 Trieste, Italy
[43] Dipartimento di Matematica, Università di Roma Tor Vergata, via della Ricerca Scientifica, 1, 00185 Roma, Italy
[44] Discovery Center, Niels Bohr Institute, Blegdamsvej 17, 1165 Copenhagen, Denmark
[45] Discovery Center, Niels Bohr Institute, Copenhagen University, Blegdamsvej 17, 1165 Copenhagen, Denmark
[46] European Southern Observatory, ESO Vitacura, Alonso de Cordova 3107, Vitacura, Casilla 19001, Santiago, Chile
[47] European Space Agency, ESAC, Planck Science Office, Camino bajo del Castillo, s/n, Urbanización Villafranca del Castillo, Villanueva de la Cañada, 28691 Madrid, Spain
[48] European Space Agency, ESTEC, Keplerlaan 1, 2201 AZ Noordwijk, The Netherlands
[49] Gran Sasso Science Institute, INFN, viale F. Crispi 7, 67100 L'Aquila, Italy
[50] HGSFP and University of Heidelberg, Theoretical Physics Department, Philosophenweg 16, 69120 Heidelberg, Germany
[51] Haverford College Astronomy Department, 370 Lancaster Avenue, Haverford, Pennsylvania, USA
[52] Helsinki Institute of Physics, Gustaf Hällströmin katu 2, University of Helsinki, 00560 Helsinki, Finland
[53] INAF−Osservatorio Astrofisico di Catania, via S. Sofia 78, 95123 Catania, Italy
[54] INAF−Osservatorio Astronomico di Padova, Vicolo dell'Osservatorio 5, 35131 Padova, Italy
[55] INAF−Osservatorio Astronomico di Roma, via di Frascati 33, 00040 Monte Porzio Catone, Italy
[56] INAF−Osservatorio Astronomico di Trieste, via G.B. Tiepolo 11, Trieste, Italy
[57] INAF/IASF Bologna, via Gobetti 101, Bologna, Italy
[58] INAF/IASF Milano, via E. Bassini 15, Milano, Italy
[59] INFN, Sezione di Bologna, viale Berti Pichat 6/2, 40127 Bologna, Italy
[60] INFN, Sezione di Ferrara, via Saragat 1, 44122 Ferrara, Italy
[61] INFN, Sezione di Roma 1, Università di Roma Sapienza, Piazzale Aldo Moro 2, 00185 Roma, Italy
[62] INFN, Sezione di Roma 2, Università di Roma Tor Vergata, via della Ricerca Scientifica, 1, 00185 Roma, Italy
[63] INFN/National Institute for Nuclear Physics, via Valerio 2, 34127 Trieste, Italy
[64] IPAG: Institut de Planétologie et d'Astrophysique de Grenoble, Université Grenoble Alpes, IPAG; CNRS, IPAG, 38000 Grenoble, France
[65] ISDC, Department of Astronomy, University of Geneva, ch. d'Ecogia 16, 1290 Versoix, Switzerland
[66] IUCAA, Post Bag 4, Ganeshkhind, Pune University Campus, 411 007 Pune, India
[67] Imperial College London, Astrophysics group, Blackett Laboratory, Prince Consort Road, London, SW7 2AZ, UK
[68] Infrared Processing and Analysis Center, California Institute of Technology, Pasadena, CA 91125, USA
[69] Institut Néel, CNRS, Université Joseph Fourier Grenoble I, 25 rue des Martyrs, 38042 Grenoble, France
[70] Institut Universitaire de France, 103, bd Saint-Michel, 75005 Paris, France
[71] Institut d'Astrophysique Spatiale, CNRS, Univ. Paris-Sud, Université Paris-Saclay, Bât. 121, 91405 Orsay Cedex, France
[72] Institut d'Astrophysique de Paris, CNRS (UMR 7095), 98bis boulevard Arago, 75014 Paris, France
[73] Institut für Theoretische Teilchenphysik und Kosmologie, RWTH Aachen University, 52056 Aachen, Germany
[74] Institute for Space Sciences, 077125 Bucharest-Magurale, Romania
[75] Institute of Astronomy, University of Cambridge, Madingley Road, Cambridge CB3 0HA, UK
[76] Institute of Theoretical Astrophysics, University of Oslo, Blindern, 0371 Oslo, Norway
[77] Instituto de Astrofísica de Canarias, C/Vía Láctea s/n, 38205 La Laguna, Tenerife, Spain
[78] Instituto de Física de Cantabria (CSIC-Universidad de Cantabria), Avda. de los Castros s/n, 39005 Santander, Spain
[79] Istituto Nazionale di Fisica Nucleare, Sezione di Padova, via Marzolo 8, 35131 Padova, Italy
[80] Jet Propulsion Laboratory, California Institute of Technology, 4800 Oak Grove Drive, Pasadena, California, USA
[81] Jodrell Bank Centre for Astrophysics, Alan Turing Building, School of Physics and Astronomy, The University of Manchester, Oxford Road, Manchester, M13 9PL, UK
[82] Kavli Institute for Cosmological Physics, University of Chicago, Chicago, IL 60637, USA
[83] Kavli Institute for Cosmology Cambridge, Madingley Road, Cambridge, CB3 0HA, UK
[84] Kazan Federal University, 18 Kremlyovskaya St., 420008 Kazan, Russia
[85] LAL, Université Paris-Sud, CNRS/IN2P3, 91898 Orsay, France
[86] LERMA, CNRS, Observatoire de Paris, 61 Avenue de l'Observatoire, Paris, France

[87] Laboratoire AIM, IRFU/Service d'Astrophysique – CEA/DSM – CNRS – Université Paris Diderot, Bât. 709, CEA-Saclay, 91191 Gif-sur-Yvette Cedex, France
[88] Laboratoire Traitement et Communication de l'Information, CNRS (UMR 5141) and Télécom ParisTech, 46 rue Barrault, 75634 Paris Cedex 13, France
[89] Laboratoire de Physique Subatomique et Cosmologie, Université Grenoble-Alpes, CNRS/IN2P3, 53 rue des Martyrs, 38026 Grenoble Cedex, France
[90] Laboratoire de Physique Théorique, Université Paris-Sud 11 & CNRS, Bâtiment 210, 91405 Orsay, France
[91] Lawrence Berkeley National Laboratory, Berkeley, California, USA
[92] Lebedev Physical Institute of the Russian Academy of Sciences, Astro Space Centre, 84/32 Profsoyuznaya st., 117997 Moscow, GSP-7, Russia
[93] Leung Center for Cosmology and Particle Astrophysics, National Taiwan University, 10617 Taipei, Taiwan
[94] Max-Planck-Institut für Astrophysik, Karl-Schwarzschild-Str. 1, 85741 Garching, Germany
[95] McGill Physics, Ernest Rutherford Physics Building, McGill University, 3600 rue University, Montréal, QC, H3A 2T8, Canada
[96] National University of Ireland, Department of Experimental Physics, Maynooth, Co. Kildare, Ireland
[97] Nicolaus Copernicus Astronomical Center, Bartycka 18, 00-716 Warsaw, Poland
[98] Niels Bohr Institute, Blegdamsvej 17, Copenhagen, Denmark
[99] Niels Bohr Institute, Copenhagen University, Blegdamsvej 17, 1165 Copenhagen, Denmark
[100] Nordita (Nordic Institute for Theoretical Physics), Roslagstullsbacken 23, 106 91 Stockholm, Sweden
[101] Optical Science Laboratory, University College London, Gower Street, London, UK
[102] Physics Department, Shahid Beheshti University, Tehran, Iran
[103] SISSA, Astrophysics Sector, via Bonomea 265, 34136 Trieste, Italy
[104] SMARTEST Research Centre, Università degli Studi e-Campus, via Isimbardi 10, Novedrate (CO), 22060, Italy
[105] School of Physics and Astronomy, Cardiff University, Queens Buildings, The Parade, Cardiff, CF24 3AA, UK
[106] School of Physics and Astronomy, University of Nottingham, Nottingham NG7 2RD, UK
[107] Sorbonne Université-UPMC, UMR7095, Institut d'Astrophysique de Paris, 98bis boulevard Arago, 75014 Paris, France
[108] Space Research Institute (IKI), Russian Academy of Sciences, Profsoyuznaya Str, 84/32, 117997 Moscow, Russia
[109] Space Sciences Laboratory, University of California, Berkeley, California, USA
[110] Special Astrophysical Observatory, Russian Academy of Sciences, Nizhnij Arkhyz, Zelenchukskiy region, 369167 Karachai-Cherkessian Republic, Russia
[111] Stanford University, Dept of Physics, Varian Physics Bldg, 382 via Pueblo Mall, Stanford, California, USA
[112] Sub-Department of Astrophysics, University of Oxford, Keble Road, Oxford OX1 3RH, UK
[113] Sydney Institute for Astronomy, School of Physics A28, University of Sydney, NSW 2006, Australia
[114] The Oskar Klein Centre for Cosmoparticle Physics, Department of Physics,Stockholm University, AlbaNova, 106 91 Stockholm, Sweden
[115] Theory Division, PH-TH, CERN, 1211 Geneva 23, Switzerland
[116] UPMC Univ Paris 06, UMR 7095, 98bis boulevard Arago, 75014 Paris, France
[117] Université de Toulouse, UPS-OMP, IRAP, 31028 Toulouse Cedex 4, France
[118] Universities Space Research Association, Stratospheric Observatory for Infrared Astronomy, MS 232-11, Moffett Field, CA 94035, USA
[119] University Observatory, Ludwig Maximilian University of Munich, Scheinerstrasse 1, 81679 Munich, Germany
[120] University of Granada, Departamento de Física Teórica y del Cosmos, Facultad de Ciencias, 11071 Granada, Spain
[121] University of Granada, Instituto Carlos I de Física Teórica y Computacional, 11071 Granada, Spain
[122] University of Heidelberg, Institute for Theoretical Physics, Philosophenweg 16, 69120 Heidelberg, Germany
[123] Warsaw University Observatory, Aleje Ujazdowskie 4, 00-478 Warszawa, Poland